Computer Methods in Applied Mechanics and Engineering 447 (2025) 118385

Contents lists available at ScienceDirect

Comput. Methods Appl. Mech. Engrg.

journal homepage: www.elsevier.com/locate/cma

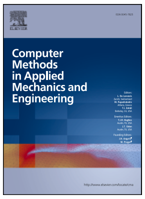

High-fidelity modelling of floor-borne vibrations in axisymmetric MRI magnets using *hp*-finite element method

Yashwanth Sooriyakanthan[a], Antonio J. Gil[a,*], Paul D. Ledger[b,*], Michael J. Mallett[c]

[a] *Data and AI, Faculty of Science and Engineering, Zienkiewicz Institute for Modelling, Swansea University, SA1 8EN, Bay Campus, UK*
[b] *School of Computing and Mathematical Sciences, University of Leicester, LE1 7RH, UK*
[c] *Siemens Healthineers, MR Magnet Technology, OX29 4BP, Eynsham, Oxon, UK*

ARTICLE INFO

Keywords:
Hp-finite elements
MRI scanners
Eddy currents
Electro-magneto-mechanics
Time vs frequency
Coupled physics
Floor borne vibrations

ABSTRACT

Magnetic Resonance Imaging (MRI) relies on the stability of highly uniform fields from superconducting main coils and spatially varying fields from AC-driven gradient coils. Both types of coils are thermally separated, as the main coils are cryogenically cooled within a cryostat whilst gradient coils operate at room temperature. Externally generated floor-borne vibrations (FBV) can induce relative motion between radiation shields and coils, generating eddy currents in the shields. These in turn produce parasitic magnetic fields that compromise field homogeneity and degrade image quality. This paper presents a high-fidelity computational framework for simulating the magneto-mechanical effects of FBV in axisymmetric MRI scanners to inform the manufacturing design workflow. The approach introduces three key advancements: **first**, a nonlinear, fully coupled magneto-mechanical formulation solved using *hp*-Finite Element Methods (*hp*-FEM) in the open-source NGSolve framework, with a focus on optimal interpolation order p and time step size; **second**, explicit mechanical modelling of both main and gradient coils, moving beyond idealised Biot-Savart type current sources; and **third**, the use of realistic axisymmetric geometries with structural connectivity between coils and radiation shields in order to inform preliminary designs in Industry. A comprehensive series of numerical results is presented in order to validate the method against some benchmarked scenarios and highlight its potential for guiding vibration mitigation and improving MRI image fidelity.

1. Introduction

Magnetic Resonance Imaging (MRI) scanners are essential diagnostic tools in modern medicine [1–4]. The high-resolution images they provide have significantly advanced the detection and assessment of various pathologies, including cardiovascular diseases, tumours, and internal haemorrhages [5]. The most common MRI systems used in clinical practice employ superconducting magnets, which enable strong and uniform magnetic fields–typically in the range of $1.5\mathrm{T} - 7\mathrm{T}$, thereby yielding superior image resolution [6–10].

The functionality of an MRI scanner (see Fig. 1) relies on a combination of strong static and time-varying magnetic fields. The primary magnetic field is generated by superconducting main coils, while spatial encoding is achieved through AC-driven gradient coils (Alternating Current-driven gradient coils), which produce non-uniform, time-dependent magnetic fields. A key structural com-

---

* Corresponding authors.
E-mail addresses: a.j.gil@swansea.ac.uk (A.J. Gil), pdl11@leicester.ac.uk (P.D. Ledger).

https://doi.org/10.1016/j.cma.2025.118385
Received 1 August 2025; Received in revised form 4 September 2025; Accepted 4 September 2025
Available online 18 September 2025
0045-7825/© 2025 The Author(s). Published by Elsevier B.V. This is an open access article under the CC BY license (http://creativecommons.org/licenses/by/4.0/).

(a) (b)

Fig. 1. (a) Magnetic Resonance Imaging scanner: Model Magnetom Free.Max. Image courtesy of Siemens Healthineers. (b) Floor-borne vibration (FBV) and impact on imaging quality: (1) FBV, (2) MRI, (3) imaging artefact.

ponent is the cryostat, which houses the main coils in a liquid helium bath (50K) within a vacuum-insulated vessel, providing thermal stability. In contrast, the gradient coils are positioned outside the cryostat and operate at ambient temperature.

Two dominant physical phenomena interact within the MRI environment: electromagnetics and mechanics. At high frequencies, displacement currents prevail in Maxwell's equations. However, at low frequencies and in highly conductive materials, the eddy current approximation is appropriate, particularly relevant for conductive shielding structures. Mechanical behaviour is generally assumed to remain in the small deformation regime, thus justifying the use of linear elasticity. The time-varying magnetic fields generated by the gradient coils induce Lorentz forces within the conducting shields, which in turn generate mechanical vibrations. These vibrations can perturb the magnetic environment, inducing additional eddy currents and secondary magnetic fields. This mutual interaction results in a fully coupled nonlinear electro-magneto-mechanical problem that can degrade image quality and compromise the longevity of scanner components. Computational approaches to this coupling have evolved. Low-order space-time finite element formulations have been proposed [11,12], while high-order *hp*-FEM techniques have been developed for both axisymmetric and full 3D geometries [13,14], incorporating linearised stress tensor formulations and DC–AC (Direct Current - Alternating Current) splitting to facilitate time-harmonic solutions in the frequency domain [15–17]. The methodology has been lately expanded to the design component of the manufacturing workflow via the consideration of reduced order modelling approaches, such as Proper Orthogonal Decomposition, Proper Generalised Decomposition and Neural Network approaches [14,18–20].

Recent developments in MRI technology have focused on increasing magnetic field strength and image resolution (i.e. above 11 T), thereby enhancing diagnostic capabilities, particularly for detecting tumours and rare conditions [22]. However, the accuracy of high-resolution imaging is sensitive to external mechanical disturbances, particularly **floor-borne vibrations (FBV)**. These vibrations introduce parasitic accelerations–both vertical and lateral–on the scanner, leading to relative motion between the radiation shields and the coils [23,24]. The resulting motion induces undesired eddy currents in the shields, which in turn generate secondary magnetic fields that distort the homogeneity of the primary magnetic field, causing image artefacts. To mitigate the impact of FBV, various vibration isolation strategies are employed, including elastomeric mats or spring-damper systems beneath the cryostat. Yet, determining the optimal configuration and placement of these isolators within a realistic 3D MRI assembly remains a non-trivial design challenge requiring expert input and advanced modelling techniques [25–27].

In light of the differing excitation frequency ranges of the gradient coil signals and the induced floor-borne vibrations, a more accurate modelling framework is necessary–beyond the linearised formulations previously considered. In this study, we examine the full nonlinear Lorentz force and induced current interactions, and compare them to their linear approximations, particularly in the context of high-resolution imaging performance. To capture the necessary spatial accuracy, we adopt an *hp*-FEM discretisation of the governing equations, combined with second-order time integration schemes, implemented for the first time within the open-source finite element platform NGSolve [28]. Due to the different element families required for electromagnetic and mechanical problems, we choose to employ a staggered coupling strategy enhanced with Aitken's Δ^2 acceleration methods [29] to improve convergence efficiency. Guided by recommendations from our industrial partner and departing from idealised Biot-Savart-based current models [30], we explicitly model both main and gradient coils as structural components. Furthermore, epoxy layers and magnetic shim structures are included to reflect realistic assembly conditions. Although the present study focuses on axisymmetric geometries–primarily for computational tractability–it forms the basis for future investigations in fully three-dimensional configurations.

Adding varying polynomial degree can help reduce the number of degrees of freedom and allow the same accuracy to be obtained with reduced computational cost. To achieve this, as well as setting an appropriate mesh spacing distribution, the distribution of the order of elements must also be controlled. This would best be achieved by using an automated adaptive procedure including an a-posteriori error estimator and an appropriate strategy to decide whether to make an *h*- or *p*- refinement for each element selected [31–33]. However, given this is an axisymmetric problem, the reduction in number of degrees of freedom would not have a significant impact on the overall cost and the additional computational effort of automated discretisation adaption and error estimation would out way this reduction. For this reason, we have chosen to tag regions with high field gradients associated with material interfaces and sharp corners, use graded meshes using boundary-layer quadrilateral elements and perform uniform p-refinement in our work. Nonetheless, for problems in three dimensions, where identifying regions associated with high field gradients is more challenging and there is a much greater need to reduce the number of degrees of freedom given the much higher computational cost, automated and adaptive procedures would become much more important.

The remainder of the paper is organised as follows: Section 2 presents the fundamental Maxwell and Cauchy equations in the general setting of a moving conductor, followed by key modelling assumptions such as the eddy current approximation and the small-strain hypothesis. This leads to the derivation of the principal electro-magneto-mechanical coupling terms: the Maxwell stress tensor and the Lorentz current. The governing equations are formulated using a vector potential approach, culminating in the definition of the complete initial-boundary value problem. Section 3 introduces the DC–AC splitting strategy relevant to MRI applications and formulates both the DC and AC sub-problems. In addition to the full nonlinear AC formulation, a linearised model from previous work is presented for comparative purposes, and the corresponding variational formulations are stated. Section 4 details the spatial hp-FEM semi-discretisation used in this work and exploited within the open-source NGSolve framework [28]. For the nonlinear AC model, a time-domain solution strategy is presented, while the linearised model is treated in the frequency domain. To accelerate the coupled solution process, an Aitken Δ^2 scheme is introduced. Section 5 presents benchmark numerical examples to assess convergence, accuracy, and solver performance within NGSolve. Section 6 follows with application-focused simulations in MRI-relevant axisymmetric configurations, developed in collaboration with our industrial partner. Finally, Section 7 summarises the key findings and outlines directions for future work.

2. Governing equations

This Section presents the Maxwell and Cauchy equations governing the solution of the problem at hand. Starting with the generic case of a deformable moving conductor within a background electromagnetic field, the key modelling assumptions for the case of an MRI scanner are introduced before arriving at the relevant Initial Boundary Value Problem.

2.1. Electromagnetics

MRI scanners generate high-strength static background magnetic fields complemented by lower strength transient magnetic fields which perturb the background field for the purpose of conducting patient scans and procuring imaging data [13,34,35]. The electromagnetic fields produced can in general be described by Maxwell's equations defined in a moving domain $\Omega_t(t) \subset \mathbb{R}^3$ with initial configuration $\Omega_0 \subset \mathbb{R}^3$, through a time varying mapping function $\boldsymbol{\phi} : \Omega_0 \subset \mathbb{R}^3 \times [0, T] \to \Omega_t(t) \subset \mathbb{R}^3$, such that an initial position $\boldsymbol{X} \in \Omega_0$ is mapped to a current position $\boldsymbol{x} = \boldsymbol{\phi}(\boldsymbol{X}, t) \in \Omega_t(t)$, introducing a displacement field $\boldsymbol{u} = \boldsymbol{x} - \boldsymbol{X}$. Sufficient smoothness of the mapping $\boldsymbol{\phi}$ ensures the existence of kinematic fields velocity $\boldsymbol{v}$, deformation gradient tensor $\boldsymbol{F}$, Jacobian $J = \det\boldsymbol{F}$ and cofactor $\boldsymbol{H} = J\boldsymbol{F}^{-T}$ [36]. Maxwell's equations can be summarised in an Updated Lagrangian description as [30,37,38]

$$\nabla \cdot \boldsymbol{D} = q, \tag{1a}$$

$$\nabla \times \boldsymbol{\mathcal{H}} = \boldsymbol{\mathcal{J}} + \overset{*}{\boldsymbol{D}}, \tag{1b}$$

$$\nabla \times \boldsymbol{\mathcal{E}} = -\overset{*}{\boldsymbol{B}}, \tag{1c}$$

$$\nabla \cdot \boldsymbol{B} = 0, \tag{1d}$$

where $\boldsymbol{D}$ is the electric flux density (also known as electric displacement), q is the volume charge density, $\boldsymbol{\mathcal{H}}$ is the magnetic field strength, $\boldsymbol{\mathcal{J}}$ is the electric current density, $\boldsymbol{\mathcal{E}}$ is the electric field strength and $\boldsymbol{B}$ is the magnetic flux density. In above equations, ∇, $\nabla\cdot$ and $\nabla\times$ denote the differential operators gradient, divergence and curl with respect to $\boldsymbol{x}$, respectively, and the upper symbol $*$ is used to represent the convective flux derivative[1]. Eq. (1a) is the Gauss law, (1b) is the Ampère-Maxwell's law, (1c) is the Faraday's law of induction and (1d) is the Gauss law of magnetism. Above (1b) and (1c) can be alternatively formulated in an Eulerian description [39] as follows

$$\nabla \times \boldsymbol{H}_E = \boldsymbol{J} + \left.\frac{\partial \boldsymbol{D}}{\partial t}\right|_{\boldsymbol{x}}, \tag{2a}$$

$$\nabla \times \boldsymbol{E} = -\left.\frac{\partial \boldsymbol{B}}{\partial t}\right|_{\boldsymbol{x}}, \tag{2b}$$

where $\boldsymbol{H}_E$ is the magnetic field strength[2], $\boldsymbol{J}$ is the electric current density and $\boldsymbol{E}$ is the electric field strength, the three measured in a fixed domain $\Omega \times [0, T]$, typical of an Eulerian description of motion [39]. Updated Lagrangian and Eulerian fields can be related as

$$\boldsymbol{\mathcal{H}} = \boldsymbol{H}_E - \boldsymbol{v} \times \boldsymbol{D}; \tag{3a}$$

$$\boldsymbol{\mathcal{J}} = \boldsymbol{J} - q\boldsymbol{v}; \tag{3b}$$

---

[1] The convective flux derivative of a vector field $\boldsymbol{S}$ is defined as $\overset{*}{\boldsymbol{S}} = \boldsymbol{H}^{-T} \left.\frac{\partial(\boldsymbol{H}^T\boldsymbol{S})}{\partial t}\right|_{\boldsymbol{X}}$.

[2] The subindex $(\cdot)_E$ has been used to avoid confusion with the cofactor $\boldsymbol{H}$ of the deformation and emphasise the Eulerian nature of the field.

$$\boldsymbol{\mathcal{E}} = \boldsymbol{E} + \boldsymbol{v} \times \boldsymbol{B}. \tag{3c}$$

To close the above system of equations, suitable constitutive equations are needed, defined as

$$\boldsymbol{D} = \boldsymbol{D}_\infty + \boldsymbol{P}; \qquad \boldsymbol{D}_\infty = \varepsilon_0 \boldsymbol{E}, \tag{4}$$

where $\varepsilon_0 \approx 8.854 \times 10^{-12}$ F/m is the electric permittivity of free space, $\boldsymbol{D}_\infty$ is the electric displacement contribution in free space and $\boldsymbol{P}$ is the polarisation vector in the presence of matter, and

$$\boldsymbol{\mathcal{H}} = \boldsymbol{\mathcal{H}}_\infty - \boldsymbol{\mathcal{M}}; \qquad \boldsymbol{H}_\infty = \frac{1}{\mu_0}\boldsymbol{B} \tag{5}$$

where $\mu_0 = 4\pi \times 10^{-7}$ N/A^2 is the magnetic permeability of free space, $\boldsymbol{\mathcal{H}}_\infty$ and $\boldsymbol{H}_\infty$ denote the vacuum magnetic field strength in both Updated Lagrangian and Eulerian descriptions related by $\boldsymbol{\mathcal{H}}_\infty = \boldsymbol{H}_\infty - \boldsymbol{v} \times \boldsymbol{D}_\infty$, and $\boldsymbol{\mathcal{M}}$ is the magnetisation vector. By exploiting relationship (3a) in combination with above constitutive laws (4) and (5), it is possible to re-write

$$\begin{aligned} \boldsymbol{H}_E &= \boldsymbol{\mathcal{H}}_\infty - \boldsymbol{\mathcal{M}} + \boldsymbol{v} \times \boldsymbol{D} \\ &= \boldsymbol{\mathcal{H}}_\infty - \boldsymbol{\mathcal{M}} + \boldsymbol{v} \times \boldsymbol{D}_\infty + \boldsymbol{v} \times \boldsymbol{P} \\ &= \underbrace{(\boldsymbol{\mathcal{H}}_\infty + \boldsymbol{v} \times \boldsymbol{D}_\infty)}_{=\boldsymbol{H}_\infty} - \underbrace{(\boldsymbol{\mathcal{M}} - \boldsymbol{v} \times \boldsymbol{P})}_{=\boldsymbol{M}} \\ &= \frac{1}{\mu_0}\boldsymbol{B} - \boldsymbol{M}, \end{aligned} \tag{6}$$

where the Eulerian-type magnetisation vector $\boldsymbol{M}$ is introduced. In addition, the electric current $\boldsymbol{\mathcal{J}}$ is generally split into a sum of free and Ohmic contributions [13] as

$$\boldsymbol{\mathcal{J}} = \boldsymbol{\mathcal{J}}_f + \gamma \boldsymbol{\mathcal{E}}, \tag{7}$$

where γ is defined as the non-negative electric conductivity (only non-zero in areas within a conductive material and zero otherwise)[3] Substitution of (3c) into (7) followed by further substitution into (3b), yields

$$\boldsymbol{J} = \underbrace{\boldsymbol{\mathcal{J}}_f}_{=\boldsymbol{J}_f} + \underbrace{\gamma \boldsymbol{E}}_{=\boldsymbol{J}_{\mathcal{O}}} + \underbrace{\gamma(\boldsymbol{v} \times \boldsymbol{B})}_{=\boldsymbol{J}_{\mathcal{L}}} + \underbrace{q\boldsymbol{v}}_{=\boldsymbol{J}_\Omega}, \tag{8}$$

where the right hand side of (8) encompasses all the possible electric current contributions, namely, free current $\boldsymbol{J}_f = \boldsymbol{\mathcal{J}}_f$, Ohmic current $\boldsymbol{J}_{\mathcal{O}} = \gamma \boldsymbol{E}$, Lorentz's current $\boldsymbol{J}_{\mathcal{L}} = \gamma(\boldsymbol{v} \times \boldsymbol{B})$ and volume charge current $\boldsymbol{J}_\Omega = q\boldsymbol{v}$, when using a Eulerian (fixed) laboratory frame. For the case of non-polarisable and non-magnetisable conductive materials (as it is typically the case in a MRI scanner), with no volume charge density, it is appropriate to assume that $\boldsymbol{M} = \boldsymbol{0}$, $\boldsymbol{P} = \boldsymbol{0}$ and $q = 0$. As a result, substitution of (4), (6) and (8) into (1a) and (2a), result in

$$\nabla \cdot \boldsymbol{E} = 0, \tag{9a}$$

$$\frac{1}{\mu_0}\nabla \times \boldsymbol{B} = \boldsymbol{J}_f + \boldsymbol{J}_{\mathcal{O}} + \boldsymbol{J}_{\mathcal{L}} + \varepsilon_0 \left.\frac{\partial \boldsymbol{E}}{\partial t}\right|_{\boldsymbol{x}}. \tag{9b}$$

Moreover, in the case of low frequency time-varying electro-magnetic fields and highly conducting components, the last term on the right hand side of (9b) can be considered negligible with respect to the sum of the rest of the contributions (see References [13]) and leads to the **eddy current approximation** where (9b) reduces to

$$\frac{1}{\mu_0}\nabla \times \boldsymbol{B} = \boldsymbol{J}_f + \boldsymbol{J}_{\mathcal{O}} + \boldsymbol{J}_{\mathcal{L}}. \tag{10}$$

By inspecting (10), it is clear that the overall right hand is a solenoidal vector field and so must be their individual components (by considering complementary cases with $\boldsymbol{J}_f = \boldsymbol{0}$, $\gamma = 0$ in $\boldsymbol{J}_{\mathcal{O}}$ or $\boldsymbol{v} = \boldsymbol{0}$ in $\boldsymbol{J}_{\mathcal{L}}$), thus

$$\nabla \cdot \boldsymbol{J}_f = 0; \tag{11a}$$

$$\nabla \cdot \boldsymbol{J}_{\mathcal{O}} = 0; \tag{11b}$$

$$\nabla \cdot \boldsymbol{J}_{\mathcal{L}} = 0. \tag{11c}$$

In addition, away from supp($\boldsymbol{J}_f$), supp($\boldsymbol{J}_{\mathcal{O}}$) and supp($\boldsymbol{J}_{\mathcal{L}}$), the fields decay as

$$\boldsymbol{E} = O\left(\frac{1}{|\boldsymbol{x}|}\right); \tag{12a}$$

$$\boldsymbol{H} = O\left(\frac{1}{|\boldsymbol{x}|}\right); \tag{12b}$$

as $|\boldsymbol{x}| \to \infty$. Eq. (9a), (10), (2b), (1d), (11), (12) summarise the set of electro-magnetic equations to be further considered.

---

[3] Notice how the Ohmic contribution is typically defined in the Updated Lagrangian description (hence the use of calligraphic symbol).

2.2. Mechanics

In the presence of a transient magnetic field, the radiation shields and OVC (Outer Vacuum Chamber) in an MRI scanner, which are comprised of conductive materials, experience deformations. In addition to this, the MRI scanner may undergo external vibrations, such as floor-borne vibrations, which will cause relative movement between the superconducting coils of the scanner and the conducting shields, also causing the components to experience deformations. Under the deformation mapping $\boldsymbol{\phi}$, the conservation of mass, linear momentum and angular momentum, can be collectively presented in an Updated Lagrangian description as

$$\overset{\diamond}{\rho} = 0, \tag{13a}$$

$$\overset{\diamond}{\boldsymbol{p}} = \boldsymbol{f} + \boldsymbol{\nabla} \cdot \boldsymbol{\sigma}, \tag{13b}$$

$$\overset{\diamond}{\boldsymbol{W}} = \boldsymbol{x} \times \boldsymbol{f} + \boldsymbol{\nabla} \cdot (\boldsymbol{x} \times \boldsymbol{\sigma}), \tag{13c}$$

where ρ is the mass density in the current configuration, $\boldsymbol{p}$ denotes the linear momentum per unit of current volume, $\boldsymbol{f}$ is a body force per unit of current volume, $\boldsymbol{\sigma}$ is the Cauchy stress tensor, $\boldsymbol{W} = \boldsymbol{x} \times \boldsymbol{p}$ is the angular momentum per unit of current volume, symbol $\times$ denotes the left cross product between a vector and a second order tensor [40] and the upper symbol $\diamond$ denotes the convective density derivative[4]. An alternative insightful expression[5] for the conservation of angular momentum (13c) is

$$\boldsymbol{\varepsilon} : \boldsymbol{\sigma} + \boldsymbol{v} \times \boldsymbol{p} = \boldsymbol{0}, \tag{14}$$

where the linear momentum $\boldsymbol{p}$ can be shown to be [30]

$$\boldsymbol{p} = \boldsymbol{p}_m + \boldsymbol{p}_{\infty}^{EM}; \tag{15a}$$

$$\boldsymbol{p}_m = \rho \boldsymbol{v}; \tag{15b}$$

$$\boldsymbol{p}_{\infty}^{EM} = \boldsymbol{D}_{\infty} \times \boldsymbol{B}, \tag{15c}$$

with $\boldsymbol{p}_m$ the kinematic linear momentum contribution and $\boldsymbol{p}_{\infty}^{EM}$ the electromagnetic contribution. Similarly, the Cauchy stress tensor, in the absence of polarisation and magnetisation can be shown to be [30]

$$\boldsymbol{\sigma} = \boldsymbol{\sigma}_m + \boldsymbol{\sigma}_{\infty}^{EM} + \boldsymbol{p}_{\infty}^{EM} \otimes \boldsymbol{v}, \tag{16}$$

where

$$\boldsymbol{\sigma}_{\infty}^{EM} = \boldsymbol{\sigma}_{\infty}^{E} + \boldsymbol{\sigma}_{\infty}^{M}; \tag{17a}$$

$$\boldsymbol{\sigma}_{\infty}^{E} = \varepsilon_0 \Big(\boldsymbol{E} \otimes \boldsymbol{E} - \frac{1}{2} (\boldsymbol{E} \cdot \boldsymbol{E}) \boldsymbol{I} \Big); \tag{17b}$$

$$\boldsymbol{\sigma}_{\infty}^{M} = \frac{1}{\mu_0} \Big(\boldsymbol{B} \otimes \boldsymbol{B} - \frac{1}{2} (\boldsymbol{B} \cdot \boldsymbol{B}) \boldsymbol{I} \Big), \tag{17c}$$

where $\boldsymbol{\sigma}_m$ denotes a deformation activated contribution, $\boldsymbol{\sigma}_{\infty}^{EM}$ is the so-called **Maxwell stress tensor** (in the vacuum) and $\boldsymbol{p}_{\infty}^{EM} \otimes \boldsymbol{v}$ is the **electromagnetic momentum** contribution. Substitution of (15) and (16) into (14) leads to the symmetry of the stress contribution $\boldsymbol{\sigma}_m$. Moreover, substitution of (15) and (16) into (13b) renders

$$\overset{\diamond}{\boldsymbol{p}}_m + \overset{\diamond}{\boldsymbol{p}}{}_{\infty}^{EM} = \boldsymbol{f} + \boldsymbol{\nabla} \cdot (\boldsymbol{\sigma}_m + \boldsymbol{\sigma}_{\infty}^{EM} + \boldsymbol{p}_{\infty}^{EM} \otimes \boldsymbol{v}), \tag{18}$$

where after application of the conservation of mass (13a) and the property of the convective density derivative $\overset{\diamond}{\boldsymbol{S}} = \frac{\partial \boldsymbol{S}}{\partial t}\Big|_{\boldsymbol{x}} + \boldsymbol{\nabla} \cdot (\boldsymbol{S} \otimes \boldsymbol{v})$, it yields

$$\rho \boldsymbol{a} = \boldsymbol{f} + \boldsymbol{\nabla} \cdot (\boldsymbol{\sigma}_m + \boldsymbol{\sigma}_{\infty}^{EM}) - \frac{\partial \boldsymbol{p}_{\infty}^{EM}}{\partial t}\bigg|_{\boldsymbol{x}}; \qquad \boldsymbol{a} = \frac{\partial \boldsymbol{v}}{\partial t}\bigg|_{\boldsymbol{X}}. \tag{19}$$

Finally, substitution of (15), (17b) and (17c) into (19), and after some algebra, it renders

$$\rho \boldsymbol{a} = \boldsymbol{\nabla} \cdot \boldsymbol{\sigma}_m + \boldsymbol{f} + \boldsymbol{f}^{EM}; \tag{20a}$$

$$\boldsymbol{f}^{EM} = \boldsymbol{f}_{f}^{EM} + \boldsymbol{f}_{\mathcal{O}}^{EM} + \boldsymbol{f}_{\mathcal{L}}^{EM}, \tag{20b}$$

where

$$\boldsymbol{f}_{f}^{EM} = \boldsymbol{J}_f \times \boldsymbol{B}; \tag{21a}$$

$$\boldsymbol{f}_{\mathcal{O}}^{EM} = \boldsymbol{J}_{\mathcal{O}} \times \boldsymbol{B}; \tag{21b}$$

$$\boldsymbol{f}_{\mathcal{L}}^{EM} = \boldsymbol{J}_{\mathcal{L}} \times \boldsymbol{B}. \tag{21c}$$

---

[4] The convective density derivative of a vector field $\boldsymbol{S}$ is defined as $\overset{\diamond}{\boldsymbol{S}} = \frac{1}{J} \frac{\partial (J\boldsymbol{S})}{\partial t}\Big|_{\boldsymbol{X}}$.

[5] From the substitution of (13a)-(13b) into (13c).

Above (20) provides an alternative formulation to that of (13b) exploiting the use of an equivalent electromagnetic body force $\boldsymbol{f}^{EM}$, suitable for smooth type problems, in contrast to the more generic (13b) also suitable to non-smooth type problems (with associated jump or interface conditions). It is interesting to notice how the three components of the body force $\boldsymbol{f}^{EM}$ match their counterparts in the electric current $\boldsymbol{J}$ in (10). Considering the **eddy current approximation**, it is appropriate to disregard the stress contributions $\boldsymbol{\sigma}_\infty^E$ and $\boldsymbol{p}_\infty^{EM} \otimes \boldsymbol{v}$ in comparison with $\boldsymbol{\sigma}_m + \boldsymbol{\sigma}_\infty^M$ and, as a result, the conservation of linear momentum (19) reduces to

$$\rho \boldsymbol{a} = \boldsymbol{f} + \boldsymbol{\nabla} \cdot (\boldsymbol{\sigma}_m + \boldsymbol{\sigma}_\infty^M). \tag{22}$$

It is clear that the above conservation of linear momentum (22) is redundant in the non-conducting region, where (18) degenerates into

$$\left.\frac{\partial \boldsymbol{p}_\infty^{EM}}{\partial t}\right|_{\boldsymbol{x}} = \boldsymbol{\nabla} \cdot \sigma_\infty^{EM}, \tag{23}$$

which is implicitly fulfilled if Maxwell equations are verified. Moreover, in regions where $\boldsymbol{J}_f$ vanishes (or is time-independent), above equation reduces even further to the well-known solenoidal condition of the Maxwell stress tensor $\boldsymbol{\nabla} \cdot \boldsymbol{\sigma}_\infty^{EM} = \boldsymbol{0}$. Under the consideration of a **time-independent** problem, $\boldsymbol{E} = \boldsymbol{0}$ and $\boldsymbol{v} = \boldsymbol{0}$, and thus, Ohmic $\boldsymbol{f}_{\mathcal{O}}^{EM}$ and Lorentz's $\boldsymbol{f}_{\mathcal{L}}^{EM}$ forces can be easily seen to vanish (see (21)). Moreover, within a conductive region outside the support of the current $\boldsymbol{J}_f$, the current force $\boldsymbol{f}_f^{EM}$ vanishes as well (see (21)). Therefore, in the absence of other body forces $\boldsymbol{f}$, the stress $\boldsymbol{\sigma}_m$ must be solenoidal. Moreover, in the **vacuum** where $\boldsymbol{J}_{\mathcal{O}} = \boldsymbol{J}_{\mathcal{L}} = \boldsymbol{0}$ and outside the support of $\boldsymbol{J}_f$, that is, $\boldsymbol{J}_f = \boldsymbol{0}$, the electromagnetic force $\boldsymbol{f}^{EM} = \boldsymbol{0}$, and thus the Maxwell stress tensor is solenoidal (self-equilibrated). Furthermore, under the consideration of a **time-independent** problem, within a conductive region outside the support of the current $\boldsymbol{J}_f$, in the absence of any other body forces $\boldsymbol{f}$, and provided homogeneous prescribed boundary conditions $\boldsymbol{u}_D = \boldsymbol{0}$, the displacements $\boldsymbol{u}$ vanish and thus the stresses $\boldsymbol{\sigma}_m = \boldsymbol{0}$. For the application of interest, where small strains apply, (13a) is redundant as it can be simplified to the assumption that ρ remains constant and not a function of time, as the Jacobian $J \approx 1$. Moreover, linearised elasticity (i.e. suitable in the case of small strains and displacements) is used to define $\boldsymbol{\sigma}_m$ as

$$\boldsymbol{\sigma}_m = \lambda \operatorname{Tr} \boldsymbol{\epsilon} \boldsymbol{I} + 2G\boldsymbol{\epsilon}, \tag{24}$$

where λ and G are the Lamé coefficients and

$$\boldsymbol{\epsilon} = \frac{1}{2}(\boldsymbol{G} + \boldsymbol{G}^T); \tag{25a}$$

$$\boldsymbol{G} = \boldsymbol{\nabla}\boldsymbol{u}, \tag{25b}$$

where $\boldsymbol{\epsilon}$ is the small strain tensor and $\boldsymbol{G}$ the displacement gradient tensor[6]. Therefore, (17c) and (22) (or alternatively (20)–(21)), along with (24), (25) constitute the mechanical governing equations to be taken forward.

2.3. Coupled initial boundary value problem

Consider that $\Omega_c \subset \mathbb{R}^3$ represents a conducting subregion, with complementary non-conducting subregion $\mathbb{R}^3 \setminus \overline{\Omega_c}$ (i.e. $\gamma = 0$), and introduce $\partial\Omega_c$ as the interface between both subdomains with unit normal defined as $\boldsymbol{n}|_{\partial\Omega_c}$ selected to be pointing towards the non-conducting region. This boundary may be divided into Dirichlet and Neumann parts, defined by $\partial\Omega_c = \overline{\partial\Omega_c^D} \cup \overline{\partial\Omega_c^N}$ and $\partial\Omega_c^D \cap \partial\Omega_c^N = \emptyset$, where $\partial\Omega_c^D$ denotes the part of the boundary on the conducting subdomain with Dirichlet boundary conditions applied, and $\partial\Omega_c^N$ denotes the part of the boundary on the conducting subdomain with Neumann boundary conditions applied[7] As it is customary for computational treatment [30,35,41], we introduce a vector potential $\boldsymbol{A}$ such that

$$\boldsymbol{B} = \boldsymbol{\nabla} \times \boldsymbol{A}; \tag{26a}$$

$$\boldsymbol{E} = -\left.\frac{\partial \boldsymbol{A}}{\partial t}\right|_{\boldsymbol{x}}, \tag{26b}$$

which ensures satisfaction of (2b) and (1d) by construction. Moreover, to guarantee uniqueness of $\boldsymbol{A}$ and hence solvability, Coulomb gauging (i.e. $\boldsymbol{\nabla} \cdot \boldsymbol{A} = 0$) is enforced in the non-conducting region. We are now in a position to present the coupled Initial Boundary Value Problem, which can be described by the **transmission problem**: Find $(\boldsymbol{A}(t), \boldsymbol{u}(t)) \in \mathbb{R}^3(0, t_{\max}] \times \mathbb{R}^3(0, t_{\max}]$ such that

$$\boldsymbol{\nabla} \cdot \boldsymbol{A} = 0; \qquad \text{in } \mathbb{R}^3 \setminus \overline{\Omega_c}, \tag{27a}$$

$$\boldsymbol{\nabla} \times {\mu_0}^{-1} \boldsymbol{\nabla} \times \boldsymbol{A} = \boldsymbol{J}_f; \qquad \text{in } \mathbb{R}^3 \setminus \overline{\Omega_c}, \tag{27b}$$

$$\boldsymbol{\nabla} \cdot \boldsymbol{J}_f = 0; \qquad \text{in } \mathbb{R}^3, \tag{27c}$$

$$\boldsymbol{\nabla} \times \mu_0^{-1} \boldsymbol{\nabla} \times \boldsymbol{A} = -\gamma \left.\frac{\partial \boldsymbol{A}}{\partial t}\right|_{\boldsymbol{x}} + \boldsymbol{J}_{\mathcal{L}} + \boldsymbol{J}_f; \qquad \text{in } \Omega_c, \tag{27d}$$

$$\boldsymbol{\nabla} \cdot \boldsymbol{J}_{\mathcal{L}} = 0; \qquad \text{in } \Omega_c, \tag{27e}$$

$$[\boldsymbol{n}|_{\partial\Omega_c} \times \boldsymbol{A}] = \boldsymbol{0}; \qquad \text{on } \partial\Omega_c, \tag{27f}$$

---

[6] Due to the further assumption of small displacements, no distinction is needed between spatial (current) and material (initial) gradient [12] in the above definition of the displacement gradient tensor $\boldsymbol{G}$.

[7] In the case of a Neumann boundary, interface or transmission conditions will be applied unless otherwise stated.

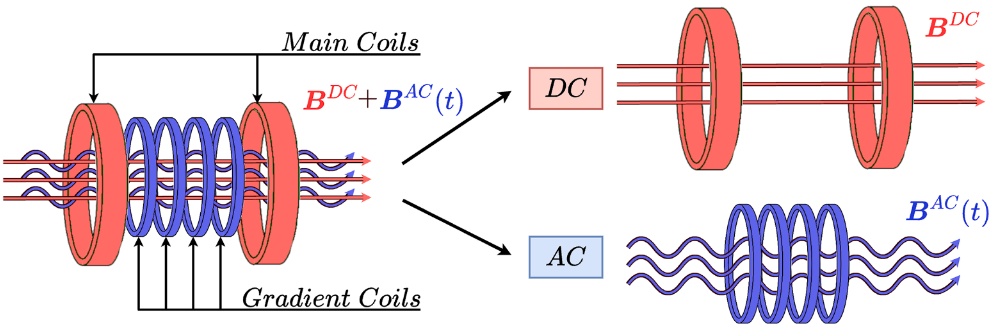

Fig. 2. Current source decomposition between main and gradient coils $\boldsymbol{J}_f(t) = \boldsymbol{J}_f^{DC} + \boldsymbol{J}_f^{AC}(t)$ with their corresponding magnetic fields $\boldsymbol{B}(t) = \boldsymbol{B}^{DC} + \vec{B}^{AC}(t)$.

$$[\boldsymbol{n}|_{\partial\Omega_c} \times \mu_0^{-1}(\nabla \times \boldsymbol{A})] = \boldsymbol{0}; \qquad \text{on } \partial\Omega_c, \tag{27g}$$

$$\boldsymbol{A} = O(|\boldsymbol{x}|^{-1}); \qquad \text{as } |\boldsymbol{x}| \to \infty, \tag{27h}$$

$$\boldsymbol{A}|_{t=0} = \boldsymbol{0}; \qquad \text{in } \mathbb{R}^3, \tag{27i}$$

$$\rho\boldsymbol{a} - \nabla \cdot \boldsymbol{\sigma}_m = \boldsymbol{f} + \nabla \cdot \boldsymbol{\sigma}_\infty^M; \qquad \text{in } \Omega_c, \tag{27j}$$

$$[\boldsymbol{v}] = \boldsymbol{0}; \qquad \text{on } \partial\Omega_c, \tag{27k}$$

$$[\boldsymbol{\sigma}_\infty^M \boldsymbol{n}|_{\partial\Omega_c}] = \boldsymbol{\sigma}_m \boldsymbol{n}|_{\partial\Omega_c}; \qquad \text{on } \partial\Omega_c, \tag{27l}$$

$$\boldsymbol{u} = \boldsymbol{u}_D; \qquad \text{on } \partial\Omega_c^D, \tag{27m}$$

$$\boldsymbol{u}|_{t=0} = \boldsymbol{v}|_{t=0} = \boldsymbol{0}; \qquad \text{in } \Omega_c, \tag{27n}$$

where (27a) is the Coulomb gauge; (27b) and (27d) are (10) re-written in terms of the vector potential $\boldsymbol{A}$ in non-conducting and conducting regions of the domain, respectively; (27c) and (27e) are the solenoidal constraints on the current sources, (27f)–(27g) represent interface conditions for the electro-magnetic equations where $[\bullet]$ denotes the jump operator; (27h) is the far field condition; (27j) is the conservation of linear momentum; (27k) and (27l) are the interface conditions for the mechanical equations; (27m) is a displacement imposed condition on the Dirichlet portion of the boundary of the conductor, and (27i) and (27n) are the initial conditions.

Note how (27d) allows for the combined modelling of Ohmic, Lorentz's and free currents simultaneously, namely, main and gradient coils can be treated as both magnets and conducting components simultaneously[8] It is interesting to notice that the non-trivial solution for $\boldsymbol{A}$ is obtained when either $\boldsymbol{J}_f$ or $\boldsymbol{J}_\mathcal{L}$ are non zero. The former case leads to magnetic fields as a result of the action of **gradient coils** subjected to a non-zero time-dependent current $\boldsymbol{J}_f \neq \boldsymbol{0}$, whilst the latter case results in magnetic fields induced by **mechanical vibrations** ($\boldsymbol{v} \neq \boldsymbol{0}$) of conductive ($\gamma > 0$) regions. These mechanical vibrations can be either directly actuated (i.e. **floor-borne vibrations**) or indirectly generated by the vibrations induced by the presence of **underlying electromagnetic stresses**.

3. DC-AC splitting with and without linearisation

Closed bore MRI scanners have two types of magnetic field generating coils, namely, (i) **superconducting main coils** that generate a strong static magnetic field and (ii) **resistive gradient coils** that generate low strength transient magnetic fields [42]. As a result, the time dependent current source $\boldsymbol{J}_f(t)$ can be decomposed as $\boldsymbol{J}_f(t) = \boldsymbol{J}_f^{DC} + \boldsymbol{J}_f^{AC}(t)$, where $\boldsymbol{J}_f^{DC}$ corresponds to the static current source imposed on the main magnetic coils and $\boldsymbol{J}_f^{AC}(t)$ denotes the transient current source imposed on the resistive gradient coils. The splitting applies to the transmission problem (27) with unknown total fields $\boldsymbol{A}(t)$ and $\boldsymbol{u}(t)$, resulting in the counterpart decomposition (see Fig. 2) given by

$$\boldsymbol{u}(t) = \boldsymbol{u}^{DC} + \boldsymbol{u}^{AC}(t); \tag{28a}$$

$$\boldsymbol{A}(t) = \boldsymbol{A}^{DC} + \boldsymbol{A}^{AC}(t). \tag{28b}$$

3.1. DC boundary value problem

Following the above decomposition, we introduce a **time-independent transmission problem** for the case where the electric current is simply $\boldsymbol{J}_f^{DC}$ as follows: Find $\boldsymbol{A}^{DC} \in \mathbb{R}^3$ such that

$$\nabla \cdot \boldsymbol{A}^{DC} = 0; \qquad \text{in } \mathbb{R}^3, \tag{29a}$$

---

[8] Existing literature typically considers the support of the free current as non-overlapping to that of the Lorentz's and Ohmic currents, that is, the so-called Biot-Savart assumption[30].

$$\nabla \times \mu_0^{-1} \nabla \times \boldsymbol{A}^{DC} = \boldsymbol{J}_f^{DC}; \qquad \text{in } \mathbb{R}^3 \setminus \Omega_c, \tag{29b}$$

$$\nabla \cdot \boldsymbol{J}_f^{DC} = 0; \qquad \text{in } \mathbb{R}^3, \tag{29c}$$

$$\nabla \times \mu_0^{-1} \nabla \times \boldsymbol{A}^{DC} = \boldsymbol{J}_f^{DC}; \qquad \text{in } \Omega_c, \tag{29d}$$

$$\boldsymbol{A}^{DC} = O(|\boldsymbol{x}|^{-1}); \qquad \text{as } |\boldsymbol{x}| \to \infty, \tag{29e}$$

$$[\boldsymbol{n}_{\partial\Omega_c} \times \boldsymbol{A}^{DC}] = \boldsymbol{0}; \qquad \text{on } \partial\Omega_c, \tag{29f}$$

$$[\boldsymbol{n}_{\partial\Omega_c} \times \mu_0^{-1}(\nabla \times \boldsymbol{A}^{DC})] = \boldsymbol{0}; \qquad \text{on } \partial\Omega_c. \tag{29g}$$

As the above DC transmission problem (29) is static in nature, no time-dependent terms feature. In the usual case where the main coils are idealised as Biot-Savart current sources, and with the further absence of mechanical body forces, tractions and prescribed boundary displacements, the displacement field vanishes, that is, $\boldsymbol{u}^{DC} = \boldsymbol{0}$ and hence is not solved for. The solenoidal constraint (29c) is typically enforced due to the axisymmetric nature of the main coils, making this constraint redundant. Maxwell stresses $\boldsymbol{\sigma}_\infty^M = \boldsymbol{\sigma}_\infty^M(\boldsymbol{A}^{DC})$ are solenoidal (i.e. self-equilibrated) everywhere, displacements trivially vanish and so the stresses $\boldsymbol{\sigma}_m = \boldsymbol{0}$, and the Coulomb gauge (29a) must extend across the entire domain.

Remark 1. In the special case where the main coils are treated as homogenised[9] deformable components, the conservation of linear momentum reduces to

$$\nabla \cdot \boldsymbol{\sigma}_m = -\boldsymbol{J}_f^{DC} \times (\nabla \times \boldsymbol{A}^{DC}), \tag{30}$$

which decouples from the rest of the Boundary value Problem (29) and can thus be solved subsequently. Traditionally, main coils are not slender components and the strains induced via (30) can be safely neglected. Furthermore, provided the assumption of small strains and linearised elasticity (24) holds, the DC mechanical problem does not intervene in the following AC problem and therefore its solution is deemed unnecessary[10]

3.2. AC initial boundary value problem

It is now possible to introduce a transient transmission problem such that its solution is given by the fields $(\boldsymbol{A}(t), \boldsymbol{u}(t))$, where the upper index $(\cdot)^{AC}$ has been removed henceforth for simplicity. Specifically, Find $(\boldsymbol{A}(t), \boldsymbol{u}(t)) \in \mathbb{R}^3(0, t_{\max}] \times \mathbb{R}^3(0, t_{\max}]$ such that

$$\nabla \cdot \boldsymbol{A} = 0; \qquad \text{in } \mathbb{R}^3 \setminus \overline{\Omega_c}, \tag{31a}$$

$$\nabla \times \mu_0^{-1} \nabla \times \boldsymbol{A} = \boldsymbol{J}_f^{AC}; \qquad \text{in } \mathbb{R}^3 \setminus \overline{\Omega_c}, \tag{31b}$$

$$\nabla \cdot \boldsymbol{J}_f^{AC} = 0; \qquad \text{in } \mathbb{R}^3, \tag{31c}$$

$$\nabla \times \mu_0^{-1} \nabla \times \boldsymbol{A} = -\gamma \left.\frac{\partial \boldsymbol{A}}{\partial t}\right|_{\boldsymbol{x}} + \boldsymbol{J}_{\mathcal{L}} + \boldsymbol{J}_f^{AC}; \qquad \text{in } \Omega_c, \tag{31d}$$

$$\nabla \cdot \boldsymbol{J}_{\mathcal{L}} = 0; \qquad \text{in } \Omega_c, \tag{31e}$$

$$[\boldsymbol{n}|_{\partial\Omega_c} \times \boldsymbol{A}] = \boldsymbol{0}; \qquad \text{on } \partial\Omega_c, \tag{31f}$$

$$[\boldsymbol{n}|_{\partial\Omega_c} \times \mu_0^{-1}(\nabla \times \boldsymbol{A})] = \boldsymbol{0}; \qquad \text{on } \partial\Omega_c, \tag{31g}$$

$$\boldsymbol{A} = O(||\boldsymbol{x}|^{-1}); \qquad \text{as } |\boldsymbol{x}| \to \infty, \tag{31h}$$

$$\boldsymbol{A}|_{t=0} = \boldsymbol{0}; \qquad \text{in } \mathbb{R}^3, \tag{31i}$$

$$\rho \boldsymbol{a} - \nabla \cdot \boldsymbol{\sigma}_m = \nabla \cdot \boldsymbol{\tau}_\infty; \qquad \text{in } \Omega_c, \tag{31j}$$

$$[\boldsymbol{v}] = \boldsymbol{0}; \qquad \text{on } \partial\Omega_c, \tag{31k}$$

$$[\boldsymbol{\tau}_\infty \boldsymbol{n}|_{\partial\Omega_c}] = \boldsymbol{\sigma}_m \boldsymbol{n}|_{\partial\Omega_c}; \qquad \text{on } \partial\Omega_c, \tag{31l}$$

$$\boldsymbol{u} = \boldsymbol{u}_D; \qquad \text{on } \partial\Omega_c^D \tag{31m}$$

$$\boldsymbol{u}|_{t=0} = \boldsymbol{v}|_{t=0} = \boldsymbol{0}; \qquad \text{in } \Omega_c, \tag{31n}$$

where no mechanical body forces are considered, and $\boldsymbol{\tau}_\infty = \boldsymbol{\tau}_\infty(\boldsymbol{A}^{DC}, \boldsymbol{A})$ represents an **incremental Maxwell stress tensor** defined as

$$\boldsymbol{\tau}_\infty(\boldsymbol{A}^{DC}, \boldsymbol{A}) = \boldsymbol{\sigma}_\infty^M(\boldsymbol{A}^{DC} + \boldsymbol{A}) - \boldsymbol{\sigma}_\infty^M(\boldsymbol{A}^{DC}), \tag{32}$$

which can be expanded to yield

$$\begin{aligned} \boldsymbol{\tau}_\infty(\boldsymbol{A}^{DC}, \boldsymbol{A}) = {} & \mu_0^{-1}(\boldsymbol{B}^{DC} \otimes (\nabla \times \boldsymbol{A}) + (\nabla \times \boldsymbol{A}) \otimes \boldsymbol{B}^{DC} - (\boldsymbol{B}^{DC} \cdot (\nabla \times \boldsymbol{A}))\boldsymbol{I}) \\ & + \mu_0^{-1}((\nabla \times \boldsymbol{A}) \otimes (\nabla \times \boldsymbol{A}) - \frac{1}{2}(\nabla \times \boldsymbol{A}) \cdot (\nabla \times \boldsymbol{A})\boldsymbol{I}), \end{aligned} \tag{33}$$

---

[9] Homogeneisation of multiple materials is typically used due to the different scales comprised in the problem [54].

[10] Otherwise, if large deformations hold [55] and a non-linear constitutive relationship is applied, appropriate linearisation of the mechanical constitutive law would lead to the classical deformation dependent fourth order tensor.

where $\boldsymbol{B}^{DC} = \nabla \times \boldsymbol{A}^{DC}$. As expected, simple addition of transmission problems (29) and (31) result in the original transmission problem (27).

Remark 2. The main coils, operating under cryogenic conditions, are typically modelled without the consideration of any Ohmic effect due to their superconductivity behaviour, that is, $\left.\frac{\partial \boldsymbol{A}}{\partial t}\right|_{\boldsymbol{x}} \to 0$ as $\gamma \to \infty$.

Careful inspection of the incremental Maxwell stress tensor $\boldsymbol{\tau}^{M}_{\infty}(\boldsymbol{A}^{DC}, \boldsymbol{A})$ shows its non-linearity with respect to the AC vector potential $\boldsymbol{A}$ (refer to the second line of (33)). Taking advantage of the large difference in magnitude between magnetic AC and DC fields (i.e. $|\nabla \times \boldsymbol{A}| << |\nabla \times \boldsymbol{A}^{DC}|$), authors in [13] propose the following **linearised approximation for the incremental Maxwell stress tensor**

$$\boldsymbol{\tau}_{\infty}(\boldsymbol{A}^{DC}, \boldsymbol{A}) \approx \boldsymbol{\tau}^{\text{lin}}_{\infty}(\boldsymbol{A}^{DC}, \boldsymbol{A}) := D(\boldsymbol{\sigma}^{M}_{\infty}(\boldsymbol{A}))\Big|_{\boldsymbol{A}^{DC}}[\boldsymbol{A}], \tag{34}$$

where the last term on the right hand side of (34) denotes the directional derivative[11] of the Maxwell stress tensor (evaluated at $\boldsymbol{A}^{DC}$) with respect to a vector potential perturbation given by $\boldsymbol{A}$, which yields

$$\boldsymbol{\tau}^{\text{lin}}_{\infty}(\boldsymbol{A}^{DC}, \boldsymbol{A}) = \mu_0^{-1}(\boldsymbol{B}^{DC} \otimes (\nabla \times \boldsymbol{A}) + (\nabla \times \boldsymbol{A}) \otimes \boldsymbol{B}^{DC} - (\boldsymbol{B}^{DC} \cdot (\nabla \times \boldsymbol{A}))\boldsymbol{I}), \tag{35}$$

which is indeed linear with respect to the curl of the AC vector potential $\boldsymbol{A}$ and can be re-written in a more compact manner as

$$\boldsymbol{\tau}^{\text{lin}}_{\infty}(\boldsymbol{A}^{DC}, \boldsymbol{A}) = \boldsymbol{\mathcal{S}}^{DC}(\nabla \times \boldsymbol{A}), \tag{36}$$

where $\boldsymbol{\mathcal{S}}^{DC}$ is a *constitutive-like third order tensor* dependent upon the magnetic field $\boldsymbol{B}^{DC}$ (i.e. $\boldsymbol{\mathcal{S}}^{DC} = \boldsymbol{\mathcal{S}}^{DC}(\boldsymbol{B}^{DC})$) and defined as

$$[\boldsymbol{\mathcal{S}}^{DC}]_{ijk} = \mu_0^{-1}(B^{DC}_i \delta_{jk} + B^{DC}_j \delta_{ik} - \delta_{ij} B^{DC}_k), \tag{37}$$

with δ_{ij} the Kronecker delta coefficient and Einstein notation has been assumed. Analogously, the **Lorentz's current term $\boldsymbol{J}_{\mathcal{L}}(\boldsymbol{v}, \boldsymbol{A}^{DC}, \boldsymbol{A})$ can also be linearised** by neglecting the nonlinear coupled term between the velocity and the AC vector potential $\boldsymbol{A}$ as

$$\boldsymbol{J}_{\mathcal{L}}(\boldsymbol{v}, \boldsymbol{A}^{DC}, \boldsymbol{A}) = \gamma \boldsymbol{v} \times (\nabla \times \boldsymbol{A}^{DC}) + \gamma \boldsymbol{v} \times (\nabla \times \boldsymbol{A}) \approx \gamma \boldsymbol{v} \times (\nabla \times \boldsymbol{A}^{DC}) := \boldsymbol{J}^{\text{lin}}_{\mathcal{L}}(\boldsymbol{v}, \boldsymbol{A}^{DC}). \tag{38}$$

It is now possible to introduce a **linearised AC transient transmission problem** in terms of unknown fields $(\boldsymbol{A}(t), \boldsymbol{u}(t))$ as follows: Find $(\boldsymbol{A}(t), \boldsymbol{u}(t)) \in \mathbb{R}^3 \times \mathbb{R}^3$ such that

$$\nabla \cdot \boldsymbol{A} = 0; \qquad \text{in } \mathbb{R}^3 \setminus \overline{\Omega_c}, \tag{39a}$$

$$\nabla \times \mu_0^{-1} \nabla \times \boldsymbol{A} = \boldsymbol{J}^{AC}_f; \qquad \text{in } \mathbb{R}^3 \setminus \overline{\Omega_c}, \tag{39b}$$

$$\nabla \cdot \boldsymbol{J}^{AC}_f = 0; \qquad \text{in } \mathbb{R}^3, \tag{39c}$$

$$\nabla \times \mu_0^{-1} \nabla \times \boldsymbol{A} = -\gamma \left.\frac{\partial \boldsymbol{A}}{\partial t}\right|_{\boldsymbol{x}} + \boldsymbol{J}^{\text{lin}}_{\mathcal{L}} + \boldsymbol{J}^{AC}_f; \qquad \text{in } \Omega_c, \tag{39d}$$

$$\nabla \cdot \boldsymbol{J}^{\text{lin}}_{\mathcal{L}} = 0; \qquad \text{in } \Omega_c, \tag{39e}$$

$$[\boldsymbol{n}|_{\partial\Omega_c} \times \boldsymbol{A}] = \boldsymbol{0}; \qquad \text{on } \partial\Omega_c, \tag{39f}$$

$$[\boldsymbol{n}|_{\partial\Omega_c} \times \mu_0^{-1}(\nabla \times \boldsymbol{A})] = \boldsymbol{0}; \qquad \text{on } \partial\Omega_c, \tag{39g}$$

$$\boldsymbol{A} = O(|\boldsymbol{x}|^{-1}); \qquad \text{as } |\boldsymbol{x}| \to \infty, \tag{39h}$$

$$\boldsymbol{A}|_{t=0} = \boldsymbol{0}; \qquad \text{in } \mathbb{R}^3, \tag{39i}$$

$$\rho \boldsymbol{a} - \nabla \cdot \boldsymbol{\sigma}_m = \nabla \cdot \boldsymbol{\tau}^{\text{lin}}_{\infty}; \qquad \text{in } \Omega_c, \tag{39j}$$

$$[\boldsymbol{v}] = \boldsymbol{0}; \qquad \text{on } \partial\Omega_c, \tag{39k}$$

$$[\boldsymbol{\tau}^{\text{lin}}_{\infty} \boldsymbol{n}|_{\partial\Omega_c}] = \boldsymbol{\sigma}_m \boldsymbol{n}|_{\partial\Omega_c}; \qquad \text{on } \partial\Omega_c, \tag{39l}$$

$$\boldsymbol{u} = \boldsymbol{u}_D; \qquad \text{on } \partial\Omega^D_c \tag{39m}$$

$$\boldsymbol{u}|_{t=0} = \boldsymbol{v}|_{t=0} = \boldsymbol{0}; \qquad \text{in } \Omega_c. \tag{39n}$$

As can be observed, the differences between the AC transmission problems (31) and (39) correspond to the use of the pairs $\{\boldsymbol{\tau}_{\infty}, \boldsymbol{J}_{\mathcal{L}}\}$ or $\{\boldsymbol{\tau}^{\text{lin}}_{\infty}, \boldsymbol{J}^{\text{lin}}_{\mathcal{L}}\}$, for the general or linearised versions, respectively. Sequential solution of transmission problems (29) and (31) (or its linearised version (39)) enables the computation of the derived fields[12]

$$\boldsymbol{B} = \nabla \times \boldsymbol{A}^{DC} + \nabla \times \boldsymbol{A}; \tag{40a}$$

$$\boldsymbol{E} = -\left.\frac{\partial \boldsymbol{A}}{\partial t}\right|_{\boldsymbol{x}}, \tag{40b}$$

$$\boldsymbol{\mathcal{E}} = \boldsymbol{E} + \boldsymbol{v} \times \boldsymbol{B}. \tag{40c}$$

---

[11] The directional derivative of a tensor-valued function $\mathcal{F}(\boldsymbol{S})$ with respect to a direction $\boldsymbol{U}$, and evaluated at $\boldsymbol{T}$, is defined by $D(\mathcal{F}(\boldsymbol{S}))|_{\boldsymbol{T}}[\boldsymbol{U}] = \left.\frac{d\mathcal{F}(\boldsymbol{T}+\epsilon\boldsymbol{U})}{d\epsilon}\right|_{\epsilon=0}$ [36].

[12] In above (40), a simplified expression for $\boldsymbol{\mathcal{E}}$ could have been obtained by neglecting the cross product contribution between the velocity $\boldsymbol{v}$ and the AC curl of the vector potential $\boldsymbol{A}$, that is, $\boldsymbol{\mathcal{E}} \approx -\left.\frac{\partial \boldsymbol{A}}{\partial t}\right|_{\boldsymbol{x}} + \boldsymbol{v} \times (\nabla \times \boldsymbol{A}^{DC})$.

3.3. DC and AC variational forms

For the establishment of the variational weak forms, we start by defining suitable variational functional spaces as follows

$$X_{\mathbb{R}^3} := \left\{ \boldsymbol{A} \in \boldsymbol{H}(\mathrm{curl}, \mathbb{R}^3) : \nabla \cdot \boldsymbol{A} = 0 \text{ in } \mathbb{R}^3,\ \boldsymbol{A} = O(|\boldsymbol{x}|^{-1}) \text{ as } |\boldsymbol{x}| \to \infty \right\}, \tag{41a}$$

$$Y(\boldsymbol{g}) := \left\{ \boldsymbol{u} \in (H^1(\Omega_c))^3 : \boldsymbol{u} = \boldsymbol{g} \text{ on } \partial\Omega_c^D \right\}, \tag{41b}$$

and consider $\boldsymbol{A}^{DC} \in X_{\mathbb{R}^3}$ as unknown (or trial function) and obtain the **DC weak form**

$$\delta W^{DC}(\boldsymbol{A}^{DC}; \delta\boldsymbol{A}^{DC}) = \int_{\mathbb{R}^3} \nabla \times \delta\boldsymbol{A}^{DC} \cdot \mu_0^{-1} \nabla \times \boldsymbol{A}^{DC} d\Omega - \int_{\Omega_{\boldsymbol{J}_f^{DC}}} \boldsymbol{J}_f^{DC} \cdot \delta\boldsymbol{A}^{DC} d\Omega = 0, \tag{42}$$

for all virtual fields (or weighting/test functions) $\delta\boldsymbol{A}^{DC} \in X_{\mathbb{R}^3}$, where $\Omega_{\boldsymbol{J}_f^{DC}} = \mathrm{supp}(\boldsymbol{J}_f^{DC})$ corresponds to the support of the source current $\boldsymbol{J}_f^{DC}$. Subsequently, to define the **$\boldsymbol{A}$-component of the AC weak form**, we consider $\boldsymbol{A}(t) \in X_{\mathbb{R}^3}$ and $\boldsymbol{u}(t) \in Y(\boldsymbol{u}_D)$ as unknowns (or trial functions) and obtain

$$\begin{aligned} \delta W_{\boldsymbol{A}}^{AC}(\boldsymbol{A}, \boldsymbol{u}; \delta\boldsymbol{A}) = & \int_{\Omega_c} \delta\boldsymbol{A} \cdot \gamma \left.\frac{\partial \boldsymbol{A}}{\partial t}\right|_{\boldsymbol{x}} d\Omega + \int_{\mathbb{R}^3} \nabla \times \delta\boldsymbol{A} \cdot \mu_0^{-1} \nabla \times \boldsymbol{A} d\Omega \\ & - \int_{\Omega_{\boldsymbol{J}_f^{AC}}} \boldsymbol{J}_f^{AC} \cdot \delta\boldsymbol{A} d\Omega - \int_{\Omega_c} \boldsymbol{J}_{\mathcal{L}}^{\star}(\boldsymbol{v}, \boldsymbol{A}^{DC}, \boldsymbol{A}) \cdot \delta\boldsymbol{A} d\Omega = 0, \end{aligned} \tag{43}$$

for all virtual fields (or weighting/test functions) $\delta\boldsymbol{A} \in X_{\mathbb{R}^3}$, where $\Omega_{\boldsymbol{J}^{AC}} = \mathrm{supp}(\boldsymbol{J}^{AC})$ correspond to the support of the source current. Similarly, to define the **$\boldsymbol{u}$-component of the AC weak form** and compute

$$\begin{aligned} \delta W_{\boldsymbol{u}}^{AC}(\boldsymbol{A}, \boldsymbol{u}; \delta\boldsymbol{u}) = & \int_{\Omega_c} \delta\boldsymbol{u} \cdot \rho \left.\frac{\partial^2 \boldsymbol{u}}{\partial t^2}\right|_{\boldsymbol{X}} d\Omega + \int_{\Omega_c} \boldsymbol{\epsilon}(\delta\boldsymbol{u}) : \boldsymbol{\sigma}_m(\boldsymbol{u}) d\Omega \\ & + \int_{\Omega_c} \boldsymbol{\epsilon}(\delta\boldsymbol{u}) : \boldsymbol{\tau}_{\infty}^{\star}(\boldsymbol{A}^{DC}, \boldsymbol{A}) d\Omega + \int_{\mathbb{R}^3 \setminus \Omega_c} \boldsymbol{\epsilon}(\delta\boldsymbol{u}) : \boldsymbol{\tau}_{\infty}^{\star}(\boldsymbol{A}^{DC}, \boldsymbol{A}) d\Omega = 0, \end{aligned} \tag{44}$$

for all virtual fields (or weighting/test functions) $\delta\boldsymbol{u} \in Y(\boldsymbol{0})$, where the dependence of tensor fields $\boldsymbol{\epsilon}$ and $\boldsymbol{\sigma}$ on $\boldsymbol{u}$ or $\delta\boldsymbol{u}$ has been explicitly stated. In above (43) and (44) and hereafter, upper index over the pair $\{\boldsymbol{\tau}_\infty, \boldsymbol{J}_{\mathcal{L}}\}$ is used to indistinctively refer to the nonlinear or linerarised versions.

4. Computational space-time methodology

Once the variational forms for both DC and AC subproblems have been defined, suitable space and time discretisation can be employed. This section starts presenting the *hp*-FEM approach preferred by the authors with their use fully justified in previous publications [13,14,16]. Subsequently, the spatial case of axisymmetric formulations of interest in this paper is then presented. The time integration approach is shown next along with a consistently derived frequency formulation for comparison purposes. The Section finishes with a brief description of the fixed-point acceleration approach to be used between solvers.

4.1. *hp*-FEM discretisation

The initially unbounded domain $\mathbb{R}^3$ is truncated at a finite distance from the conducting domain Ω_c to define a suitably reduced domain of interest Ω, where an appropriate boundary condition must be applied on $\partial\Omega$, thus replacing the far-field conditions. Specifically, the functional space $X_{\mathbb{R}^3}$ (41a) used to define trial and test functions is suitably replaced with

$$\tilde{X}_\Omega(\boldsymbol{g}) := \left\{ \boldsymbol{A} \in \boldsymbol{H}(\mathrm{curl}, \Omega) : \nabla \cdot \boldsymbol{A} = 0 \text{ in } \mathbb{R}^3, \boldsymbol{n}|_{\partial\Omega} \times \boldsymbol{A} = \boldsymbol{n}|_{\partial\Omega} \times \boldsymbol{g} \text{ on } \partial\Omega \right\}, \tag{45}$$

where $\boldsymbol{g} = \boldsymbol{A}^{\mathrm{exact}}$ in the case of an available closed-form solution and $\boldsymbol{g} = \boldsymbol{0}$ if the far field decay solution is to be approximated. The truncated domain Ω is then tessellated, that is, a non-overlapping unstructured partitioning of the domain is introduced where N_e is the total number of finite elements in the discretisation and $\Omega^{(e)}$ denotes a single element. To define the DC semi-discrete system of the weak form statement (42), we seek trial functions $\boldsymbol{A}_{hq}^{DC} \in \tilde{X}_\Omega(\boldsymbol{0}) \cap X_{hq}$ and use test/weighting functions $\delta\boldsymbol{A}_{hq}^{DC} \in \tilde{X}_\Omega(\boldsymbol{0}) \cap X_{hq}$, where X_{hq} represents the space of hierarchical $\boldsymbol{H}(\mathrm{curl}, \Omega)$ basis functions and the subindex $(\cdot)_{hq}$ is used to emphasise the Finite Element character of the approximation. Thus

$$\boldsymbol{A}_{hq}^{DC} = \sum_{a=1}^{P_{global}^{DC}} \boldsymbol{N}_A^a A^{DC,a} = \mathbf{N}_A \mathbf{A}^{DC}; \tag{46a}$$

$$\delta\boldsymbol{A}_{hq}^{DC} = \sum_{a=1}^{P_{global}^{DC}} \boldsymbol{N}_A^a \delta A^{DC,a} = \mathbf{N}_A \delta\mathbf{A}^{DC}, \tag{46b}$$

where $\boldsymbol{N}_A^a$ represents the $\boldsymbol{H}(\mathrm{curl})$ vector shape function corresponding to the Degree of Freedom (DoF) a, with P_{global}^{DC} denoting the total number of DoFs considered, and $\{A^{DC,a}, \delta A^{DC,a}\}$ the approximation coefficients at DoF a of the trial and test functions, respectively. Alternatively, in standard matrix notation, N_A symbolises the matrix of $\boldsymbol{H}$(curl) vector shape functions and A^{DC} and $\delta\mathsf{A}^{DC}$ the vectorised vector of unknowns. As a result, the curl of the trial and test functions is computed as

$$\nabla \times \boldsymbol{A}_{hq}^{DC} = \sum_{a=1}^{P_{global}^{DC}} \boldsymbol{B}_A^a A^{DC,a} = \mathsf{B}_A \mathsf{A}^{DC}; \tag{47a}$$

$$\nabla \times \delta\boldsymbol{A}_{hq}^{DC} = \sum_{a=1}^{P_{global}^{DC}} \boldsymbol{B}_A^a \delta A^{DC,a} = \mathsf{B}_A \delta\mathsf{A}^{DC}, \tag{47b}$$

where B_A is the matrix containing the curl of the $\boldsymbol{H}$(curl) vector shape functions $\boldsymbol{B}_A^a$. Therefore, the semi-discrete DC weak form yields: Find $\boldsymbol{A}_{hq}^{DC} \in \tilde{X}_\Omega(\mathbf{0}) \cap X_{hq}$ such that

$$\delta W^{DC}(\boldsymbol{A}_{hq}^{DC}; \delta\boldsymbol{A}_{hq}^{DC}) = \delta\mathsf{A}^{DC^T}(\mathsf{K}_{AA}\mathsf{A}^{DC} - \mathsf{J}_f^{DC}) = 0, \tag{48}$$

for all $\delta\boldsymbol{A}_{hq}^{DC} \in \tilde{X}_\Omega(\mathbf{0}) \cap X_{hq}$, where

$$\mathsf{K}_{AA} = \int_\Omega \mathsf{B}_A^T \mu_0^{-1} \mathsf{B}_A \, d\Omega; \tag{49a}$$

$$\mathsf{J}_f^{DC} = \int_{\Omega_{\boldsymbol{J}_f^{DC}}} \mathsf{N}_A^T \boldsymbol{J}_f^{DC} \, d\Omega. \tag{49b}$$

To define the AC semi-discrete weak form statements (43)–(44), we seek trial functions $\boldsymbol{A}_{hq} \in \tilde{X}_\Omega(\boldsymbol{g}) \cap X_{hq}$ and $\boldsymbol{u}_{hp} \in Y(\boldsymbol{u}^D) \cap W_{hp}$, and use test/weighting functions $\delta\boldsymbol{A}_{hq} \in \tilde{X}_\Omega(\mathbf{0}) \cap X_{hq}$ and $\delta\boldsymbol{u}_{hp} \in Y(\mathbf{0}) \cap W_{hp}$, where W_{hq} represents the space of hierarchical $H^1(\Omega)$ basis functions. Thus,

$$\boldsymbol{A}_{hq} = \sum_{g=1}^{P_{global}} \boldsymbol{N}_A^g A^g = \mathsf{N}_A \mathsf{A}; \tag{50a}$$

$$\delta\boldsymbol{A}_{hq} = \sum_{g=1}^{P_{global}} \boldsymbol{N}_A^g \delta A^g = \mathsf{N}_A \delta\mathsf{A}, \tag{50b}$$

and

$$\boldsymbol{u}_{hp} = \sum_{g=1}^{Q_{global}} N_u^g \boldsymbol{u}^g = \mathsf{N}_u \mathsf{u}; \tag{51a}$$

$$\delta\boldsymbol{u}_{hp} = \sum_{g=1}^{Q_{global}} N_u^g \delta\boldsymbol{u}^g = \mathsf{N}_u \delta\mathsf{u}, \tag{51b}$$

where $\boldsymbol{N}_A^g$ represents the $\boldsymbol{H}$(curl) vector shape function corresponding to the Degree of Freedom (DoF) g, with P_{global} denoting the total number of DoFs considered, and $\{A^g, \delta A^g\}$ the approximation coefficients at DoF g of the trial and test functions, respectively. Similarly, N_u^g represents the (scalar) H^1 shape function corresponding to the Degree of Freedom (DoF) g, with Q_{global} denoting the total number of DoFs considered, and $\{\boldsymbol{u}^g, \delta\boldsymbol{u}^g\}$ the approximation vector coefficients at DoF g of the trial and test functions, respectively. Alternatively, in standard matrix notation, N_u symbolises the matrix of H^1 shape functions and u and $\delta\mathsf{u}$ the vectorised vector of unknowns, with N_A, A and $\delta\mathsf{A}$ with a similar definition to that in (46). The strain of the trial and test displacement functions (in vectorised Voigt notation) is computed as

$$\underline{\epsilon}(\boldsymbol{u}_{hp}) = \sum_{a=1}^{Q_{global}} \boldsymbol{B}_u^a \boldsymbol{u}^a = \mathsf{B}_u \mathsf{u}; \tag{52a}$$

$$\underline{\epsilon}(\delta\boldsymbol{u}_{hp}) = \sum_{a=1}^{Q_{global}} \boldsymbol{B}_u^a \delta\boldsymbol{u}^a = \mathsf{B}_u \delta\mathsf{u}, \tag{52b}$$

where the underline is used to denote Voigt notation and B_u is the matrix containing the symmetric gradient of the H^1 shape functions $\boldsymbol{B}_u^a$. Thus, the semi-discrete AC weak form yields: Find $(\boldsymbol{A}_{hq}(t), \boldsymbol{u}_{hp}(t)) \in \tilde{X}_\Omega(\mathbf{0}) \cap X_{hq} \times Y(\boldsymbol{u}_D) \cap W_{hp}$ fulfilling the initial conditions

$$\boldsymbol{A}_{hq}|_{t=0} = \mathbf{0}; \tag{53a}$$

$$\boldsymbol{u}_{hp}|_{t=0} = \mathbf{0}; \tag{53b}$$

$$\left.\frac{\partial \boldsymbol{u}_{hp}}{\partial t}\right|_{\boldsymbol{X}|_{t=0}} = \mathbf{0}, \tag{53c}$$

such that

$$\delta W_{\boldsymbol{A}}^{AC}(\boldsymbol{A}_{hq}, \boldsymbol{u}_{hp}; \delta\boldsymbol{A}_{hq}) = \delta\mathsf{A}^T\left(\mathsf{M}_{AA}^{\gamma}\frac{d\mathsf{A}}{dt} + \mathsf{K}_{AA}\mathsf{A} - \mathsf{J}_{\mathcal{L}}^{\star} - \mathsf{J}_f^{AC}\right) = 0, \tag{54a}$$

$$\delta W^{AC}_{\boldsymbol{u}}(\boldsymbol{A}_{hq},\boldsymbol{u}_{hp};\delta\boldsymbol{u}_{hp}) = \delta\mathbf{u}^T\left(\mathbf{M}^{\rho}_{uu}\frac{d^2\mathbf{u}}{dt^2}+\mathbf{C}_{uu}\frac{d\mathbf{u}}{dt}+\mathbf{K}_{uu}\mathbf{u}-\mathbf{F}^{\star}_{\mathcal{L}}\right)=0, \tag{54b}$$

for all $(\delta\boldsymbol{A}_{hq},\delta\boldsymbol{u}_{hp})\in\tilde{X}_{\Omega}(\mathbf{0})\cap X_{hq}\times Y(\mathbf{0})\cap W_{hp}$, where

$$\mathbf{M}^{\gamma}_{AA}=\int_{\Omega_c}\mathbf{N}^T_A\gamma\mathbf{N}_A\,d\Omega_c; \tag{55a}$$

$$\mathbf{K}_{uu}=\int_{\Omega_c}\mathbf{B}^T_u\boldsymbol{D}\mathbf{B}_u\,d\Omega_c; \tag{55b}$$

$$\mathbf{M}^{\rho}_{uu}=\int_{\Omega_c}\mathbf{N}^T_u\rho\mathbf{N}_u\,d\Omega_c, \tag{55c}$$

where $\mathbf{J}^{AC}_f$ is defined as in (49b) replacing $\bullet^{DC}$ with $\bullet^{AC}$, $\boldsymbol{D}$ in (55b) is the standard constitutive-like vectorised second order tensor and

$$\mathbf{J}^{\star}_{\mathcal{L}}=\int_{\Omega_c}\mathbf{N}^T_A\boldsymbol{J}^{\star}_{\mathcal{L}}(\boldsymbol{v}_{hp},\boldsymbol{A}^{DC}_{hq},\boldsymbol{A}_{hq})\,d\Omega_c; \tag{56a}$$

$$\mathbf{F}^{\star}_{\mathcal{L}}=\int_{\Omega_c}\mathbf{B}^T_u\underline{\boldsymbol{\tau}}^{\star}_{\infty}(\boldsymbol{A}^{DC}_{hq},\boldsymbol{A}_{hq})\,d\Omega_c, \tag{56b}$$

denote the coupled semi-discrete Lorentz's and Maxwell force vectors, respectively. In above equation (56b), the (underlined) Voigt notation has been used for the Maxwell stress tensor and the upper symbol $(\bullet)^{\star}$ has been used to indicate either the nonlinear or linearised versions. Note that a Rayleigh-type damping matrix $\mathbf{C}_{uu}$ has been added into (54b) to permit the consideration of explicit mechanical damping (as in [13,14]). The semi-discrete solution process is summarised and displayed in Algorithm 1. Note that the coupling between (58) and (59) is explicitly observed which will require of an iterative-type solution process.

Algorithm 1 Semi-discrete solution procedure.

```
procedure DC PROBLEM($\boldsymbol{J}^{DC}_f$)                                        ▷ DC problem
    Input data: main coil current $\boldsymbol{J}^{DC}_f$
    Construct DC semi-discrete current vector $\mathbf{J}^{DC}_f$ using (49b)
    Compute solution of DC vector potential $\mathbf{A}^{DC}$

        $\mathbf{K}_{AA}\mathbf{A}^{DC}=\mathbf{J}^{DC}_f.$                                        (57)

end procedure
procedure AC PROBLEM($\boldsymbol{J}^{AC}_f,\boldsymbol{u}^D$)                                    ▷ AC problem
    Input data: gradient coils current $\boldsymbol{J}^{AC}_f$, floor-borne vibrations $\boldsymbol{u}^D$ and initial conditions $\{\boldsymbol{A}|_{t=0},\boldsymbol{u}|_{t=0},\left.\frac{d\boldsymbol{u}}{dt}\right|_{t=0}\}$
    while $t<T$ do
        Compute Lorentz's current $\boldsymbol{J}^{\star}_{\mathcal{L}}$ using (38)
        Construct AC semi-discrete current vector $\mathbf{J}^{AC}_f$ and $\mathbf{J}^{\star}_{\mathcal{L}}$ using $AC$-adapted (49b) and (56a)
        Compute solution of AC vector potential $\mathbf{A}$

            $\mathbf{M}^{\gamma}_{AA}\frac{d\mathbf{A}}{dt}+\mathbf{K}_{AA}\mathbf{A}=\mathbf{J}^{AC}_f+\mathbf{J}^{\star}_{\mathcal{L}}\left(\frac{d\mathbf{U}}{dt},\mathbf{A}^{DC},\mathbf{A},\right).$        (58)

        Construct equivalent force vector $\mathbf{F}^{\star}_{\mathcal{L}}$ using (56b)
        Construct floor-borne vibration vector $\mathbf{u}|_{\partial\Omega^D_c}=\mathbf{u}_D$
        Compute solution of displacement vector $\mathbf{u}$

            $\mathbf{M}^{\rho}_{uu}\frac{d^2\mathbf{u}}{dt^2}+\mathbf{C}_{uu}\frac{d\mathbf{u}}{dt}+\mathbf{K}_{uu}\mathbf{u}=\mathbf{F}^{\star}_{\mathcal{L}}\left(\mathbf{A}^{DC},\mathbf{A},\right).$        (59)

    end while
end procedure
```

4.2. Axisymmetric implementation

An axisymmetric formulation $\{r,\phi,z\}$ with cylindrical basis $\{e_r,e_\phi,e_z\}$ is assumed and the problem is formulated in the meridian two dimensional truncated domain Ω_m with embedded conducting region $\Omega_{m,c}$. The applied current fields are represented as $\boldsymbol{J}^{DC}=J^{DC}_{\phi}(r,z)e_{\phi}$ and $\boldsymbol{J}^{AC}(t)=J^{AC}_{\phi}(r,z,t)e_{\phi}$ and thus the solution fields become

$$\boldsymbol{A}=A_{\phi}(r,z)\boldsymbol{e}_{\boldsymbol{\phi}}; \tag{60a}$$

$$A_\phi(r,z) = r\hat{A}_\phi(r,z); \tag{60b}$$

$$\boldsymbol{u} = u_r(r,z)\boldsymbol{e}_r + u_z(r,z)\boldsymbol{e}_z; \tag{60c}$$

$$u_r(r,z) = r\hat{u}_r(r,z), \tag{60d}$$

where the r-scaling in $A_\phi(r,z)$ is introduced to avoid having to solve fields in weighted spaces and to resolve the $1/r$ singularities associated with $r \to 0$ [15], from which the curl of the vector potential and the symmetric gradient of the displacement field arise as

$$\nabla \times \boldsymbol{A} = \frac{1}{r}\tilde{\nabla}(r^2\hat{A}_\phi(r,z)) \times \boldsymbol{e}_\phi; \tag{61a}$$

$$\tilde{\nabla}_m = \frac{\partial}{\partial r}\boldsymbol{e}_r + \frac{\partial}{\partial z}\boldsymbol{e}_z, \tag{61b}$$

where $\tilde{\nabla}_m$ denotes the gradient operator constraint to the meridian plane, along with

$$\begin{aligned}\epsilon(\boldsymbol{u}) = &\left(\hat{u}_r(r,z) + r\frac{\partial \hat{u}_r(r,z)}{\partial r}\right)\boldsymbol{e}_r \otimes \boldsymbol{e}_r + \hat{u}_r(r,z)\boldsymbol{e}_\phi \otimes \boldsymbol{e}_\phi + \frac{\partial u_z(r,z)}{\partial z}\boldsymbol{e}_z \otimes \boldsymbol{e}_z \\ &+ \frac{1}{2}\left(r\frac{\partial \hat{u}_r(r,z)}{\partial z} + \frac{\partial u_z(r,z)}{\partial r}\right)(\boldsymbol{e}_r \otimes \boldsymbol{e}_z + \boldsymbol{e}_z \otimes \boldsymbol{e}_r).\end{aligned} \tag{62}$$

With above formulae (60)–(62) in hand, above semi-discrete set of (57)–(59) can be straightforwardly computed by simply replacing $\int_\Omega(\bullet)d\Omega$ with $2\pi\int_{\Omega_m}(\bullet)rd\Omega_m$ and $\int_{\Omega_c}(\bullet)d\Omega$ with $2\pi\int_{\Omega_{m,c}}(\bullet)rd\Omega_m$, where the stress tensors $\boldsymbol{\sigma}_m$ and $\boldsymbol{\tau}^\star_\infty$ can be obtained and (Voigt) vectorised taking advantage of the formulae (61)–(62). Note that, in this case, the vectors of unknowns $\mathbf{A}$ is defined as $\mathbf{A} = [\hat{A}^1_\phi \dots \hat{A}^{P_{global}}_\phi]^T$ with analogous expansions for $\mathbf{A}^{DC}$, $\delta\mathbf{A}$ and $\delta\mathbf{A}^{DC}$.

4.3. Time based formulation

For the time stepping solution of the AC transient systems of ordinary differential equations depicted in (58) and (59), appropriate time integration schemes can be used. A **modified backward Euler** scheme for (58) and a **mid-point** scheme for (59) are preferred as the simplest possible (unconditionally stable) implicit-type second order methods. Note that in the absence of acceleration type terms, the mid-point scheme degenerates into the modified backward Euler, which can also be seen as an implicit second order Runge-Kutta method. To start with, consider a time stepping scheme within the solution interval $[0,T]$, with $t_{n+1} = t_n + \Delta t$, with $n = 0,1\dots N-1$ such that $t_N = T$. Furthermore, we introduce discrete vectors $\mathbf{v} := \frac{d\mathbf{u}}{dt}$, $\mathbf{a} := \frac{d^2\mathbf{u}}{dt^2}$ and $\mathbf{Y} := \frac{d\mathbf{A}}{dt}$ and re-write (58) and (59) in terms of residuals

$$\mathbf{R}_A(\mathbf{Y}_{n+1/2}, \mathbf{a}_{n+1/2}) = \mathbf{M}^\gamma_{AA}\mathbf{Y}_{n+1/2} + \mathbf{K}_{AA}\mathbf{A}_{n+1/2} - \mathbf{J}^{AC}_f\Big|_{n+1/2} - \mathbf{J}^\star_{\mathcal{L}}(\mathbf{v}_{n+1/2}, \mathbf{A}^{DC}, \mathbf{A}_{n+1/2}) = \mathbf{0}, \tag{63a}$$

$$\mathbf{R}_u(\mathbf{Y}_{n+1/2}, \mathbf{a}_{n+1/2}) = \mathbf{M}^\rho_{uu}\mathbf{a}_{n+1/2} + \mathbf{C}_{uu}\mathbf{v}_{n+1/2} + \mathbf{K}_{uu}\mathbf{u}_{n+1/2} - \mathbf{F}^\star_{\mathcal{L}}(\mathbf{A}^{DC}, \mathbf{A}_{n+1/2}) = \mathbf{0}, \tag{63b}$$

where

$$\mathbf{A}_{n+1} = \mathbf{A}_n + \Delta t\mathbf{Y}_{n+1/2}; \tag{64a}$$

$$\mathbf{v}_{n+1} = \mathbf{v}_n + \Delta t\mathbf{a}_{n+1/2}; \tag{64b}$$

$$\mathbf{u}_{n+1} = \mathbf{u}_n + \Delta t\mathbf{v}_{n+1/2}, \tag{64c}$$

with $(\bullet)_{n+1/2} = 1/2((\bullet)_n + (\bullet)_{n+1})$ for $(\bullet) = \{\mathbf{A}, \mathbf{u}, \mathbf{v}\}$. Coupling of (63a) and (63b) takes place via the right hand side terms $\mathbf{J}^\star_{\mathcal{L}}(\mathbf{v}_{n+1/2}, \mathbf{A}^{DC}, \mathbf{A}_{n+1/2})$ and $\mathbf{F}^\star_{\mathcal{L}}(\mathbf{A}^{DC}, \mathbf{A}_{n+1/2})$. Numerically, a fixed point type of procedure can be used to drive a k-iteration process for every time step t_n within a given tolerance criterion TOL. For instance, considering a typical **predictor-corrector** procedure, the corrector step yields

$$(\mathbf{M}^\gamma_{AA} + \frac{\Delta t}{2}\mathbf{K}_{AA})\Delta\mathbf{Y}_{n+1/2} = -\mathbf{R}_A(\mathbf{Y}^{(k)}_{n+1/2}, \mathbf{a}^{(k+1)}_{n+1/2}), \tag{65a}$$

$$(\mathbf{M}^\rho_{uu} + \frac{\Delta t}{2}\mathbf{C}_{uu} + \frac{\Delta t^2}{4}\mathbf{K}_{uu})\Delta\mathbf{a}_{n+1/2} = -\mathbf{R}_u(\mathbf{Y}^{(k+1)}_{n+1/2}, \mathbf{a}^{(k+1)}_{n+1/2}), \tag{65b}$$

with the corrector update

$$\mathbf{Y}^{(k+1)}_{n+1/2} = \mathbf{Y}^{(k)}_{n+1/2} + \Delta\mathbf{Y}_{n+1/2}, \tag{66a}$$

$$\mathbf{a}^{(k+1)}_{n+1/2} = \mathbf{a}^{(k)}_{n+1/2} + \Delta\mathbf{a}_{n+1/2}. \tag{66b}$$

An algorithmic description of this process is described in Algorithm 2.

4.4. Frequency based formulation

The linearised transient weak statements (54a) and (54b) (i.e. for $(\bullet)^\star = (\bullet)^{\text{lin}}$) can be further modified by particularising to the case of wave-type solution vectors. With that in mind, we can consider a generic time dependent semi-discrete weak form statement as: Find $\mathbf{V}(t) \in \mathbb{R}^n$ such that

$$\delta W(\mathbf{V}(t); \delta\mathbf{V}(t)) := \delta\mathbf{V}^T(t)(\mathbf{T}(\mathbf{V}(t)) - \mathbf{F}(t)) = 0, \tag{67}$$

Algorithm 2 Fixed-point iteration procedure.

```
Initial guess for $\Delta \mathbf{a}_{n+1/2}$
while Residual($\mathbf{Y}_{n+1/2}, \mathbf{a}_{n+1/2}$) $< TOL$ do
    Corrector for displacements: use (66b) to obtain $\mathbf{a}^{(k+1)}_{n+1/2}$ and then other kinematic outputs using (64b),(64c)
    Update magnetic potential rate: use (65a) to obtain $\Delta \mathbf{Y}_{n+1/2}$
    Corrector for vector potential: use (66a) to obtain $\mathbf{A}^{(k+1)}_{n+1/2}$ and other outputs (64a)
    Update acceleration: use (65b) to obtain $\Delta \mathbf{a}_{n+1/2}$
end while
```

for all $\delta\mathbf{V}(t) \in \mathbb{R}^n$, with n a generic dimension, $\mathbf{T} : \mathbb{R}^n \to \mathbb{R}^n$ a (real) vector linear operator on $\mathbf{V}(t)$ and $\mathbf{F}(t)$ a time-dependent vector. Specifically, generic vector $\mathbf{V}(t)$ can symbolise $\mathbf{A}(t)$ or $\mathbf{u}(t)$ (and vector $\delta\mathbf{V}(t)$ its counterparts $\delta\mathbf{A}(t)$ or $\delta\mathbf{u}(t)$). Thus, a wave-type solution vector of natural frequency ω can be written as

$$\mathbf{V}(t) = \mathrm{Re}(\mathcal{V} e^{\mathrm{i}\omega t}); \qquad \mathbf{V}(t) \in \mathbb{R}^n; \qquad \mathcal{V} \in \mathbb{C}^n, \tag{68}$$

with $\mathcal{V}$ representing the complex phasor vector corresponding to the real transient vector $\mathbf{V}(t)$, with $\mathrm{i} = \sqrt{-1}$ the imaginary number. Note that hereafter calligraphic fonts will be solely used to denote complex phasors magnitudes, unless otherwise stated, and should not confused with physical magnitudes defined in the Updated Lagrangian description (as used in Section 2). Similarly, is further assumed a similar wave-type expression for the vectors $\delta\mathbf{V}(t)$ and $\mathbf{F}(t)$, as

$$\delta\mathbf{V}(t) = \mathrm{Re}(\delta\mathcal{V} e^{\mathrm{i}\omega t}); \qquad \delta\mathbf{V}(t) \in \mathbb{R}^n; \qquad \delta\mathcal{V} \in \mathbb{C}^n, \tag{69}$$

and

$$\mathbf{F}(t) = \mathrm{Re}(\mathcal{F} e^{\mathrm{i}\omega t}); \qquad \mathbf{F}(t) \in \mathbb{R}^n; \qquad \mathcal{F} \in \mathbb{C}^n, \tag{70}$$

with $\delta\mathcal{V}$ and $\mathcal{F}$ representing the complex phasor vectors corresponding to the real transient vectors $\delta\mathbf{V}(t)$ and $\mathbf{F}(t)$, respectively. Thus, the time average (i.e. steady-state contribution) denoted by the symbol $\overline{\bullet}$ of above (67) can be obtained as

$$\overline{\delta W(\mathbf{V}(t); \delta\mathbf{V}(t))} = \frac{1}{2}\mathrm{Re}(\delta\mathcal{V}^*(\mathcal{T}(\mathcal{V}) - \mathcal{F})) = 0, \tag{71}$$

where the symbol $(\cdot)^*$ denotes the Hermitian transpose. As a result, an alternative semi-discrete complex weak form statement can be summarised as: Find $\mathcal{V} \in \mathbb{C}^n$ such that

$$\delta\mathcal{W}(\mathcal{V}; \delta\mathcal{V}) := \mathrm{Re}(\delta\mathcal{V}^*(\mathcal{T}(\mathcal{V}) - \mathcal{F})) = 0, \tag{72}$$

for any $\delta\mathcal{V} \in \mathbb{C}^n$. Note that the calligraphic symbol $\delta\mathcal{W}$ has been introduced to clearly differentiate the spatial semi-discrete complex steady-state version (72) from its real transient counterpart (67) (defined via δW). Referring back to (54a) and (54b), it is now possible to introduce wave-type solutions of the form

$$\mathbf{A}(t) = \mathrm{Re}(\mathcal{A} e^{\mathrm{i}\omega t}); \tag{73a}$$

$$\mathbf{u}(t) = \mathrm{Re}(\mathcal{U} e^{\mathrm{i}\omega t}), \tag{73b}$$

with analogous virtual counterparts

$$\delta\mathbf{A}(t) = \mathrm{Re}(\delta\mathcal{A} e^{\mathrm{i}\omega t}); \tag{74a}$$

$$\delta\mathbf{u}(t) = \mathrm{Re}(\delta\mathcal{U} e^{\mathrm{i}\omega t}), \tag{74b}$$

which after substitution into (54a)–(54b) and use of (71)–(72), permits a frequency sweep over $\omega = \omega_1, \omega_2, \ldots, \omega_N$ seeking to obtain complex phasors $\{\mathcal{A}, \mathcal{U}\}$ satisfying

$$\mathcal{R}_{\mathcal{A}}(\mathcal{A}, \mathcal{U}) = (\mathrm{i}\omega \mathbf{M}^{\gamma}_{AA} + \mathbf{K}_{AA})\mathcal{A} - \mathcal{J}^{AC}_{f} - \mathcal{J}^{\mathrm{lin}}_{\mathcal{L}}(\mathrm{i}\omega\mathcal{U}, \mathbf{A}^{DC}, \mathcal{A}) = \mathbf{0}, \tag{75a}$$

$$\mathcal{R}_{\mathcal{U}}(\mathcal{A}, \mathcal{U}) = (-\omega^2 \mathbf{M}^{\rho}_{uu} + \mathrm{i}\omega\mathbf{C}_{uu} + \mathbf{K}_{uu})\mathcal{U} - \mathcal{F}^{\mathrm{lin}}_{\mathcal{L}}(\mathbf{A}^{DC}, \mathcal{A}) = \mathbf{0}, \tag{75b}$$

where $\{\mathcal{J}^{AC}_{f}, \mathcal{J}^{\mathrm{lin}}_{\mathcal{L}}, \mathcal{F}^{\mathrm{lin}}_{\mathcal{L}}\}$ are the frequency counterparts of $\{\mathbf{J}^{AC}_{f}, \mathbf{J}^{\mathrm{lin}}_{\mathcal{L}}, \mathbf{F}^{\mathrm{lin}}_{\mathcal{L}}\}$. Note that a Rayleigh-type damping term $\mathrm{i}\omega\mathbf{C}_{uu}$ has been added into (75b) to permit the consideration of explicit mechanical damping. Moreover, the coupling between above (75a) and (75b) is explicitly observed via the terms $\mathcal{J}^{\mathrm{lin}}_{\mathcal{L}}(\mathrm{i}\omega\mathcal{U}, \mathbf{A}^{DC}, \mathcal{A})$ and $\mathcal{F}^{\mathrm{lin}}_{\mathcal{L}}(\mathbf{A}^{DC}, \mathcal{A})$. A fixed point type of procedure can be used to drive a k-iteration process for every frequency within a given tolerance criterion TOL, that is,

$$(\mathrm{i}\omega \mathbf{M}^{\gamma}_{AA} + \mathbf{K}_{AA})\Delta\mathcal{A} = -\mathcal{R}_{\mathcal{A}}(\mathcal{A}^{(k)}, \mathcal{U}^{(k+1)}), \tag{76a}$$

$$(-\omega^2 \mathbf{M}^{\rho}_{uu} + \mathrm{i}\omega\mathbf{C}_{uu} + \mathbf{K}_{uu})\Delta\mathcal{U} = -\mathcal{R}_{\mathcal{U}}(\mathcal{A}^{(k+1)}, \mathcal{U}^{(k+1)}), \tag{76b}$$

with

$$\mathcal{A}^{(k+1)} = \mathcal{A}^{(k)} + \Delta\mathcal{A}; \tag{77a}$$

$$\mathcal{U}^{(k+1)} = \mathcal{U}^{(k)} + \Delta\mathcal{U}, \tag{77b}$$

where convergence is controlled by a suitable norm Residual($\mathcal{U}^{(k+1)}, \mathcal{A}^{(k+1)}$), resulting into an algorithm breakdown analogous to that previously described in Algorithm 2, albeit adapted to the frequency case.

4.5. *Acceleration technique via Aitken Δ^2 method*

To improve the convergence rate of the fixed point iteration method used in this work, an acceleration technique based on the Aitken Δ^2 method is applied. This method, originally developed for scalar sequences, has been extended to the vector case through a general residual-based framework [29,43]. In general, the convergence acceleration is achieved by using information from previous iterations to construct an improved estimate of the solution. For the numerical examples considered in this paper, the Irons and Tuck [44], Lemaréchal [45], and Wynn [46] acceleration techniques are employed. Specifically, given three successive $(k+1)$ fixed point iterations of a generic vector sequence $\left\{\mathbf{X}_{[0]}^{(k+1)}, \mathbf{X}_{[1]}^{(k+1)}, \mathbf{X}_{[2]}^{(k+1)}\right\}$ and after introduction of the so-called ath first-order and second-order difference operators given by

$$\Delta\mathbf{X}_{[a]}^{(k+1)} = \mathbf{X}_{[a+1]}^{(k+1)} - \mathbf{X}_{[a]}^{(k+1)}; \tag{78a}$$

$$\Delta^2\mathbf{X}_{[a]}^{(k+1)} = \Delta\mathbf{X}_{[a+1]}^{(k+1)} - \Delta\mathbf{X}_{[a]}^{(k+1)}, \tag{78b}$$

the Irons and Tuck [44] acceleration update is defined as

$$\mathbf{X}^{(k+1)} = \mathbf{X}_{[2]}^{(k+1)} - \frac{\langle \Delta\mathbf{X}_{[1]}^{(k+1)}, \Delta^2\mathbf{X}_{[0]}^{(k+1)} \rangle}{\langle \Delta^2\mathbf{X}_{[0]}^{k}, \Delta^2\mathbf{X}_{[0]}^{k} \rangle} \Delta\mathbf{X}_{[1]}^{k}, \tag{79}$$

the Lemaréchal [45] acceleration update is defined as

$$\mathbf{X}^{(k+1)} = \mathbf{X}_{[0]}^{(k+1)} - \frac{\langle \Delta\mathbf{X}_{[0]}^{(k+1)}, \Delta^2\mathbf{X}_{[0]}^{(k+1)} \rangle}{\langle \Delta^2\mathbf{X}_{[0]}^{(k+1)}, \Delta^2\mathbf{X}_{[0]}^{(k+1)} \rangle} \Delta\mathbf{X}_{[0]}^{k}, \tag{80}$$

and the Wynn [46] acceleration update is defined as

$$\mathbf{X}^{(k+1)} = \mathbf{X}_{[1]}^{(k+1)} + \frac{\langle \Delta\mathbf{X}_{[0]}^{(k+1)}, \Delta\mathbf{X}_{[0]}^{(k+1)} \rangle \Delta\mathbf{X}_{[1]}^{(k+1)} - \langle \Delta\mathbf{X}_{[1]}^{(k+1)}, \Delta\mathbf{X}_{[1]}^{(k+1)} \rangle \Delta\mathbf{X}_{[0]}^{(k+1)}}{\langle \Delta^2\mathbf{X}_{[0]}^{(k+1)}, \Delta^2\mathbf{X}_{[0]}^{(k+1)} \rangle}, \tag{81}$$

where $\langle , \rangle$ denotes the vector inner product. These three acceleration techniques are implemented as part of an iterative process that uses only fixed point evaluations and does not require modification of the underlying solvers. The complete accelerated fixed point iteration procedure for the frequency-based approach is presented in Algorithm 3. A similar algorithm is used for the time-based approach.

Algorithm 3 Aitken Δ^2 accelerated fixed point iteration solution procedure for time harmonic approach.

```
Input data: gradient coils current $\boldsymbol{\mathcal{J}}_f^{AC}$ and floor-borne vibrations $\boldsymbol{\mathcal{U}}^D$
while $t < T$ do
    while $|\boldsymbol{\mathcal{U}}^{(k+1)} - \boldsymbol{\mathcal{U}}^{(k)}|$ and $|\boldsymbol{\mathcal{A}}^{(k+1)} - \boldsymbol{\mathcal{A}}^{(k)}|$ >TOL do
        for $n_{\text{Iter}}$ do
            Set $\boldsymbol{\mathcal{A}}_{[0]}^{(k+1)} = \boldsymbol{\mathcal{A}}^{(k)}$ and $\boldsymbol{\mathcal{U}}_{[0]}^{(k+1)} = \boldsymbol{\mathcal{U}}^{(k)}$
            Compute $\boldsymbol{\mathcal{J}}_{\mathcal{L}}^{\text{lin}}\left(\boldsymbol{\mathcal{U}}_{[0]}^{(k+1)}, \boldsymbol{B}^{DC}\right)$ and $\boldsymbol{\tau}_{\infty}^{\text{lin}}\left(\boldsymbol{\mathcal{A}}_{[0]}^{(k+1)}, \boldsymbol{B}^{DC}\right)$
            Solve (76) and (77) to obtain $\boldsymbol{\mathcal{A}}_{[1]}^{(k+1)}$ and $\boldsymbol{\mathcal{U}}_{[1]}^{(k+1)}$.
            Compute $\boldsymbol{\mathcal{J}}_{\mathcal{L}}^{\text{lin}}\left(\boldsymbol{\mathcal{U}}_{[1]}^{(k+1)}, \boldsymbol{B}^{DC}\right)$ and $\boldsymbol{\tau}_{\infty}^{\text{lin}}\left(\boldsymbol{\mathcal{A}}_{[1]}^{(k+1)}, \boldsymbol{B}^{DC}\right)$
            Solve (76) and (77) to obtain $\boldsymbol{\mathcal{A}}_{[2]}^{(k+1)}$ and $\boldsymbol{\mathcal{U}}_{[2]}^{(k+1)}$.
            Compute accelerated solution for $\boldsymbol{\mathcal{A}}^{(k+1)}(\boldsymbol{\mathcal{A}}_{[0]}^{(k+1)}, \boldsymbol{\mathcal{A}}_{[1]}^{(k+1)}, \boldsymbol{\mathcal{A}}_{[2]}^{(k+1)})$ and $\boldsymbol{\mathcal{U}}^{(k+1)}(\boldsymbol{\mathcal{U}}_{[0]}^{(k+1)}, \boldsymbol{\mathcal{U}}_{[1]}^{(k+1)}, \boldsymbol{\mathcal{U}}_{[2]}^{(k+1)})$ using Aitken $\Delta^2$ approach using either of formulae (79)–(81).
        end for
    end while
end while
```

5. Numerical examples: benchmarking

In this section, the benchmarking of the Python code developed using the open-source finite element package NGSolve [28] is discussed and the numerical solutions from the solver are compared to analytical solutions for academic problems of interest. hp-convergence and Δt-convergence studies are conducted to ensure spatial and temporal convergence in the solution. Furthermore, the motivation for the use of local mesh refinement using specialised elements is discussed and studies presented. For the examples presented, the curved geometry is described by second order rational splines in NGSolve, which give an exact representation of ellipses (and hence the cases where curved geometry is employed in this work). These are incorporated using a blending function approach as commonly used in *hp*-FEM [21,32,33,47]. To ensure that the numerical solution has converged and is accurate, an error measure

Table 1
Table of physical parameters for the time harmonic conducting sphere problem of interest.

Parameter	Units	Value
Sphere relative permeability – μ_r	–	2
Background electrical conductivity – γ_0	S m^{-1}	0
Sphere electrical conductivity – γ	S m^{-1}	10^7

for the eddy current problem of interest must be defined against a closed form solution. The norms of the L^2 and H^1 error can be computed as

$$\|e\|_{L^2(\Omega_m)} := \left(2\pi \int_{\Omega_m} |e|^2 r d\Omega_m\right)^{1/2}; \tag{82a}$$

$$\|e\|_{H^1(\Omega_m)} := \left(2\pi \int_{\Omega_m} \left(|e|^2 + |\tilde{\nabla}_m(e)|^2\right) r d\Omega_m\right)^{1/2}, \tag{82b}$$

where $e = x_\phi - x_{\phi,exact}$, with x_ϕ the numerical solution and $x_{\phi,exact}$ the analytical solution[13] Specifically the relative errors, $\|e_r\|_{L^2(\Omega_m)}$ and $\|e_r\|_{H^1(\Omega_m)}$, can be defined such that

$$\|e_r\|_{L^2(\Omega_m)} := \|e\|_{L^2(\Omega_m)} / \|x_{\phi,exact}\|_{L^2(\Omega_m)}; \tag{83a}$$

$$\|e_r\|_{H^1(\Omega_m)} := \|e\|_{H^1(\Omega_m)} / \|x_{\phi,exact}\|_{H^1(\Omega_m)}. \tag{83b}$$

5.1. Time harmonic conducting sphere in a uniform amplitude background magnetic field

Consider a conducting sphere of radius $a = 1$ m, placed in a vacuum, excited by a constant amplitude time varying background magnetic field with complex amplitude $\mathcal{H}_0 = \mu_0^{-1}\nabla \times \mathcal{A}_0 = \mathcal{H}_{z,0}\boldsymbol{e}_z$ and angular frequency ω [rad s^{-1}], where $\mathcal{A}_0$ is a prescribed far field vector potential expressed in terms of complex amplitudes. The computed magnetic field $\mathcal{H} = \mu^{-1}\nabla \times \mathcal{A}$ will be spatially different to $\mathcal{H}_0$, but will tend to $\mathcal{H}_0$ far from the object. This problem is set in an unbounded domain where the sphere is defined by $\Omega_s = \{\boldsymbol{x} : |\boldsymbol{x}| \le a\}$ m^3 and the region exterior to the sphere is $\mathbb{R}^3 \setminus \overline{\Omega_s}$. The relevant physical parameters are defined in Table 1.

The position dependent permeability μ, is given by

$$\mu := \begin{cases} \mu_r\mu_0 & \text{for } \boldsymbol{x} \in \Omega_s, \\ \mu_0 & \text{for } \boldsymbol{x} \in \mathbb{R}^3 \setminus \overline{\Omega_s}. \end{cases} \tag{84}$$

This case represents a simplified form of the transmission problem (27) where there exists no mechanical or coupling terms. For this problem there exists a closed form axisymmetric solution [48] (pg. 397–399) $\mathcal{A}_{exact}(r,\phi,z) = \mathcal{A}_{\phi,exact}(r,z)\boldsymbol{e}_\phi$ in cylindrical coordinates (r,ϕ,z) with origin located at the centre of the sphere, defined as

$$\mathcal{A}_{\phi,exact}(r,z) = \begin{cases} \frac{1}{2}\mu_0^{-1}|\mathcal{B}_0|\left(r + \frac{Dr}{(r^2+z^2)^{3/2}}\right) & \text{for } (r^2+z^2)^{1/2} > a, \\ \frac{1}{2}\mu_0^{-1}C|\mathcal{B}_0|\left(r^2+z^2\right)^{-3/4} r I_3(r,z) & \text{for } (r^2+z^2)^{1/2} \le a, \end{cases} \tag{85a}$$

where C and D are defined as

$$C := \frac{3\mu_r\mu_0 v a^{3/2}}{(\mu_r\mu_0 - \mu_0)vI_1 + \left(\mu_0(1+v^2) - \mu_r\mu_0\right)I_2}, \tag{86a}$$

$$D := \frac{\left((2\mu_r\mu_0 + \mu_0)vI_1 - \left(\mu_0(1+v^2) + 2\mu_r\mu_0\right)I_2\right)a^3}{(\mu_r\mu_0 - \mu_0)vI_1 + \left(\mu_0(1+v^2) - \mu_r\mu_0\right)I_2}, \tag{86b}$$

with

$$I_1 := \sqrt{\frac{2\pi}{v}}\sinh(v); \tag{87a}$$

$$I_2 := \sqrt{\frac{2\pi}{v}}\cosh(v), \tag{87b}$$

$$I_3(r,z) := \sqrt{\frac{2\pi}{v_1(r,z)}}\frac{(\cosh(v_1(r,z)) - 1)\sinh(v_1(r,z))}{v_1(r,z)}. \tag{87c}$$

---

[13] The formulation as presented here is for a scalar field, however this can also be applied to vector fields to compute errors in the norm of the vector field.

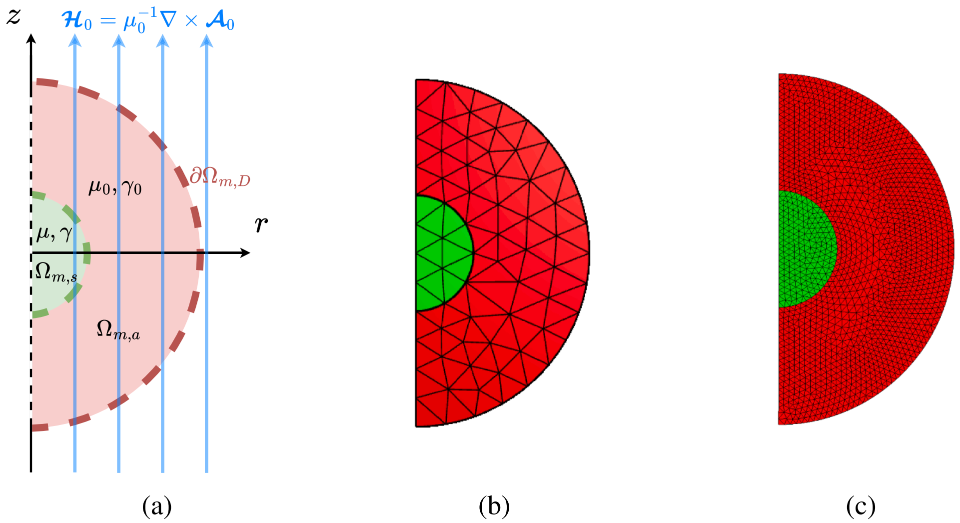

Fig. 3. Time harmonic conducting sphere in a uniform amplitude background magnetic field - (a) Illustration of computational domain on the meridian plane in cylindrical coordinates, (b) unstructured mesh of computational domain on the meridian plane corresponding to a maximum element size $h = 0.5$ m with curved elements, (c) unstructured mesh of computational domain on the meridian plane corresponding to a maximum element size $h = 0.1$ m.

In the above, I_1, I_2, and I_3 are modified spherical Bessel functions defined in terms of

$$v := \sqrt{\mathrm{i}\gamma\omega\mu_r\mu_0}\, a; \tag{88a}$$

$$v_1(r, z) := \sqrt{\mathrm{i}\gamma\omega\mu_r\mu_0}\sqrt{r^2 + z^2}. \tag{88b}$$

For the numerical solution, the unbounded domain is truncated at a radial distance of 2 m away from the spherical domain resulting in a sphere around the origin of radius $b = 3$ m, so that the truncated vacuum region is $\Omega_a = \{\boldsymbol{x} : a \le |\boldsymbol{x}| \le b\}$ m^3. Moreover, due to the rotationally invariant nature of the geometry and solution, the problem is modelled axisymmetrically and, hence, the inner spherical domain is defined in the meridian plane as $\Omega_{m,s} = \{\boldsymbol{x}_m : |\boldsymbol{x}_m| \le a\}$ m^2, and the truncated unbounded outer vacuum domain is defined in the meridian plane as $\Omega_{m,a} = \{\boldsymbol{x}_m : a \le |\boldsymbol{x}_m| \le b\}$ m^2, where the subindex $(\cdot)_m$ is used to emphasise that the solution is sought in the meridian plane Ω_m and $\boldsymbol{x}_m = (r, z)$. Following the approach in [15] and in (60a) –(60b), in order to avoid the potential singularities associated with the radial axis and the need for weighted spaces, we introduce $\hat{\mathcal{A}}_\phi = \mathcal{A}_\phi / r$ and solve for this variable. As the closed form solution to the problem is known, the Dirichlet boundary conditions $\hat{\mathcal{A}}_\phi = \hat{\mathcal{A}}_{\phi,exact}$ is applied on the boundary of the outer meridian circumference $\partial\Omega_{m,D}$ whilst symmetry conditions are applied for $\hat{\mathcal{A}}_\phi$ on the radial axis $r = 0$ as $\boldsymbol{e}_r \cdot \nabla_m \hat{\mathcal{A}}_\phi\big|_{r=0} = 0$. An illustration of the computational domain on the meridian plane illustrating the boundaries and subdomains is presented in Fig. 3a. A coarse mesh with curved elements, where the maximum element size is $h = 0.5$ m, is presented in Fig. 3b, and a much finer mesh, with maximum element size of $h = 0.1$ m, is presented in Fig. 3c.

A h-refinement study is considered to investigate the effect of varying the mesh spacing on the relative norm of the L^2 and H^1 errors by considering a mesh with spacing values $h = 0.1, 0.05, 0.025, 0.0125$ m and element order $p = 1, 2, 3, 4$ for the geometry presented in Fig. 3a, with $\omega = 2\pi[6 \times 10^1]$ rad s^{-1}. The error is measured using $\|e_r\|_{L^2(\Omega_m)}$ and $\|e_r\|_{H^1(\Omega_m)}$, in accordance to (83), and the results are presented against $1/h$ and NDOF in Fig. 4. As presented in Table 2, it can be see that the rates of convergence observed in Fig. 4 follow the *a-priori* convergence behaviour and converge at the expected rates for a smooth solution. As the solution is smooth in this case, there are benefits in employing p-refinment where the polynomial order of the elements is uniformly increased on fixed mesh as this leads to exponential convergence of the solution with respect to NDOF$^{1/2}$.

A contour plot of $\mathcal{A}_\phi$ is shown for the converged solution in Fig. 5a. Furthermore, the contour plots of $\mathcal{B}_r$ and $\mathcal{B}_z$ are included in Fig. 5b,c, respectively. For a discretisation consisting of $h = 0.1$ m and $p = 3$, the relative error of $\mathcal{A}_\phi$ and the r and z components of $\boldsymbol{\mathcal{B}}$ are shown in Fig. 6. The peak values of the relative errors are 1×10^{-5}, 1×10^{-3}, and 8×10^{-4}, respectively, which is deemed to be sufficiently small.

If the solution contains singularities or steep gradients, applying h or p-refinement alone will not achieve exponential convergence, but given an appropriate combination of h and p values, it is possible to achieve exponential convergence [47] (pg. 195), according to the *a-priori* convergence below

$$\|e_r\|_{L^2(\Omega_m)} \le C_1 \exp(\beta_1 \mathrm{NDOF}^{1/3}); \tag{89a}$$

$$\|e_r\|_{H^1(\Omega_m)} \le C_2 \exp(\beta_2 \mathrm{NDOF}^{1/3}). \tag{89b}$$

where C_1, C_2 and β_1, β_2 are scalar coefficients independent of h and p.

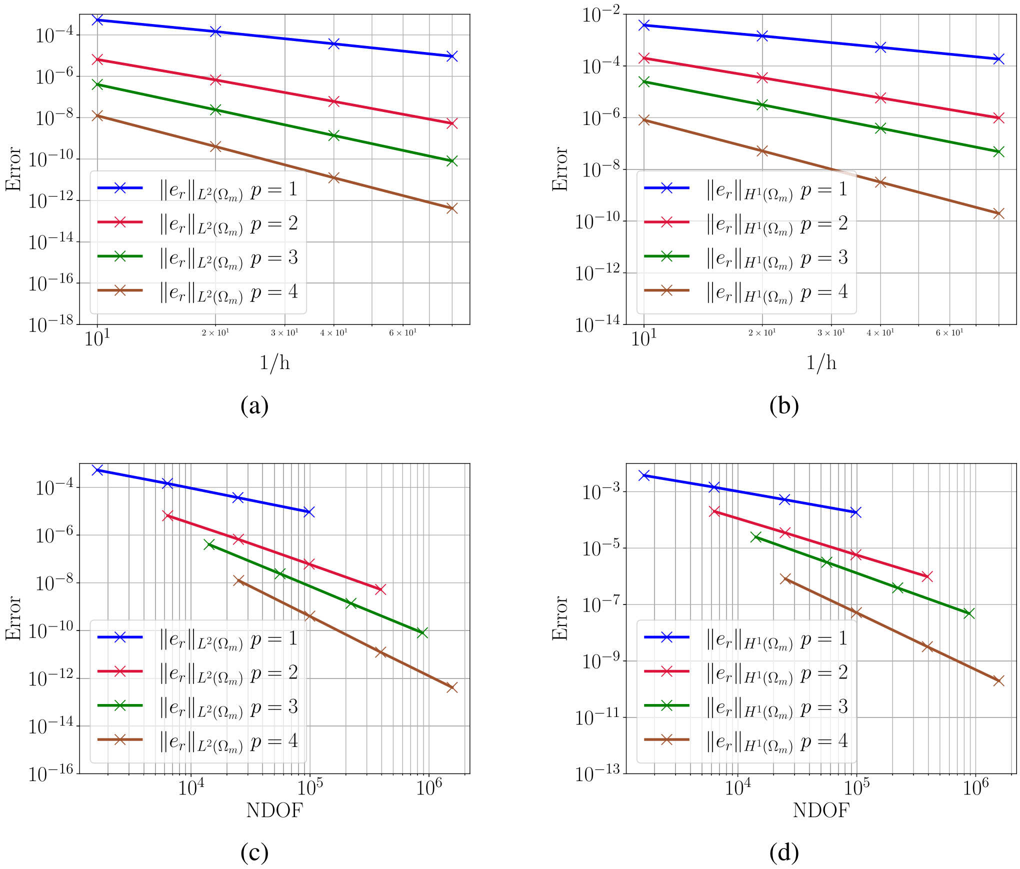

Fig. 4. Time harmonic conducting sphere in a uniform amplitude background magnetic field - Showing (a) $||e_r||_{L^2(\Omega_m)}$ against $1/h$, (b) $||e_r||_{H^1(\Omega_m)}$ against $1/h$, (c) $||e_r||_{L^2(\Omega_m)}$ against NDOF and (d) $||e_r||_{H^1(\Omega_m)}$ against NDOF for $\omega = 2\pi[1.6\times 10^0]$ rad s^{-1}, $h = 0.1, 0.05, 0.015, 0.0125$ m, $p = 1, 2, 3, 4$.

Table 2

Time harmonic conducting sphere in a uniform amplitude background magnetic field - The expected rates of convergence and measured rates of convergence for a given polynomial order of element for (a) $\|e_r\|_{L^2(\Omega_m)}$ vs $1/h$, (b) $\|e_r\|_{H^1(\Omega_m)}$ vs $1/h$, (c) $\|e_r\|_{L^2(\Omega_m)}$ vs NDOF, (d) $\|e_r\|_{H^1(\Omega_m)}$ vs NDOF.

p	Expected $(p+1)$	Measured
1	2	1.72
2	3	3.56
3	4	4.58
4	5	5.53

(a)

p	Expected (p)	Measured
1	1	1.28
2	2	2.49
3	3	3.54
4	4	4.54

(b)

p	Expected $((p+1)/2)$	Measured
1	1	0.89
2	1.5	1.80
3	2	2.29
4	2.5	2.76

(c)

p	Expected $(p/2)$	Measured
1	0.5	0.66
2	1	1.26
3	1.5	1.77
4	2	2.26

(d)

Solutions with steep gradients can occur for this problem at higher frequencies due to the skin effects associated with eddy currents being confined to the surface of the conductor. The skin depth is defined as

$$\delta = \left(2/\gamma\omega\mu_0\mu_r\right)^{1/2}, \tag{90}$$

which denotes the depth at which, below the surface of a conducting domain, the magnitude of the Ohmic current decays to $1/e$ of the magnitude at the surface [48] (pg. 393). Examining (90), it is clear that the frequency is inversely proportional to skin depth δ^2. Therefore, as the frequency increases, the fields become more confined to the surface of the conductor and high field gradients are

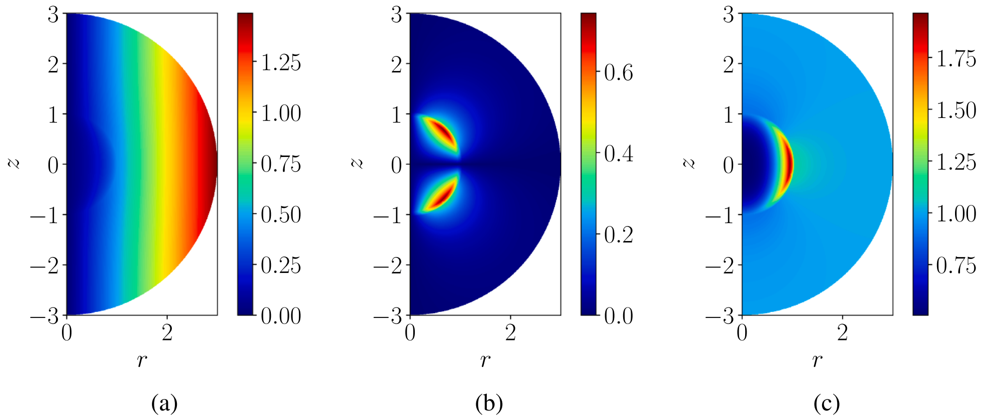

(a) (b) (c)

Fig. 5. Time harmonic conducting sphere in a uniform amplitude background magnetic field - (a) $\mathcal{A}_\phi$ [Vsm^{-1}], (b) $\mathcal{B}_r$ [T], and (c) $\mathcal{B}_z$ [T] with $\omega = 2\pi[6 \times 10^1]$ rad s^{-1}. Contour plots of the converged numerical solution corresponding to $h = 0.1$ m, $p = 4$.

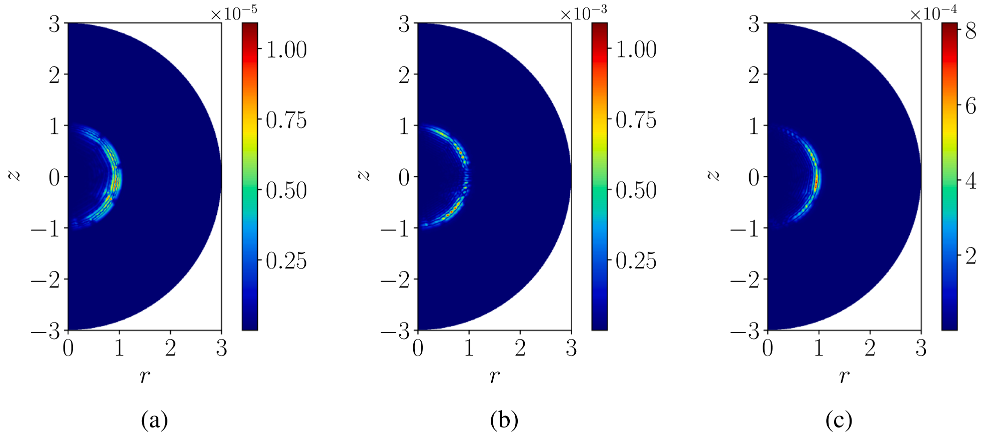

(a) (b) (c)

Fig. 6. Time harmonic conducting sphere in a uniform amplitude background magnetic field - The $|e_r|$ for (a) $\mathcal{A}_\phi$ (b) $\mathcal{B}_r$ and (c) $\mathcal{B}_z$ with $\omega = 2\pi[6 \times 10^1]$ rad s^{-1}. Contour plots of the converged numerical solution corresponding to $h = 0.1$ m, $p = 4$.

exhibited. Using the previous approach of a fixed mesh and p-refinement becomes increasingly inefficient as ω is increased. This is illustrated in Fig. 7 where $\omega = 2\pi[1.6 \times 10^0, 1.6 \times 10^1, 1.6 \times 10^2]$ rad s^{-1} in turn. Here we observe that while for low values of ω the convergence of $||e_r||_{H^1(\Omega_m)}$ and $||e_r||_{L^2(\Omega_m)}$ is exponential with respect to NDOF$^{1/2}$, the rate tends to become algebraic for high ω. To resolve this, finer spatial discretisation is required to ensure that the solution is accurately captured. But, as the conductor-vacuum interface is known, this allows for local mesh refinement along the boundary of the conductors to capture these small skin depths. We adopt so-called hp layers to selectively refine the discretisation along the boundary of the conductors. The hp layers allow for a hybrid mesh approach, where the elements near the surface of the conductors are high aspect ratio quadrilateral elements, with standard triangular elements used away from this region. This is illustrated in Fig. 8.

A study has been conducted to investigate the effect of increasing the number of hp layers on the norm of the L^2 and H^1 errors for $\omega = 2\pi[1.6 \times 10^3]$ rad s^{-1} in Fig. 9. It can be seen that there is a small decrease in the error of the solution going from 1 to 2 hp layers, however, the introduction of more layers for this ω does not improve the efficiency of the approach. Fig. 10 investigates the effect of the gradation factor of the hp layers σ_g, on the L^2 and H^1 errors. This study demonstrates the need to combine a series of meshes with different spacings near conductor-air interface to ensure a rapid (and as it happens exponentially) convergence of the solution. This idea has been further expanded, as presented in Fig. 11, where the error envelope is plotted. This demonstrates the best possible error for each mesh refinement and element order considered, and demonstrates that exponential convergence of $||e_r||_{L^2(\Omega_m)}$ and $||e_r||_{H^1(\Omega_m)}$ with respect to NDOF$^{1/3}$, as predicted by (89), can be achieved. This allows for a more accurate solution while not requiring a considerable increase in the number of degrees of freedom, as would be the case if the refinement was carried out with triangular elements instead.

With the introduction of the hp layers, it is possible to accurately capture the solution of the eddy current field $\boldsymbol{\mathcal{J}}_f = \gamma \boldsymbol{\mathcal{E}} = \mathcal{J}_\phi \boldsymbol{e}_\phi$ for higher frequencies, where $\mathcal{J}_\phi = \mathrm{i}\omega\gamma\mathcal{A}_\phi$. The converged magnitude of the (complex) eddy current component $\mathcal{J}_\phi$ has been plotted as contour plot for $\omega = 2\pi[1.6 \times 10^0, 1.6 \times 10^1, 1.6 \times 10^2]$ rad s^{-1}, in Fig. 12, which exhibits the expected skin effects where the Ohmic currents become more confined to the surface of the conductor as the frequency increases.

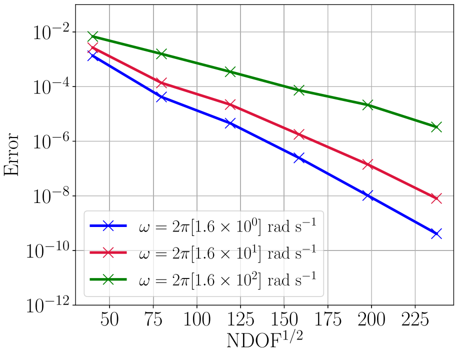

(a) (b)

Fig. 7. Time harmonic conducting sphere in a uniform amplitude background magnetic field - Showing (a) $||e_r||_{L^2(\Omega_m)}$ against NDOF$^{1/2}$, and (b) $||e_r||_{H^1(\Omega_m)}$ against NDOF$^{1/2}$ for $\omega = 2\pi[1.6 \times 10^0, 1.6 \times 10^1, 1.6 \times 10^2]$ rad s^{-1}, $h = 0.1$ m, $p = 1, 2, 3, 4, 5, 6$.

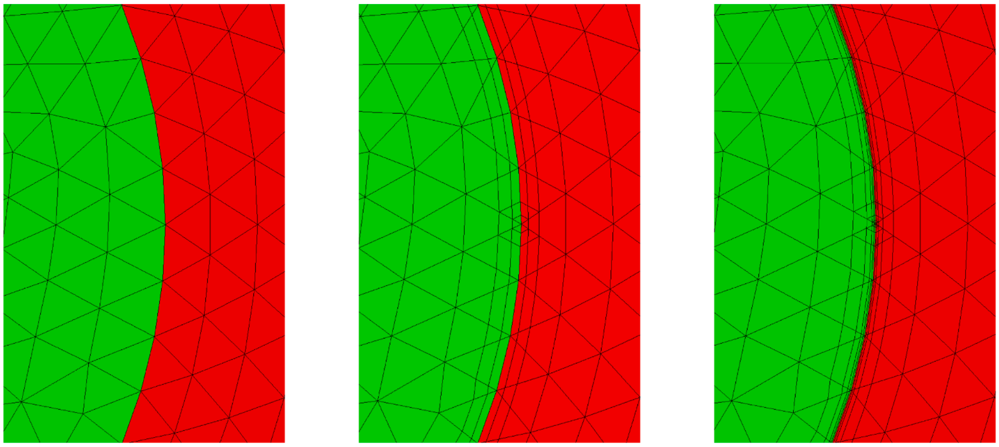

(a) hp layers = 0 (b) hp layers = 2 (c) hp layers = 4

Fig. 8. Magnified view of the additional quadrilateral layers added to the interface between the conducting sphere subdomain (green) and vacuum subdomain (red) for a hybrid mesh with (a) hp layers = 0, (b) hp layers = 2, (c) hp layers = 4 where $h = 0.25$ m, $\sigma_g = 0.5$. (For interpretation of the references to colour in this figure legend, the reader is referred to the web version of this article.)

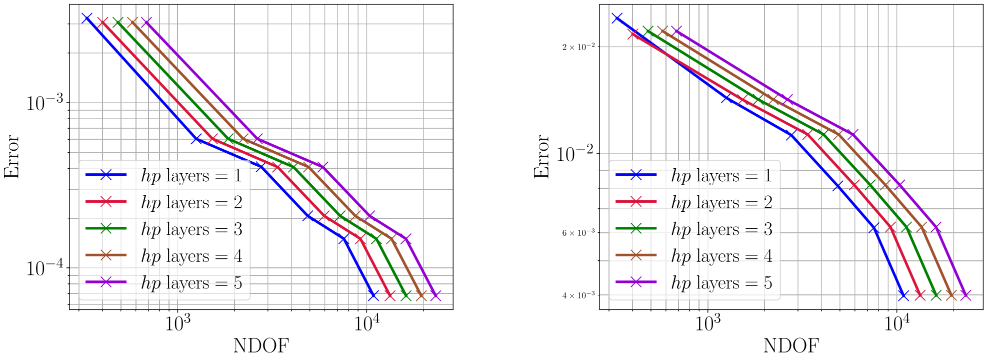

(a) (b)

Fig. 9. Time harmonic conducting sphere in a uniform amplitude background magnetic field - Showing (a) $||e_r||_{L^2(\Omega_m)}$ against NDOF, and (b) $||e_r||_{H^1(\Omega_m)}$ against NDOF for $\omega = 2\pi[1.6 \times 10^3]$ rad s^{-1}, $h = 0.25$ m, $p = 1, 2, 3, 4, 5, 6$, $\sigma_g = 0.4$.

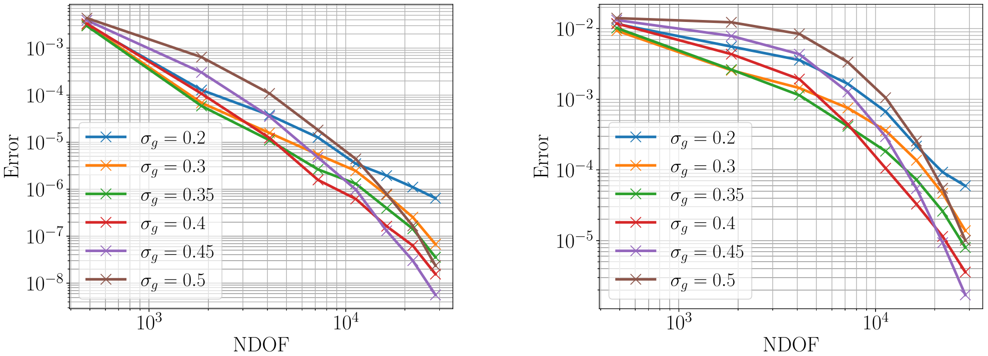

(a) (b)

Fig. 10. Time harmonic conducting sphere in a uniform amplitude background magnetic field - Showing (a) $||e_r||_{L^2(\Omega_m)}$ against NDOF, and (b) $||e_r||_{H^1(\Omega_m)}$ against NDOF for $\omega = 2\pi[1.6 \times 10^3]$ rad s^{-1}, $h = 0.25$ m, $p = 1, 2, 3, 4, 5$, $\sigma_g = 0.2, 0.3, 0.35, 0.4, 0.45, 0.5$.

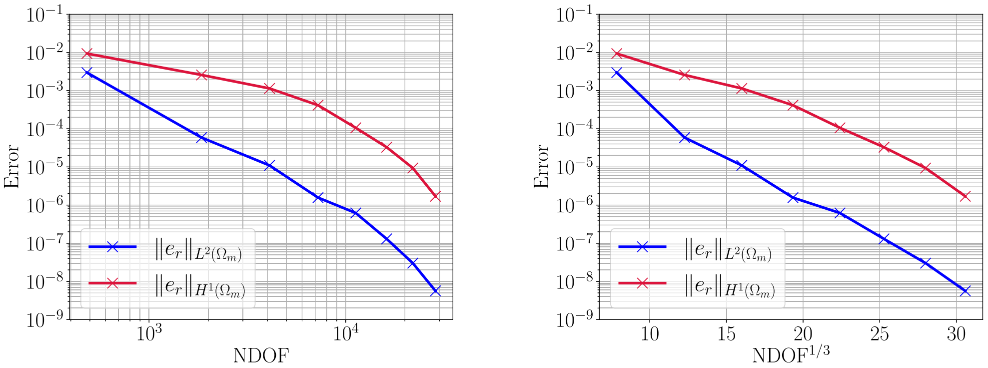

(a) (b)

Fig. 11. Time harmonic conducting sphere in a uniform amplitude background magnetic field - Showing (a) $||e_r||_{L^2(\Omega_m)}$ against NDOF, and (b) $||e_r||_{H^1(\Omega_m)}$ against NDOF$^{1/3}$ for $\omega = 2\pi[1.6 \times 10^3]$ rad s^{-1} for the best performing mesh, with a given value of σ_g, for this geometry where *hp* layers = 2, and $p = 3$.

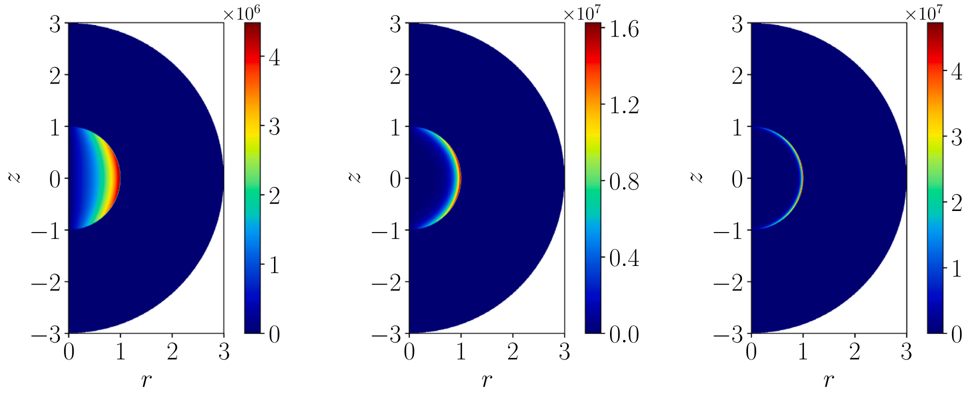

(a) $\omega = 2\pi[1.6 \times 10^0]$ rad s^{-1} (b) $\omega = 2\pi[1.6 \times 10^1]$ rad s^{-1} (c) $\omega = 2\pi[1.6 \times 10^2]$ rad s^{-1}

Fig. 12. Time harmonic conducting sphere in a uniform amplitude background magnetic field - $|\mathcal{J}_\phi|$ [A] for $\omega = 2\pi[1.6 \times 10^0, 1.6 \times 10^1, 1.6 \times 10^2]$ rad s^{-1}. Contour plots of the converged numerical solution corresponding to $h = 0.1$ m, $p = 4$, *hp* layers = 3, and $\sigma_g = 0.4$.

Table 3
Table of physical parameters for the time integration coupled magneto-mechanical problem of interest.

Parameter	Units	Value
Young's modulus – E	Pa	1×10^6
Poisson's ratio – ν	–	0.33
Density – ρ	kg m^{-3}	1×10^6
Relative permeability – μ_r	–	1
Electrical conductivity – γ	S m^{-1}	1×10^6

5.2. Time integration linearised fully coupled conducting mechanical cylinder subject to non-homogeneous dirichlet boundary conditions

Next, consider a conducting mechanical cylinder of radius $r = 1$ m and length $l = 2$ m, subject to a time varying displacement and magnetic vector potential field on the external boundaries. The domain is defined by $\Omega = \{(r, \theta, z) : 0 \le r \le 1, 0 \le \theta \le 2\pi, -1 \le z \le 1\}$ m^3. The relevant physical parameters are defined in Table 3.

This case is a solution to the transmission problem (27a). The choice was made to employ the *"method of manufactured solutions"* [49]. The form of the analytical solution is manufactured, by substituting this in to the governing equations, the required source term and boundary conditions are obtained. We define $\boldsymbol{A}^{DC}_{exact}(r, \phi, z) = A^{DC}_{\phi,exact}(r, z)\boldsymbol{e}_{\boldsymbol{\phi}}$, and $\boldsymbol{A}_{exact}(r, \phi, z, t) = A_{\phi,exact}(r, z)\sin(\omega t)\boldsymbol{e}_{\boldsymbol{\phi}}$, as static and transient axisymmetric vector potentials and similarly $\boldsymbol{u}_{exact}(r, z, t) = (u_{r,exact}(r, z)\boldsymbol{e}_r + u_{z,exact}(r, z)\boldsymbol{e}_z)\sin(\omega t)$ as a transient mechanical displacement in terms of (r, ϕ, z) with origin located at the centre of the cylinder, and

$$A^{DC}_{\phi,exact}(r, z) = r^a f^{DC}_A(z); \tag{91a}$$

$$A_{\phi,exact}(r, z) = r^b f_A(z), \tag{91b}$$

$$u_{r,exact}(r, z) = r^c f_r(z); \tag{91c}$$

$$u_{z,exact}(r, z) = r^d f_z(z), \tag{91d}$$

where a, b, c, and d are positive integer values, and $f^{DC}_A(z)$, $f_A(z)$, $f_r(z)$ and $f_r(z)$ are chosen to be polynomial functions of z. For the chosen manufactured solution, we require that $a \ge 2$, $b \ge 2$, $c \ge 2$, and $d \ge 2$ to ensure that the source term does not involve negative powers. For the results presented in this section, we make the choice $a = 3$, $b = 3$, $c = 3$, $d = 3$, $f^{DC}_A(z) = z^2$, $f_A(z) = z^3$, $f_r(z) = z^4$, and $f_z(z) = z^4$ and choose $\omega = 2\pi$ rad s^{-1}.

For the numerical solution, the problem is modelled axisymmetrically, therefore the cylindrical domain is defined on the meridian plane as $\Omega_m = \{\boldsymbol{x}_m : 0 \le r \le 1, -1 \le z \le 1\}$ m^2. Given the manufactured solution, the Dirichlet boundary condition $\hat{A}^{DC}_\phi = \hat{A}^{DC}_{\phi,exact}$, $\hat{A}_\phi = \hat{A}_{\phi,exact}$, $\hat{u}_r = \hat{u}_{r,exact}$, and $\hat{u}_z = \hat{u}_{z,exact}$ are applied on the boundaries of the outer meridian surfaces $\partial\Omega_{m,D_A}$ and $\partial\Omega_{m,D_u}$, whilst a symmetry condition are applied for $\hat{A}_\phi$ and $\boldsymbol{u}$ on the radial axis $r = 0$. An illustration of the computational domain on the meridian plane illustrating the boundaries and domain is presented in Fig. 13a. A coarse unstructured mesh with maximum element size $h = 0.1$ m, is presented in Fig. 13b, and a finer unstructured mesh with maximum element size $h = 0.05$ m, is presented in Fig. 13c.

As presented in Algorithm 2, a fixed point iteration strategy has been used to resolve the coupling and converge to a solution. For the cases presented in this section, a value of TOL$= 1 \times 10^{-8}$ has been prescribed, and the maximum number of iterations as $n^{MAX}_{iter} = 20$.

A h-refinement study is considered for meshes with spacings $h = 0.1, 0.05, 0.025, 0.0125$ m and element orders $p = 1, 2, 3, 4$, in turn, for the geometry presented in Fig. 13a, with time step $\Delta t = 1 \times 10^{-10}$ s. The error is measured using $\|e_r\|_{L^2(\Omega_m)}$ and $\|e_r\|_{H^1(\Omega_m)}$, in accordance to (83), where errors are computed for both the A_ϕ and the $\boldsymbol{u}$ fields, and evaluated at $t = 1 \times 10^{-10}$ s. This is to ensure that the system is only integrated in time over one time step and consequently the error associated with the time integration is expected to be negligible. In the interest of space, the results are presented only against NDOF in Fig. 14. As presented in Table 4, it can be seen that the rates of convergence observed in Fig. 14 follow the *a-priori* convergence behaviour and converge at the expected rates for a smooth solution.

The modified backward Euler time stepping scheme that has been utilised is second order in time [50] (pg. 328). In order to validate this, a Δt-refinement study is considered using $\Delta t = 1 \times 10^{-2}, 1 \times 10^{-2.5}, 1 \times 10^{-3}$ s with $\omega = 2\pi$ rad s^{-1}. The error is measured in accordance to (83) for both the A_ϕ and $\boldsymbol{u}$ fields, and the results are presented against $1/\Delta t$ in Fig. 15 [14] The rates of convergence for the study shown in Fig. 15 is presented in Table 5, where it can be seen that the rates of convergence observed follow the *a-priori* convergence behaviour and converge at the expected rates for both midpoint and trapezium methods of assembling the right hand side.

---

[14] The *midpoint* and *trapezium* variants, as presented in the figures, are in reference to the time integration method used to compute the last term on the right hand sides of (63a)–(63b). For all presented cases, the modified backward Euler time stepping scheme has been utilised for the solution of the vector potential equation.

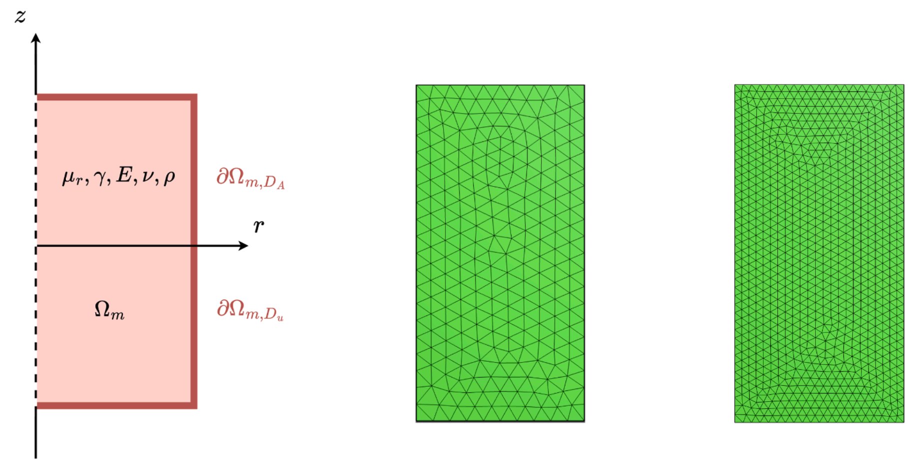

(a) (b) (c)

Fig. 13. Time integration linearised fully coupled conducting mechanical cylinder subject to non-homogeneous Dirichlet boundary conditions - (a) Illustration of computational domain on the meridian plane in cylindrical coordinates, (b) unstructured mesh of the computational domain on the meridian place corresponding to the maximum element size $h = 0.1$ m, (c) unstructured mesh of the computational domain on the meridian plane corresponding to a maximum element size $h = 0.05$ m.

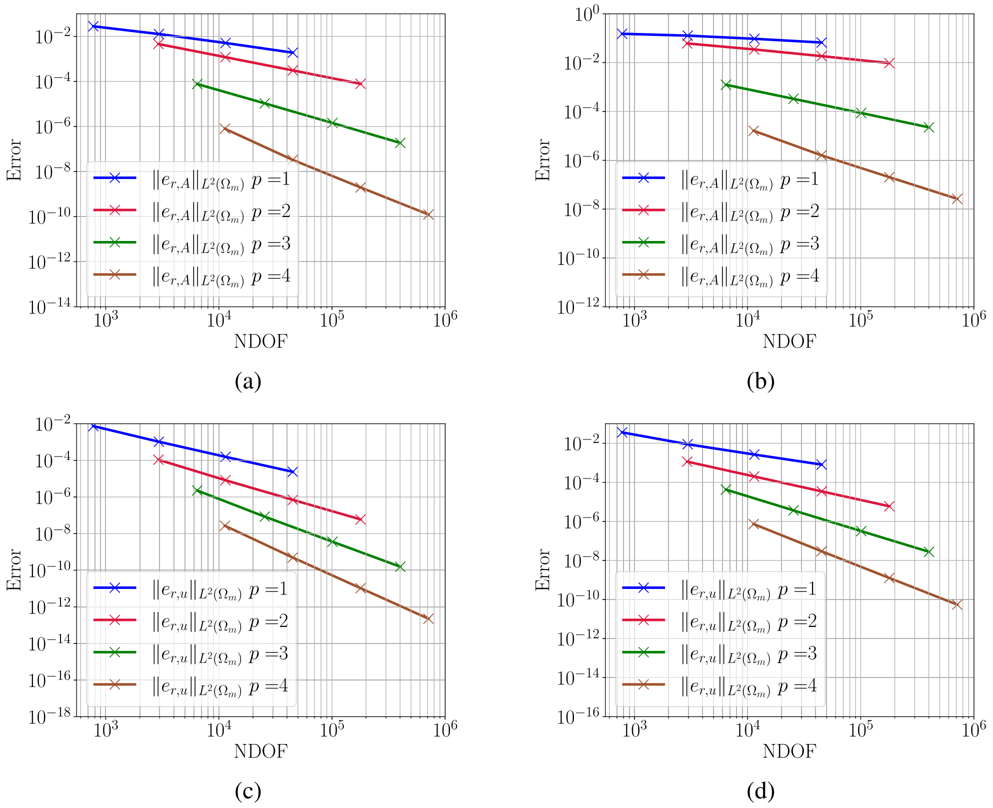

(a) (b)

(c) (d)

Fig. 14. Time integration linearised fully coupled conducting mechanical cylinder subject to non-homogeneous Dirichlet boundary conditions - Showing (a) $||e_{r,A}||_{L^2}$, (b) $||e_{r,A}||_{H^1}$, (c) $||e_{r,u}||_{L^2}$, (d) $||e_{r,u}||_{H^1}$ against NDOF for $\omega = 2\pi$ rad s^{-1}, $h = 0.1, 0.05, 0.015, 0.0125$ m, $p = 1, 2, 3, 4$.

Table 4
Time integration linearised fully coupled conducting mechanical cylinder subject to non-homogeneous Dirichlet boundary conditions - Showing rates of convergence and expected rates of convergence for (a) $||e_{r,A}||_{L^2}$, (b) $||e_{r,A}||_{H^1}$, (c) $||e_{r,u}||_{L^2}$, (d) $||e_{r,u}||_{H^1}$ against NDOF for $\omega = 2\pi$ rad s^{-1}, $h = 0.1, 0.05, 0.015, 0.0125$ m, $p = 1, 2, 3, 4$.

p	Expected $((p+1)/2)$	Measured
1	1	0.74
2	1.5	1.54
3	2	1.85

(a)

p	Expected $(p/2)$	Measured
1	0.5	0.31
2	1	1.02
3	1.5	1.41

(b)

p	Expected $((p+1)/2)$	Measured
1	1	1.46
2	1.5	1.81
3	2	2.30

(c)

p	Expected $(p/2)$	Measured
1	0.5	1.00
2	1	1.31
3	1.5	1.81

(d)

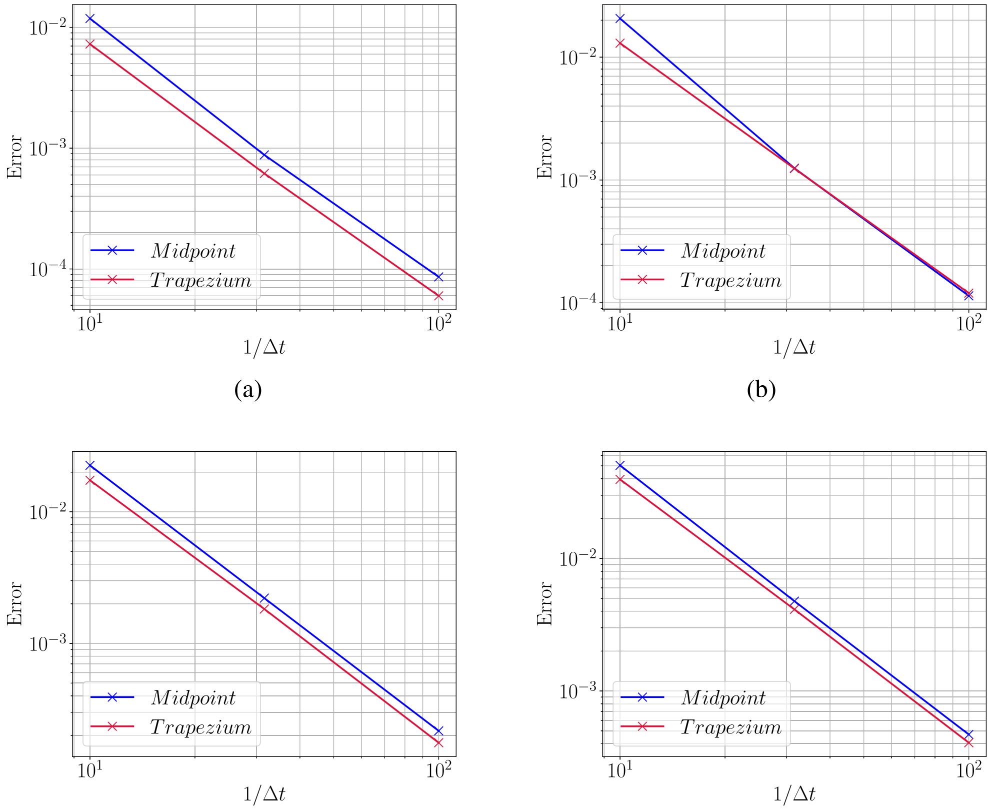

(a) (b)

(c) (d)

Fig. 15. Time integration linearised fully coupled conducting mechanical cylinder subject to non-homogeneous Dirichlet boundary conditions - Showing (a) $||e_{r,A}||_{L^2}$, (b) $||e_{r,A}||_{H^1}$, (c) $||e_{r,u}||_{L^2}$, (d) $||e_{r,u}||_{H^1}$ against $1/\Delta t$ for $\omega = 2\pi$ rad s^{-1}, $h = 0.1$ m, $p = 3$.

6. Numerical examples: MRI geometries

The preceding benchmark studies have demonstrated the advantages of p-refinement over h-refinement in problems characterised by smooth solution fields. Furthermore, in the presence of steep gradients, such as those occurring near conductor-vacuum interfaces, hp-refinement with boundary layers was shown to accurately capture the solution with significantly fewer degrees of freedom. In addition, the chosen time-integration methods have been shown to effectively obtain the transient solution with the expected second-order convergence. This establishes a solid basis for applying the solution methodology to more complex, industrially relevant problems. In the following section, we apply the approach to representative MRI magnet geometries to assess its performance

Table 5
Time integration linearised fully coupled conducting mechanical cylinder subject to non-homogeneous Dirichlet boundary conditions - Rates of convergence for $||e_{r,A}||_{L^2}$, $||e_{r,A}||_{H^1}$, $||e_{r,u}||_{L^2}$, and $||e_{r,u}||_{H^1}$ for the midpoint and trapezium methods of constructing the right hand side, for $\omega = 2\pi$ rad s^{-1}, $h = 0.1$ m, $p = 3$.

	$\|\|e_{r,A}\|\|_{L^2}$	$\|\|e_{r,A}\|\|_{H^1}$	$\|\|e_{r,u}\|\|_{L^2}$	$\|\|e_{r,u}\|\|_{H^1}$
Midpoint	2.14	2.26	2.02	2.03
Trapezium	2.09	2.04	2.00	1.99

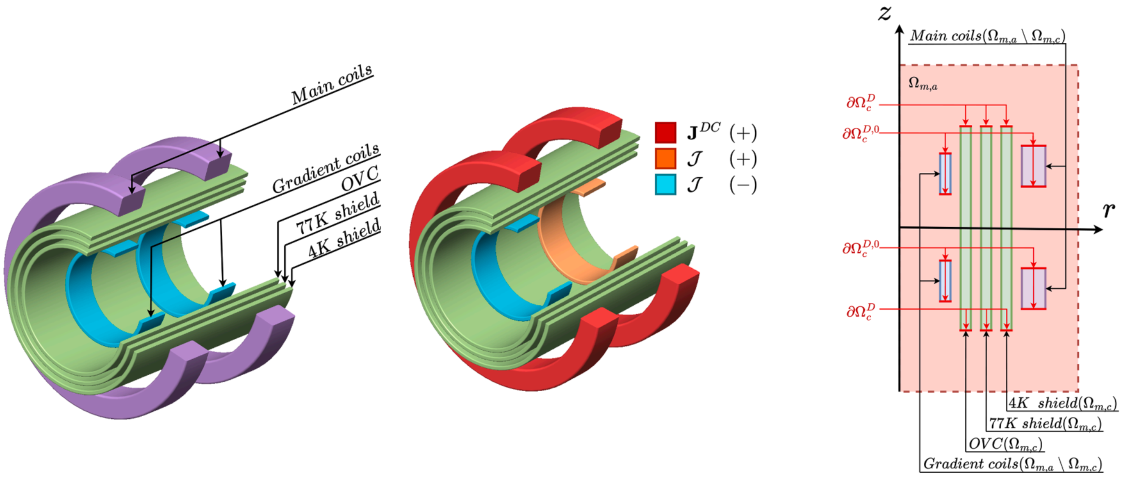

(a) (b) (c)

Fig. 16. (a) 3D representation of domain for the test magnet geometry with labels specifying each component, (b) representation of magnet coils with respective support currents, (c) illustration of computational domain on the meridian plane in cylindrical coordinates.

Table 6
Table of geometrical parameters for the coupled test magnet problem of interest. The defined measurements are the lengths of the subdomains in the r direction, and z direction.

Dimensions	Units	OVC	77K Shield	4K Shield	Main coil	Gradient coil
r direction	10^{-3} m	5	5	3	38.4	5.4
z direction	10^{-3} m	500	500	500	59.7	50.4

in realistic, application-driven contexts. The computational approach will be tested through three MRI configurations of increasing level of complexity and realism, designed win close collaboration with our industrial partner.

6.1. Test magnet problem

Consider a test MRI configuration geometry, comprised of three thin conducting cylindrical shields, two main coils carrying a static DC current and producing a static magnetic field, and two gradient coils carrying a variable AC current and producing a time varying magnetic field. The three shields are referred to as the outer vacuum chamber (OVC), the 77K radiation shield, and the 4K helium vessel, as presented in Fig. 16a. Similar geometries have been presented in past work by the group [20], however in this paper, the coils are considered mechanical bodies and the mechanical boundary conditions have been modified to include the challenging problem of floor-borne vibrations following feedback from the industrial partner. The problem is set in an unbounded domain, and has the geometrical parameters outlined in Table 6, and material parameters outlined in Table 7. Notice that the main coils do not have an electrical conductivity value. This is due to the main coils operating under cryogenic conditions, rendering them superconducting with zero electrical resistance and effectively infinite conductivity. The configuration is assumed to be placed in an unbounded region of free space. To understand the electromagnetic field and mechanical displacements we seek a solution to the transmission problem (27a).

For the numerical solution, the unbounded domain is truncated at a finite distance from the conducting shields and coils, resulting in the finite domain $\Omega_a = \{(r, \theta, z) : 0 \le r \le 3, 0 \le \theta \le 2\pi, -3 \le z \le 3\}$ m^3. The problem is modelled axisymmetrically and hence, the

Table 7

Table of material parameters for the coupled realistic magnet problem of interest.

Parameters	Units	OVC	77K Shield	4K Shield	Main coil	Gradient coil
Relative permeability – μ_r	–	1	1	1	1	1
Electrical conductivity – γ	10^6 S m^{-1}	1.4	33	1.4	N/A	59
Young's modulus – E	10^9 Pa	210	81	210	84	130
Poisson's ratio – ν	–	0.283	0.337	0.283	0.33	0.34
Density – ρ	Kg m^{-3}	7900	2698	7900	5700	8960

Table 8

Table of numerical parameters for the fully coupled magneto-mechanical test magnet problem of interest.

Parameter	p	h	hp layers	σ_g	n_{iter}^{MAX}	TOL
Value	3	1	2	0.35	20	10^{-5}

outer domain is defined in the meridian plane as $\Omega_{m,a} = \{(r,z) : (0 \le r \le 3, -3 \le z \le 3)\}$ m^2. The Dirichlet boundary conditions $\boldsymbol{\mathcal{U}} = \boldsymbol{\mathcal{U}}_D$ and $\boldsymbol{\mathcal{U}} = \mathbf{0}$ are imposed on the surfaces $\partial\Omega_c^D$ and $\partial\Omega_c^{D,0}$ located at z_{max} and z_{min} for both the shields and coils subdomains, respectively, as illustrated in Fig. 16. The currents carried by the main and gradient coils are defined as

$$\boldsymbol{J}_f^{DC} = J_\phi^{DC} \chi^{DC} \boldsymbol{e}_\phi; \tag{92a}$$

$$\boldsymbol{\mathcal{J}}_f = \mathcal{J}_\phi (\chi_{\Omega_{\mathcal{J}_f^+}} - \chi_{\Omega_{\mathcal{J}_f^-}}) \boldsymbol{e}_\phi, \tag{92b}$$

where $J_\phi^{DC} = 250 \times 10^6$ A/m^2, $\mathcal{J}_\phi = 6 \times 10^6$ A/m^2, and χ^{DC} and χ are characteristic functions defined as

$$\chi^{DC} = \begin{cases} 1 & \text{for } \boldsymbol{x} \in \Omega_{\boldsymbol{J}_f^{DC}}, \\ 0 & \text{for } \boldsymbol{x} \in \Omega_{m,a} \setminus \Omega_{\boldsymbol{J}_f^{DC}}; \end{cases} \tag{93a}$$

$$\chi_{\Omega_{\mathcal{J}_f^{+,-}}} = \begin{cases} 1 & \text{for } \boldsymbol{x} \in \Omega_{\mathcal{J}_f^{+,-}}, \\ 0 & \text{for } \boldsymbol{x} \in \Omega_{m,a} \setminus \Omega_{\mathcal{J}_f^{+,-}}, \end{cases} \tag{93b}$$

Following the approach proposed by Elgy et al. [51], a value of hp layers $= 2$ and $\sigma_g = 0.35$ were selected for the surfaces of the conducting subdomains in this problem, namely, the shields, main coils, and gradient coils, as it was shown to lead to a good compromise between solution accuracy and computational cost. A complete list of numerical parameters are provided in Table 8.

Contour plots of the B_z^{DC}, $\mathcal{B}_z$, $\mathcal{U}_r$ fields are shown for the converged solution in Fig. 17a–c, respectively. The magnitude of the $\mathcal{B}_z$ field produced is of the order 1×10^{-2} T, which is two orders of magnitude smaller compared to the field strength of this particular magnet configuration, which is known to be 1.5 T at the bore of the magnet, in the z direction. As mentioned previously, this large difference in order of magnitude allows for the linearisation of the DC and AC components. Notice that in Fig. 17c, the upper coil produces a negative magnetic field and the lower coil produces a positive magnetic field in the z direction. This generates the 'gradient' in the field that MRI scanners require for imaging. The contour plot of the $\mathcal{U}_r$ fields is shown for the converged solution in Fig. 17c. For this particular case, which does not feature externally induced floor-borne vibrations, the displacements found in the shields are relatively minor for the particular frequency selected. These displacements are a result of the Maxwell stresses generated within the conducting shields.

Previous work by the group featured only a one-way coupling approach [13], which is equivalent to solving for a single fixed point iteration. For just one fixed point iteration and the current operating conditions, the magnitude of the fixed residual[15] for both $\boldsymbol{\mathcal{A}}$ and $\boldsymbol{\mathcal{U}}$ is extremely large, motivating the fixed point iteration approach for this two-way coupling problem of interest, as presented in Fig. 18. For the fully coupled staggered approach, the linear system is solved and a converged solution is obtained through the use of a fixed point iterative scheme, as presented in Algorithm 2. Following Theorem 2.4 in [52] (pg. 62), the rate of convergence for a fixed point iteration is expected to be linear, as is observed in Fig. 18, but with rates depending on frequency. Thus, it is desirable to understand the relationship between key quantities of interest, such as the angular frequency, and the rate of convergence of the fixed point iterations. For the selected frequencies of interest $\omega = 2\pi[1 \times 10^3, 2 \times 10^3, 3 \times 10^3, 3.5 \times 10^3, 4 \times 10^3, 5 \times 10^3]$ rad s^{-1}, it is apparent that particular frequencies require greater number of fixed point iterations to converge to a solution, specifically $\omega = 2\pi[3.5 \times 10^3]$ rad s^{-1}, and it is desirable to reduce the number of iterations for these frequencies. To achieve this, a selection of iterative residual-based vector methods to accelerate fixed point iterations, called the Aitken Δ^2 methods [29], has been explored.

---

[15] This residual is computed as the relative L^2 norm of the difference between successive iterates. Specifically, it is defined as Residual($\mathcal{E}$) $= \left(\int_{\Omega_m} |\boldsymbol{\mathcal{E}}^{(k+1)} - \boldsymbol{\mathcal{E}}^{(k)}|^2 d\Omega_m\right)^{1/2} / \left(\int_{\Omega_m} |\boldsymbol{\mathcal{E}}^{(k+1)}|^2 d\Omega_m\right)^{1/2}$, where $\boldsymbol{\mathcal{E}}^{(k+1)}$ and $\boldsymbol{\mathcal{E}}^{(k)}$ denote the solution at the current and previous iterations, respectively.

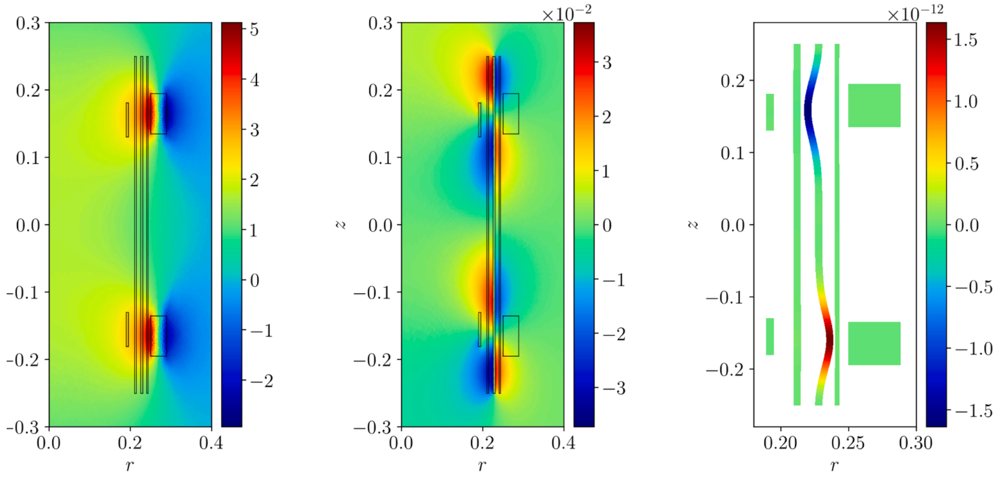

(a) (b) (c)

Fig. 17. Time harmonic fully coupled linearised test magnet problem - (a) B_z^{DC} [T], (b) $\mathrm{Re}(\mathcal{B}_r)$ [T], (c) $\mathrm{Re}(\mathcal{U}_r)$ [m] with $\omega = 2\pi[4\times 10^1]$ rad s^{-1}, with numerical parameters found in Table 8. Deformation exaggerated by a factor of 5×10^9.

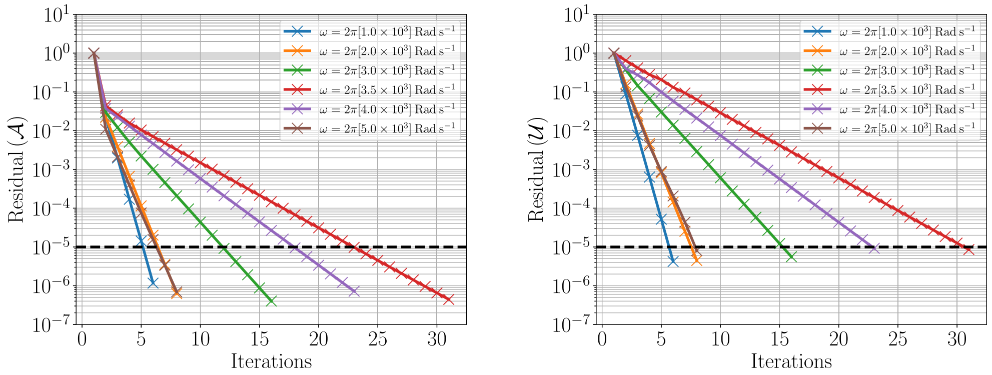

(a) (b)

Fig. 18. A Showing (a) Residual($\mathcal{A}$), (b) Residual($\mathcal{U}$) against number of fixed point iterations for frequencies $\omega = 2\pi[1\times 10^3, 2\times 10^3, 3\times 10^3, 3.5\times 10^3, 4\times 10^3, 5\times 10^3]$ rad s^{-1}, with numerical parameters found in Table 8.

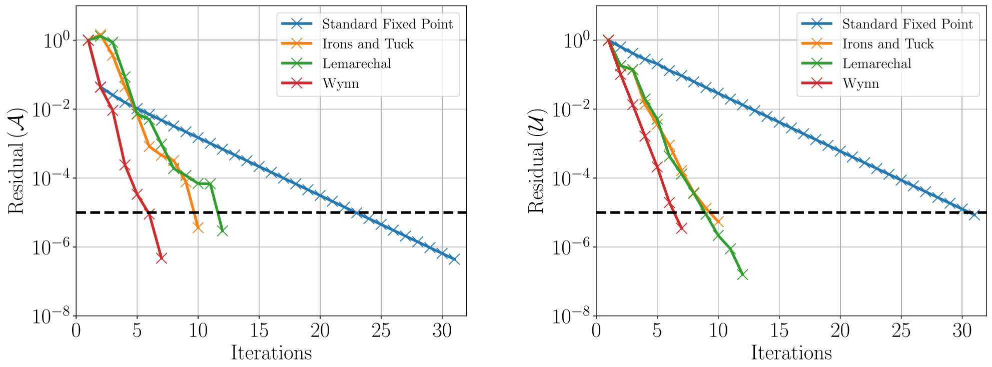

(a) (b)

Fig. 19. Time harmonic fully coupled linearised test magnet problem - Showing (a) Residual($\mathcal{A}$), (b) Residual($\mathcal{U}$) against number of fixed point iterations for the standard, Irons and Tuck, Lemarechal, and Wynn approaches to accelerate the fixed point iteration procedure, with numerical parameters found in Table 8.

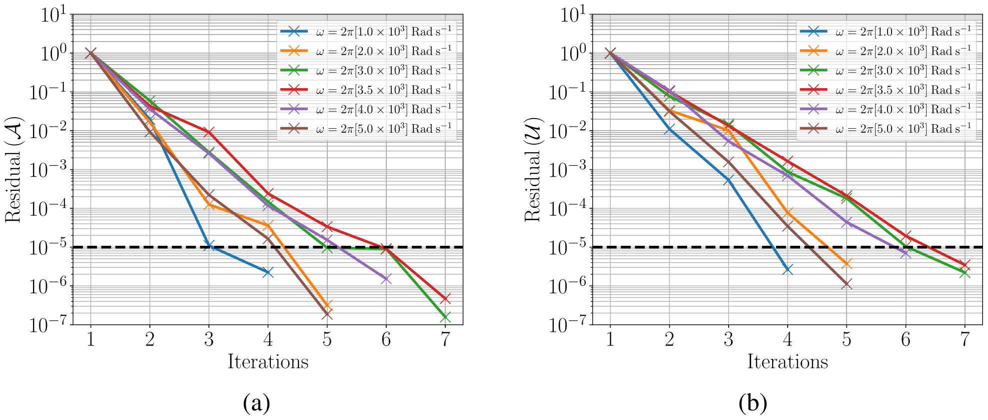

Fig. 20. Time harmonic fully coupled linearised test magnet problem - Showing (a) Residual($\mathcal{A}$), (b) Residual($\mathcal{U}$) against number of fixed point iterations using the Wynn acceleration scheme for frequencies $\omega = 2\pi[1 \times 10^3, 2 \times 10^3, 3 \times 10^3, 3.5 \times 10^3, 4 \times 10^3, 5 \times 10^3]$ rad s^{-1}, with numerical parameters found in Table 8.

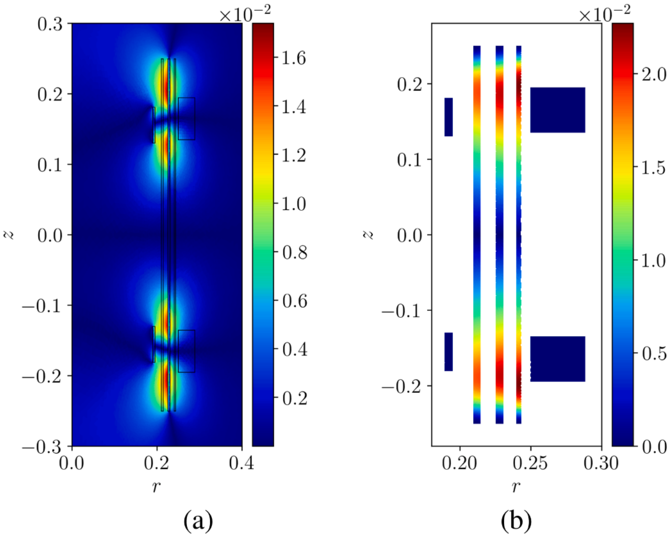

Fig. 21. Time harmonic fully coupled linearised test magnet problem - The $|e_r|$ for (a) B_z, (b) u_r at $t = 0.2625$ s, with $\Delta t = 2.5 \times 10^{-4}$ s, $\omega = 2\pi [4 \times 10^1]$ rad s^{-1}, and numerical parameters found in Table 8.

The Irons and Tuck [44], Lemarechal [45], and Wynn [46] schemes were investigated for $\omega = 2\pi[3.5 \times 10^3]$ rad s^{-1}, and are all noticeably faster than the standard fixed point scheme, as shown in Fig. 19. The approach proposed by Wynn was chosen as the preferred method for accelerating the fixed point iterations, due to the greater increase in rate of convergence and the convenient procedure to appropriately treat the complex phasor vector for this problem, compared to the alternative approaches.

The study presented in Fig. 18 was repeated using the Wynn Aitken Δ^2 method to accelerated the fixed point iterations, as presented in Fig. 20. Comparing the two sets of results, there is a clear improvement in the rate of convergence, as the worst performing frequencies, which previously required 31 iterations has now converged in 7 iterations using the new scheme, to the same residual tolerance of TOL $= 10^{-5}$.

In the time harmonic regime, the magnetic vector potential field $\boldsymbol{\mathcal{A}}(r, \phi, z) = \mathcal{A}_\phi(r, z)\boldsymbol{e}_\phi$, and the displacement field $\boldsymbol{\mathcal{U}}(r, z) = \mathcal{U}_r(r, z)\boldsymbol{e}_r + \mathcal{U}_z(r, z)\boldsymbol{e}_z$ are related to the transient solution at time t by

$$\boldsymbol{A}(r, \phi, z, t) = \operatorname{Im}\left[\boldsymbol{\mathcal{A}}(r, \phi, z)e^{\mathrm{i}\omega t}\right]; \tag{94a}$$

$$\boldsymbol{u}(r, z, t) = \operatorname{Im}\left[\boldsymbol{\mathcal{U}}(r, z)e^{\mathrm{i}\omega t}\right], \tag{94b}$$

where $\boldsymbol{\mathcal{A}}$ and $\boldsymbol{\mathcal{U}}$ are complex amplitudes of the oscillating solution[16] It is desirable to compute the discrepancy in the solution between the time harmonic and time integration approach to validate the two methods of temporal discretisation. To compare results, solutions

---

[16] The imaginary component of the solution is required here due to the choice of the transient solution being a sine type wave.

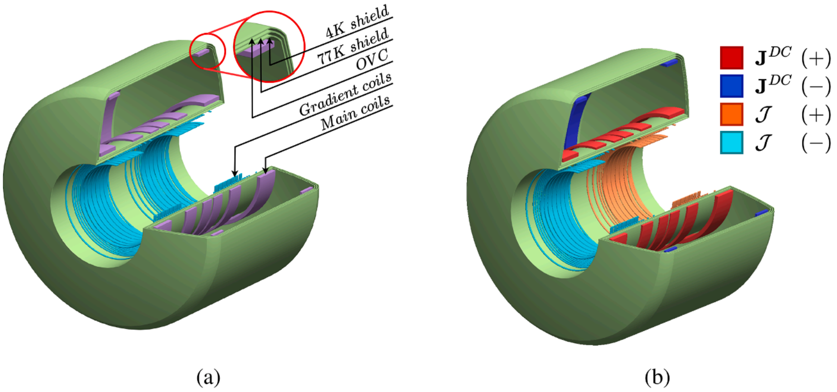

Fig. 22. (a) 3D representation of domain for the realistic magnet geometry with labels specifying each component, (b) representation of magnet coils with respective support currents.

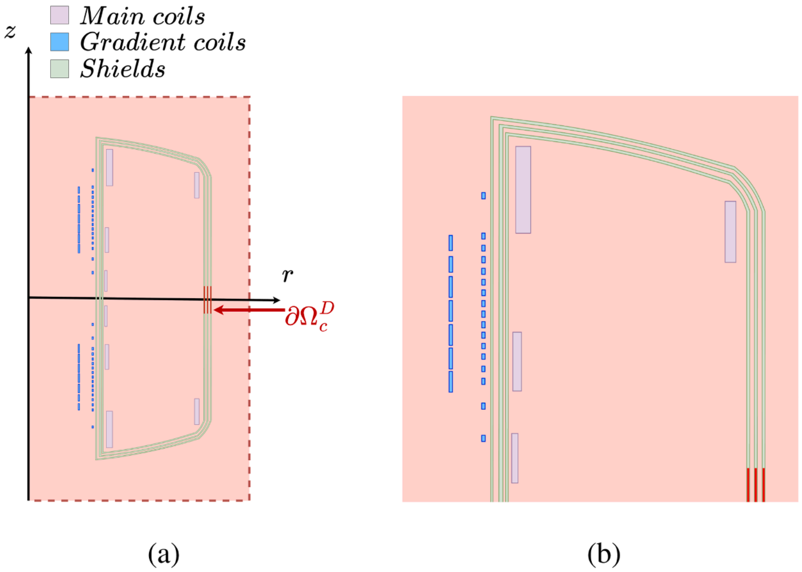

Fig. 23. (a) Illustration of computational domain on the meridian plane in cylindrical coordinates, (b) close-up image.

are sought using the geometry presented in Figure 16 and the problem parameters listed in Table 7 using both the time harmonic and time integration approaches. For the time harmonic and time integration approaches, Dirichlet boundary conditions of the form

$$\mathcal{U}^D = \mathcal{U}_r^D \boldsymbol{e}_r + \mathcal{U}_z^D \boldsymbol{e}_z; \tag{95a}$$

$$\boldsymbol{u}^D(t) = (u_r^D \boldsymbol{e}_r + u_z^D \boldsymbol{e}_z)\sin(\omega t), \tag{95b}$$

are prescribed, respectively, where $\mathcal{U}_r^D = u_r^D = 0$ m, $\mathcal{U}_z^D = u_z^D = 2 \times 10^{-3}$ m, and with $\omega = 2\pi[4 \times 10^1]$ rad s^{-1}. For the time integration approach, a linear ramp is introduced to both time dependent variables where the magnitude of $J(t)$, $u_r(t)$, and $u_z(t)$ are linearly increased between $t = 0$ s and $t = 0.13125$ s, which represents 5 periods of sine wave oscillations, to ensure that the rate of change for the quantities reaches a steady state. Contour plots of the relative discrepancy between the time integrated and time harmonic solutions through application of (83) and setting the exact solution to be the solution obtained from the time harmonic approach evaluated at time $t = 0.2625$ s, which represents 10.25 periods of sine wave oscillations, for both the A_ϕ and u_z fields is presented in Fig. 21. For this discretisation, the peak values of the relative discrepancies for the A_ϕ and u_z fields are 1×10^{-2}, which is deemed to be sufficiently small.

6.2. Realistic magnet problem

Consider a rotationally symmetric realistic MRI configuration geometry, comprised of three thin conducting toroidal shells, 8 main coils carrying a static DC current and producing a static magnetic field, and 48 gradient coils carrying a variable AC current and producing a time varying magnetic field. The three shields are referred to as the outer vacuum chamber (OVC), the 77K radiation

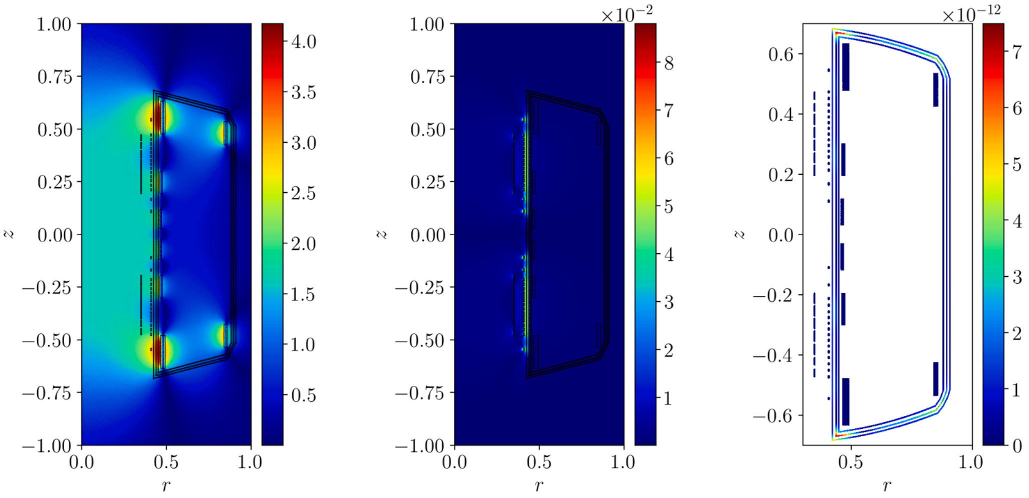

(a) (b) (c)

Fig. 24. Time integration fully coupled linearised realistic magnet problem - (a) B_z^{DC} [T], (b) B_r [T], (c) u_r [m] at $t = 0.2625$ s, with $\Delta t = 2.5 \times 10^{-4}$ s, $\omega = 2\pi\ [4 \times 10^1]$ rad s^{-1}, and numerical parameters found in Table 8.

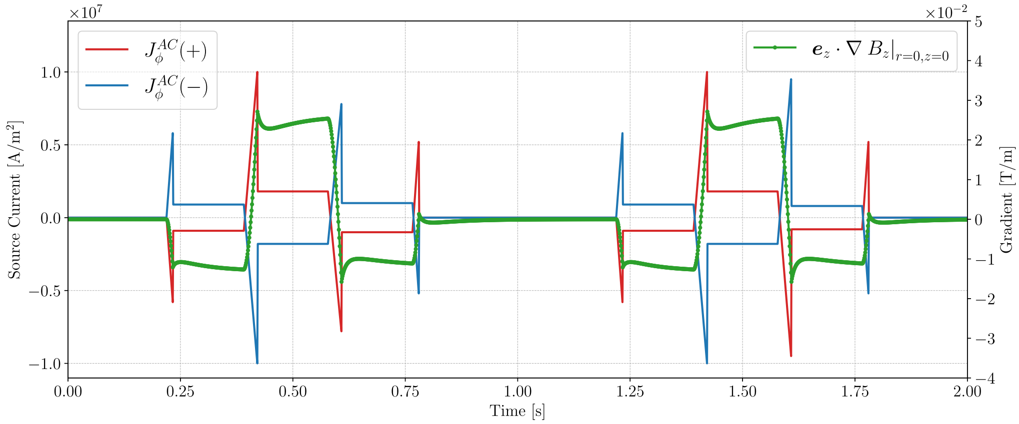

Fig. 25. Time integration fully coupled non-linear realistic magnet problem - Gradient coil source current over time (measured on left axis) and resulting gradient of the B_z field at the bore of the magnet along the z direction over time (measured on right axis).

shield, and the 4K helium vessel, as presented in Fig. 22a. Similar geometries have been briefly presented in past work by the group [41], which has been further expanded upon in this paper. The problem is set in an unbounded domain, and has the material parameters outlined in Table 7. The configuration is assumed to be placed in an unbounded region of free space. To understand the electromagnetic field and mechanical displacements we seek a solution to the transmission problem (27).

For the numerical solution, the unbounded domain is truncated at a finite distance from the conducting shields and coils, resulting in the finite domain $\Omega_a = \{(r, \theta, z) : 0 \le r \le 3, 0 \le \theta \le 2\pi, -3 \le z \le 3\}$ m^3. The problem is modelled axisymmetrically and hence, the outer domain is defined in the meridian plane as $\Omega_{m,a} = \{(r, z) : (0 \le r \le 3, -3 \le z \le 3)\}$ m^2. The Dirichlet boundary condition $\boldsymbol{u} = \boldsymbol{0}$ is imposed on the surfaces $\partial\Omega_c^{D,0}$ located at z_{max} and z_{min} for the coils subdomains. Furthermore, the Dirichlet boundary condition $\boldsymbol{u} = \boldsymbol{u}^D$ is imposed on the surfaces $\partial\Omega_c^D$ located on the internal r_{min} surfaces of the conducting shields, as illustrated in Fig. 23. The currents carried by the main and gradient coils are defined as $\boldsymbol{J}_f^{DC} = J_\phi^{DC}\chi^{DC}\boldsymbol{e}_\phi$, $\boldsymbol{\mathcal{J}}_f = \mathcal{J}_\phi(\chi_{\Omega_{\mathcal{J}_f^+}} - \chi_{\Omega_{\mathcal{J}_f^-}})\boldsymbol{e}_\phi$ where $J_\phi^{DC} = 2.35 \times 10^8$ A/m^2, $\mathcal{J}_\phi = 0.2 J_\phi^{DC}$ A/m^2, and χ^{DC} and χ are characteristic functions defined in (93).

Numerical solutions presented by the group thus far represents gradient coils that vary through time sinusoidally. In a realistic imaging setting, this is not the case, and gradient coils undergo specific current sequences which leads to a specific gradient in the magnetic field at the bore of the magnet in the z direction at a given time, called a gradient echo pulse [53]. Presented in Fig. 25 is the current provided to the gradient coils as a function of time (measure on the left axis), and the gradient of the magnetic field at the bore of the magnet along the z direction as a result of the gradient coils (measured on the right axis). Several snapshots of the B_z field has been produced during this echo sequence, at time instants $t = 0.25, 0.45, 0.65$ s, denoted by the red markers in Fig. 25, which have

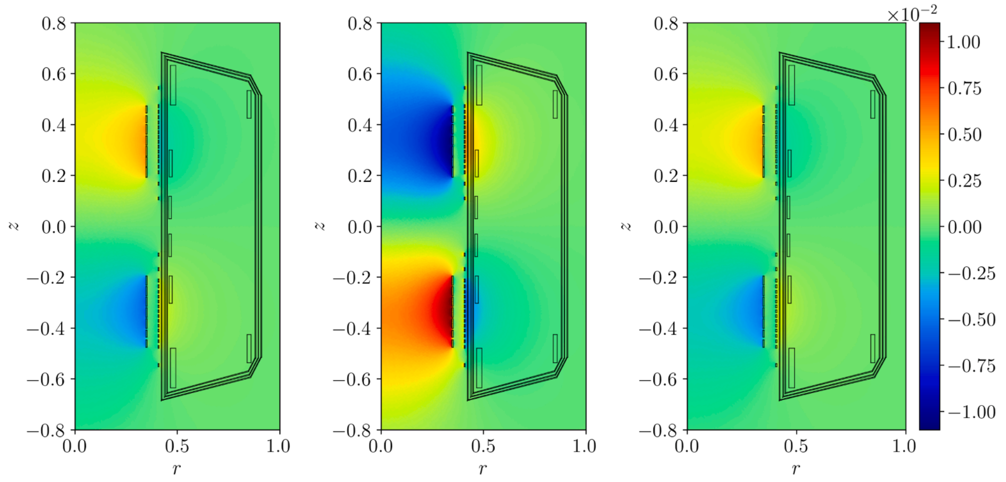

(a) (b) (c)

Fig. 26. Time integration fully coupled linearised realistic magnet problem – B_z [T] at (a) $t = 0.25$ s, (b) $t = 0.45$ s, (c) $t = 0.65$ s, with $\Delta t = 2.5 \times 10^{-4}$ s.

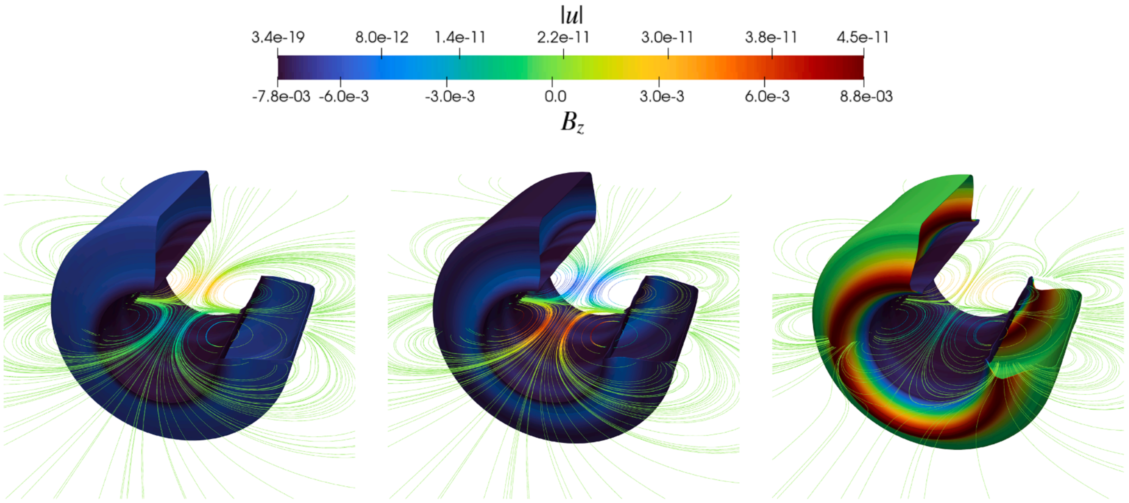

(a) (b) (c)

Fig. 27. Three-dimensional (scaled) deformation of the 77 K shield and magnetic field contour lines at (a) $t = 0.25$ s, (b) $t = 0.45$ s, (c) $t = 0.65$ s, with $\Delta t = 2.5 \times 10^{-4}$ s.

been presented in Fig. 26a, b, c, respectively. Furthermore, the B_z field at time instants $t = 0.25, 0.45, 0.65$ s have been presented in Fig. 26a, b, c, respectively. The gradient in the field produced by the gradient coils along the bore of the magnet is clearly visible and can be seen to be changing in strength at the different points in the gradient echo pulse sequence. Fig. 27 shows a three-dimensional representation with (scaled) deformations of the 77 K shield along with the magnetic field contour lines displayed at the meridian plane.

Recalling the linearisation of the coupling terms as presented in (35) and (38), this approximation only holds for the cases where the relative magnitude of the AC component is negligible compared to the DC components and the displacements are sufficiently small. In cases where the field strength of the MRI scanner is lower, and hence the DC component is smaller, or the displacements are larger, the non-linear component of the coupling terms become more dominant. To investigate the effect of the non-linear components of the coupling terms on the solution, especially in cases where they would be expected to have more influence, solutions are sought using the geometry presented in Fig. 22 and the problem parameters listed in Table 7 using both the linearised and non-linear forms of the coupling terms. For this case, the Dirichlet boundary conditions were prescribed to the shields in accordance to (95), where $\mathcal{U}_r^D = u_r^D = 0$ m, $\mathcal{U}_z^D = u_z^D = 2 \times 10^{-3}$ m, and with $\omega = 2\pi[4 \times 10^1]$ rad s^{-1}. Furthermore, the source current provided to the main coils is $J_\phi^{DC} = 8 \times 10^7$ A/m^2. As a result, the strength of the field at the bore of the magnet in the z direction is 0.55 T. The relative discrepancy between solution fields using the linearised and non-linear forms of the coupling terms have been presented in Fig. 28a,

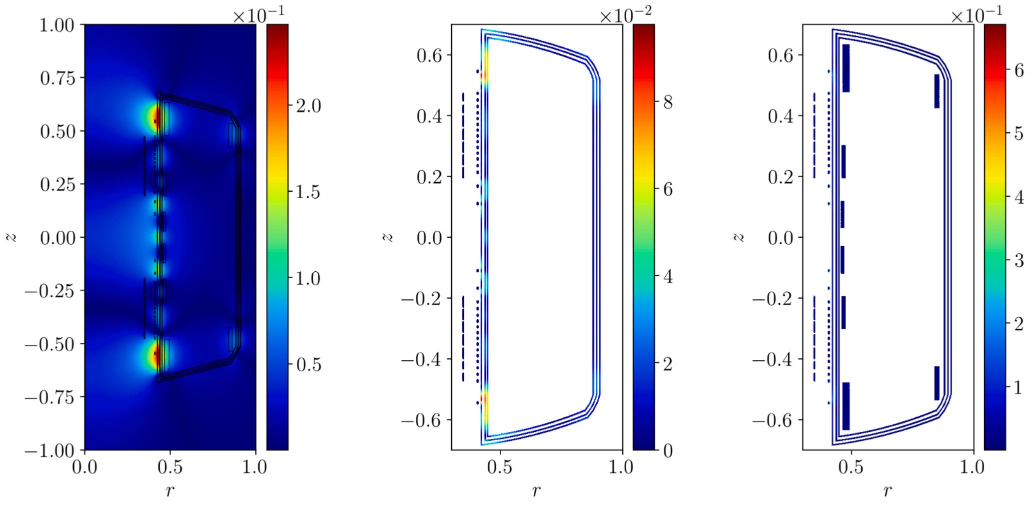

(a) (b) (c)

Fig. 28. Time integration fully coupled test magnet problem - The $|e_r|$ for (a) B_z, (b) $\mathcal{J}_{\mathcal{L}}$, (c) $\tau_{\infty,rz}$ at $t = 0.2625$ s, with $\Delta t = 2.5 \times 10^{-4}$ s, $\omega = 2\pi\,[4 \times 10^1]$ rad s^{-1}, and numerical parameters found in Table 8.

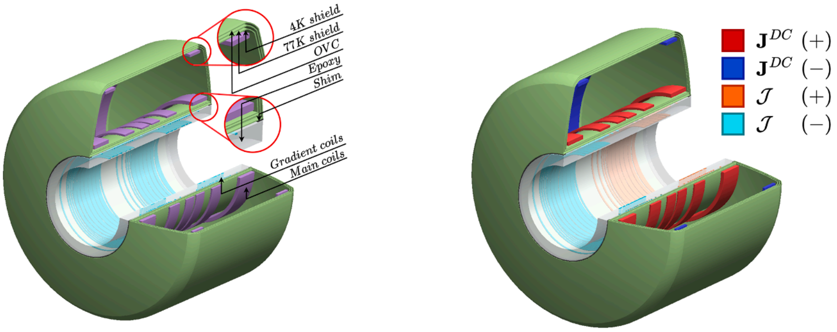

(a) (b)

Fig. 29. (a) 3D representation of domain for the realistic magnet geometry with labels specifying each component, (b) representation of magnet coils with respective support currents.

Table 9
Table of additional material parameters for the coupled realistic magnet problem of interest.

Parameters	Units	Epoxy	Shim
Relative permeability – μ_r	-*	1	1
Electrical conductivity - γ	10^6 S m^{-1}	0	0
Young's modulus – E	10^9 Pa	2.75	13
Poisson's ratio – ν	–	0.4	0.13
Density – ρ	Kg m^{-3}	1160	1850

b, c for the B_z, $\mathcal{J}_{\mathcal{L}}$, and $\tau_{\infty,rz}$ fields, respectively. The order of the relative discrepancy for this case is seen to range from 8×10^{-2} to 6×10^{-1} which is an extremely high discrepancy and motivates the use of the non-linear coupling terms, especially for cases such as the one presented.

6.3. Realistic magnet problem - epoxy casing

Consider a rotationally symmetric, realistic MRI system geometry, analogous to the configuration presented in the previous section, but with the gradient coils encapsulated in epoxy resin and mechanically affixed to the outer vacuum chamber (OVC) via fibreglass shims, as presented in Figs. 29 and 30. This more accurately represents the gradient coils and, in particular, their mechanical coupling to the shielding structures as found in actual MRI scanners. The configuration is assumed to be placed in an unbounded region of free

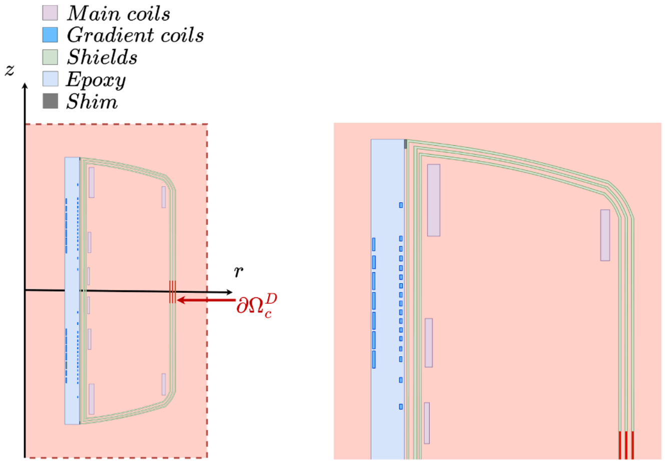

(a) (b)

Fig. 30. (a) Illustration of computational domain on the meridian plane in cylindrical coordinates, (b) close-up image.

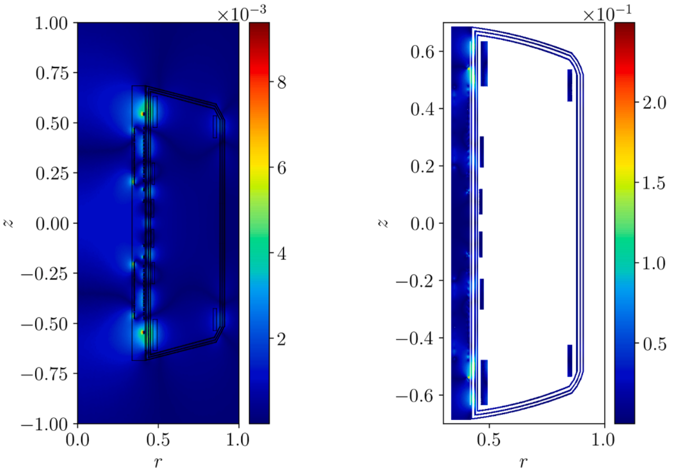

(a) (b)

Fig. 31. Time integration fully coupled realistic magnet problem with epoxy casing - The $|e_r|$ for (a) B_z, (b) $\tau_{\infty,rz}$ at $t = 0.2625$ s, with $\Delta t = 2.5\times10^{-4}$ s, $\omega = 2\pi\ [4\times10^1]$ rad s^{-1}, and numerical parameters found in Table 8.

space. To understand the electromagnetic field and mechanical displacements we seek a solution to the transmission problem (27). The problem has the additional material parameters outlined in Table 9.

For the numerical solution, the unbounded domain is truncated at a finite distance from the conducting shields and coils, resulting in the finite domain $\Omega_a = \{(r,\theta,z) : 0 \le r \le 3, 0 \le \theta \le 2\pi, -3 \le z \le 3\}$ m^3. The problem is modelled axisymmetrically and hence, the outer domain is defined in the meridian plane as $\Omega_{m,a} = \{(r,z) : (0 \le r \le 3, -3 \le z \le 3)\}$ m^2. The Dirichlet boundary condition $\boldsymbol{u} = \boldsymbol{0}$ is imposed on the surfaces $\partial\Omega_c^{D,0}$ located at z_{max} and z_{min} for only the main coils subdomains. Furthermore, the Dirichlet boundary condition $\boldsymbol{u} = \boldsymbol{u}^D$ is imposed on the surfaces $\partial\Omega_c^D$ located on the internal r_{min} surfaces of the conducting shields, as illustrated in Fig. 23. The currents carried by the main and gradient coils are defined as $\boldsymbol{J}_f^{DC} = J_\phi^{DC}\chi^{DC}\boldsymbol{e}_\phi$, $\boldsymbol{\mathcal{J}}_f = \mathcal{J}_\phi(\chi_{\Omega_{\mathcal{J}_f^+}} - \chi_{\Omega_{\mathcal{J}_f^-}})\boldsymbol{e}_\phi$ where $J_\phi^{DC} = 2.35\times10^8$ A/m^2, $\mathcal{J}_\phi = 0.2J_\phi^{DC}$ A/m^2, and χ^{DC} and χ are characteristic functions defined in (93).

To investigate the effect of the non-linear components on the solution, in cases where they would be expected to have more influence, solutions are sought using the geometry presented in Fig. 29 and Fig. 30 and the problem parameters listed in Table 7 using both the linearised and non-linear forms of the coupling terms. Due to the additional movement expected from the gradient coils for this case, it is expected that the discrepancy would be greater between the linearised and non-linear forms of the coupling terms. The relative discrepancy between solution fields using the linearised and non-linear forms of the coupling terms have been presented in Fig. 31a, b for the B_z, and $\tau_{\infty,rz}$ fields, respectively. Furthermore, the relative discrepancy for the u_z and $\mathcal{J}_{\mathcal{L}}$ fields are presented in Fig. 32a, b, respectively. The relative discrepancy for the B_z and u_z are of the order 8×10^{-3} and 4×10^{-4}, respectively.

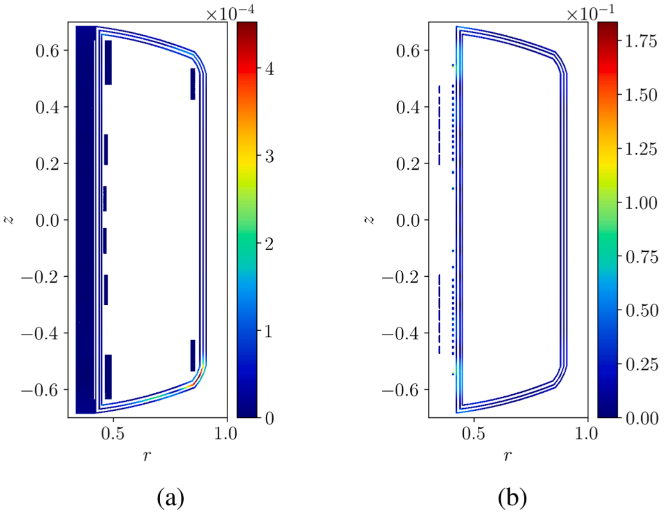

(a) (b)

Fig. 32. Time integration fully coupled realistic magnet problem with epoxy casing - The $|e_r|$ for (a) u_z, (b) $\mathcal{J}_{\mathcal{L}}$ at $t = 0.2625$ s, with $\Delta t = 2.5 \times 10^{-4}$ s, $\omega = 2\pi\ [4 \times 10^1]$ rad s^{-1}, and numerical parameters found in Table 8.

This may be considered acceptable, however for the fields of the derived quantities $\tau_{\infty,rz}$ and $\mathcal{J}_{\mathcal{L}}$, the relative discrepancy is of the order 2×10^{-1} and 1.75×10^{-1}, respectively, which are high discrepancies and once again motivates the use of the non-linear coupling terms.

7. Concluding remarks

The performance of Magnetic Resonance Imaging systems critically depends on the stability of both the highly uniform magnetic fields produced by superconducting main coils and the spatially varying, time-dependent fields generated by AC gradient coils. These two systems operate in distinct thermal environments, that is, the main coils are housed within a cryostat–comprising nested radiation shields and a helium vessel maintaining cryogenic temperatures, whilst the gradient coils are mounted externally at ambient conditions. Floor-borne vibrations, both in vertical and lateral directions, can induce relative motion between the cryostat components and the magnet assembly. This mechanical disturbance generates eddy currents in the radiation shields, producing parasitic magnetic fields that degrade field homogeneity, thus introducing image artefacts and ghosting.

This work has presented a high-fidelity computational framework for the simulation of the coupled magneto-mechanical response of axisymmetric MRI systems subject to floor-borne vibrations. Three main methodological advancements have been introduced. **First**, building upon prior linearised frequency-domain formulations, the full nonlinear coupled magneto-mechanical problem has been solved using an *hp*-Finite Element Method (*hp*-FEM), implemented in the NGSolve framework [28]. The impact of interpolation order p and the size of the time step on the solution accuracy has been systematically investigated. **Second**, the mechanical response of the main and gradient coils has been explicitly modelled, moving beyond prior idealised current-source representations based on Biot-Savart approximations. **Third**, within the context of axisymmetric MRI scanners, realistic geometries have been considered including detailed structural connectivity among the gradient coils, main coils and radiation shields. Numerical results for axisymmetric MRI configurations have been presented to validate the framework, highlight the influence of FBV on magnetic field integrity, and demonstrate the method's capability to inform design improvements and vibration mitigation strategies. Specifically, the computational approach is evaluated using three MRI configurations of increasing complexity and realism, developed in close collaboration with our industrial partner. Implementation of the presented methodology into a more general (and more computationally intensive) three-dimensional framework constitutes the next step of our work.

CRediT authorship contribution statement

Yashwanth Sooriyakanthan: Writing – review & editing, Writing – original draft, Visualization, Validation, Software, Methodology, Investigation, Data curation; **Antonio J. Gil:** Writing – review & editing, Writing – original draft, Supervision, Project administration, Methodology, Investigation, Funding acquisition, Formal analysis, Conceptualization; **Paul D. Ledger:** Writing – review & editing, Supervision, Methodology, Investigation, Funding acquisition, Formal analysis, Conceptualization; **Michael J. Mallett:** Writing – review & editing, Supervision, Funding acquisition, Conceptualization.

Data availability

Data will be made available on request.

Declaration of competing interest

The authors declare the following financial interests/personal relationships which may be considered as potential competing interests: Yashwanth Sooriyakanthan reports financial support was provided by Engineering and Physical Sciences Research Council. Antonio J. Gil reports financial support was provided by The Leverhulme Trust. Paul D. Ledger reports financial support was provided by UK International Centre for Mathematical Sciences. If there are other authors, they declare that they have no known competing financial interests or personal relationships that could have appeared to influence the work reported in this paper.

Acknowledgements

Y. Sooriyakanthan is grateful to the UK Engineering and Physical Sciences Research Council and Siemens Healthineers for a CASE Award PhD studentship that has supported this work. A. J. Gil acknowledges the financial support of UK The Leverhulme Trust through a Leverhulme Trust Fellowship. P.D. Ledger acknowledges the financial support of the UK International Centre for Mathematical Sciences (ICMS) through a KE_Catalyst project.

References

[1] I.I. Rabi, J.R. Zacharias, S. Millman, P. Kusch, A new method of measuring nuclear magnetic moment, Phys. Rev. 53 (1938) 318. https://doi.org/10.1103/PhysRev.53.318

[2] E.L. Hahn, Nuclear induction due to free larmor precession, Phys. Rev. 77 (1950) 297–298. https://doi.org/10.1103/PhysRev.77.297.2

[3] E.L. Hahn, Spin echoes, Phys. Rev. 80 (1950) 580–594. https://doi.org/10.1103/PhysRev.80.580

[4] B. Gruber, M. Froeling, T. Leiner, D.W.J. Klomp, RF coils: a practical guide for nonphysicists, J. Magn. Reson. Imaging 48 (3) (2018) 590–604. https://doi.org/10.1002/jmri.26187

[5] J.R. Singer, Blood flow rates by nuclear magnetic resonance measurements, Sci. (New York, N.Y.), 130 (3389) (1959) 1652–1653. https://doi.org/10.1126/science.130.3389.1652

[6] H.Y. Carr, Steady-State free precession in nuclear magnetic resonance, Phys. Rev. 112 (1958) 1693–1701. https://doi.org/10.1103/PhysRev.112.1693

[7] J.A. Chalela, C.S. Kidwell, L.M. Netwich, M. Luby, J.A. Butman, A.M. Demchuk, M.D. Hill, N. Patronas, L. Latour, S. Warach, Magnetic resonance imaging and computed tomography in emergency assessment of patients with suspected acute stroke: a prospective comparison, Lancet 396 (9558) (2007) 293–298. https://doi.org/10.1016/S0140-6736(07)60151-2

[8] T. Platt, M.E. Ladd, D. Paech, Tesla and beyond: advanced methods and clinical applications in magnetic resonance imaging, Invest Radiol. 56 (11) (2021) 705–725. https://doi.org/10.1097/RLI.0000000000000820

[9] M.G. Harisinghani, A. O'Shea, R. Weissleder, Advances in clinical MRI technology, Sci. Transl. Med. 11 (523) (2019). https://doi.org/10.1126/scitranslmed.aba2591

[10] R.G. Beets-Tan, G.L. Beets, A.C. Borstlap, T.K. Oei, T.M. Teune, M.F. von Meyenfeldt, J.M. Engelshoven, Preoperative assessment of local tumor extent in advanced rectal cancer: CT or high-resolution MRI?, Abdom Imaging. 25 (5) (2000) 533–541. https://doi.org/10.1007/s002610000086

[11] A. Taflove, S.C. Hagness, Computational Electrodynamics: The Finite-Difference Time-Domain Method, McGraw-Hill Education, 2016.

[12] M. Kaltenbacher, Numerical Simulation of Mechatronic Sensors and Actuators, Springer, 2015.

[13] M. Seoane, P.D. Ledger, A.J. Gil, M. Mallett, An accurate and efficient three-dimensional high-order finite element methodology for the simulation of magneto-mechanical coupling in MRI scanners, Int. J. Numer. Methods Eng. 119 (12) (2019) 1185–1215. https://doi.org/10.1002/nme.6088

[14] G. Barroso, M. Seoane, A.J. Gil, P.D. Ledger, M. Mallet, A. Huerta, A staggered high-dimensional proper generalised decomposition for coupled magneto-mechanical problems with application to MRI scanners, Comput. Methods Appl. Mech. Eng. 370 (2020) 113271. https://doi.org/10.1016/j.cma.2020.113271

[15] P.D. Ledger, A.J. Gil, R. Poya, M. Kruip, I. Wilkson, S. Bagwell, Solution of an industrially relevant coupled magneto-mechanical problem set on an axisymmetric domain, Appl. Math. Model. 40 (2016) 1959–1971. https://doi.org/10.1016/j.apm.2015.09.030

[16] S. Bagwell, P.D. Ledger, A.J. Gil, M. Mallett, M. Kruip, A linearised *hp*-finite element framework for acousto-magneto-mechanical coupling in axisymmetric MRI scanners, Int. J. Numer Methods Eng. 112 (2017). https://doi.org/10.1002/nme.5559

[17] S. Bagwell, P.D. Ledger, A.J. Gil, M. Mallett, Transient solutions to non-linear acousto-magneto-mechanical coupling for axisymmetric MRI scanner design: transient non-linear acousto-magneto-mechanical coupling in MRI, Int. J. Numer. Methods Eng. 115 (2018). https://doi.org/10.1002/nme.5802

[18] M. Seoane, P.D. Ledger, A.J. Gil, S. Zlotnik, M. Mallett, A combined reduced order-full order methodology for the solution of 3D magneto-Mechanical problems with application to MRI scanners, Int. J. Numer. Methods Eng. 121 (2020) 3529–3559. https://doi.org/10.1002/nme.6369

[19] G. Barroso, A.J. Gil, P.D. Ledger, M. Mallet, A. Huerta, A regularised-adaptive proper generalised decomposition implementation for coupled magneto-mechanical problems with application to MRI scanners, Comput. Methods Appl. Mech. Eng. 358 (2020) 112640. https://doi.org/10.1016/j.cma.2019.112640

[20] S. Miah, Y. Sooriyakanthan, P.D. Ledger, A.J. Gil, M. Mallett, Reduced order modelling using neural networks for predictive modelling of 3D-magneto-mechanical problems with application to magnetic resonance imaging scanners, Eng. Comput. 39 (6) (2023) 4103–4127. https://doi.org/10.1007/s00366-023-01870-3

[21] NGSolve Team. Define and mesh 2d geometries, 2021. https://docu.ngsolve.org/v6.2.2103/netgen_tutorials/define_2d_geometries.{html}.

[22] A.P.S. Kirkham, M. Emberton, C. Allen, How good is MRI at detecting and characterising cancer within the prostate?, Eur. Urol. 50 (6) (2006) 1163–1175. https://doi.org/10.1016/j.eururo.2006.06.025

[23] R. Harris, G. Wesbey, Artefacts in magnetic resonance imaging, Magn. Reson. Annu. 80 (1988) 71–112.

[24] I. Harvsteen, A. Ohlhues, K.H. Madsen, J.D. Nybing, H. Christensen, A. Christensen, Are movement artifacts in magnetic resonance imaging a real problem? a narrative review, Front Neurol. 8 (232) (2017). https://doi.org/10.3389/fneur.2017.00232

[25] D. Gallichan, J. Scholz, A. Bartsch, T.E. Behrens, M.D. Robson, K.L. Miller, Addressing a systematic vibration artefact in diffusion-weighted MRI, Hum Brain Mapp. 31 (2) (2010) 193–202. https://doi.org/10.1002/hbm.20856

[26] M.J. Graves, D.G. Mitchell, Body MRI artefacts in clinical practice: a physicist's and radiologist's perspective, J. Magn. Reson. Imaging. 38 (2) (2013) 269–287. https://doi.org/10.1002/jmri.24288

[27] A. Stadler, W. Schima, A. Ba-Ssalamah, J. Kettenbach, E. Eisenhuber, Artefacts in body MR imaging: their appearance and how to eliminate them, Eur. Radiol. 17 (5) (2007) 1242–1255. https://doi.org/10.1007/s00330-006-0470-4

[28] J. Schöberl, C++11 implementation of finite elements in NGSolve, ASC Report 30 (2014). https://ngsolve.org.

[29] I. Ramiére, T. Helfer, Iterative residual-based vector methods to accelerate fixed point iterations, Comput. Math. Appl. 70 (9) (2015) 2210–2226. https://doi.org/10.1016/j.camwa.2015.08.025

[30] A. Kovetz, Electromagnetic Theory, Oxford University Press, Oxford, UK, 2000.

[31] M. Ainsworth, J.T. Oden, A posteriori error estimation in finite element analysis, Pure and Applied Mathematics, Wiley-Interscience, New York, 2000.

[32] L. Demkowicz, Computing with hp-Adaptive Finite Elements: Volume 1: One and Two Dimensional Elliptic and Maxwell Problems, Chapman & Hall/CRC, 1st edition, 2006.

[33] L. Demkowicz, J. Kurtz, D. Pardo, M. Paszynski, W. Rachowicz, A. Zdunek, Computing with hp-Adaptive Finite Elements: Volume II Frontiers: Three Dimensional Elliptic and Maxwell Problems with Applications, Chapman and Hall/CRC, New York, 2007.

[34] J.M. Jin, Electromagnetics in magnetic resonance imaging, IEEE Antennas Propag. Mag. 40 (6) (1998) 7–22. https://doi.org/10.1109/74.739187

[35] E. Pardo, F. Grilli, Numerical Modeling of Superconducting Applications, World Scientific Publishing, 2023. https://doi.org/10.1142/9789811271441_0001

[36] J. Bonet, A.J. Gil, R.D. Wood, Nonlinear Solid Mechanics for Finite Element Analysis: Statics, Cambridge University Press, 2016.

[37] A.C. Eringen, G.A. Maugin, Electrodynamics of Continua I, Springer-Verlag, New York, 1990.

[38] C. Trimarco, On the dynamics of electromagnetic bodies, Int. J. Adv. Eng. Sci. Appl. Math. 1 (2009) 157–162. https://doi.org/10.1007/s12572-009-0007-6

[39] J. Bonet, A.J. Gil, R.D. Wood, Nonlinear Solid Mechanics for Finite Element Analysis: Dynamics, Cambridge University Press, 2021.

[40] J. Bonet, A.J. Gil, R. Ortigosa, On a tensor cross product based formulation of large strain solid mechanics, Int. J. Solids Struct. 84 (2016) 49–63. https://doi.org/10.1016/j.ijsolstr.2015.12.030

[41] S. Bagwell, A High Order Finite Element Coupled Multi-Physics Approach To MRI Scanner Design, Ph.D. thesis, Swansea University, UK, 2018.

[42] R.W. Brown, Y.N. Cheng, Magnetic Resonance Imaging:Physical Principles and Sequence Design, John Wiley & Sons, Ltd, 2014.

[43] A.J. MacLeod, Acceleration of vector sequences by multi-dimensional Δ2 methods, Commun. Appl. Numer. Methods 2 (1986) 385–392. https://doi.org/10.1002/cnm.1630020409

[44] B.M. Irons, R.C. Tuck, A version of the Aitken accelerator for computer iteration, Int. J. Numer. Methods Eng. 1 (3) (1969) 275–277. https://doi.org/10.1002/nme.1620010306

[45] C. Lemaréchal, An algorithm for solving a class of nonlinear programming problems, Math. Program. 3 (1) (1973) 77–97. https://doi.org/10.1007/BF01584097

[46] P. Wynn, On a device for computing the $e_m(S_n)$ transformation, Math. Tables Other Aids Computation 10 (54) (1956) 91–96. https://doi.org/10.2307/2002089

[47] B. Szabó, I. Babuška, Introduction to Finite Element Analysis: Formulation, Verification and Validation, John Wiley & Sons, Ltd, New Jersey, USA, 2011.

[48] W.R. Smythe, Static and Dynamic Electricity, McGraw-Hill, New York, USA, 1968.

[49] P.J. Roache, Code verification by the method of manufactured solutions, ASME. J. Fluids Eng. 124 (1) (2002) 4–10. https://doi.org/10.1115/1.1436090

[50] E. Süli, D.F. Mayers, An Introduction to Numerical Analysis, Cambridge University Press, Cambridge, UK, 2003.

[51] J. Elgy, P.D. Ledger, Efficient computation of magnetic polarizability tensor spectral signatures for object characterisation in metal detection, Eng. Comput. 41 (10) (2024) 2472–2503. https://doi.org/10.1108/EC-04-2024-0343

[52] R.L. Burden, J.D. Faires, Numerical analysis, Brooks/Cole, Cengage Learning, California, USA, 2010.

[53] F. Hennel, F. Girard, T. Loenneker, “Silent” MRI with soft gradient pulses, Magn. Reson. Med. 42 (1) (1999) 6–10.

[54] M.S. Miah, P.D. Ledger, A.J. Gil, M. Mallett, T.Q. Ye, An application of hp-version finite element methods to quench simulation in axisymmetric MRI magnets, Eng. Comput. (2025). https://doi.org/10.1007/s00366-025-02126-y

[55] I. Niyonzima, Y. Jiao, J. Fish, Modeling and simulation of nonlinear electro-thermo-mechanical continua with application to shape memory polymeric medical devices, Comput. Methods Appl. Mech. Eng. 350 (2019) 511–534. https://doi.org/10.1016/j.cma.2019.03.003